The Dissertation Committee for Chenglin Wu Certifies that this is the approved version of the following dissertation:

USING FAR-FIELD MEASUREMENTS FOR DETERMINING MIXED-MODE INTERACTIONS AT INTERFACES

Committee:

Kenneth M. Liechti, Supervisor

Rui Huang, Co-Supervisor

K. Ravi-Chandar

Nanshu Lu

John Foster

USING FAR-FIELD MEASUREMENTS FOR DETERMINING MIXED-MODE INTERACTIONS AT INTERFACES

by

Chenglin Wu, B.E.; M.S.; Ph.D.

Dissertation

Presented to the Faculty of the Graduate School of

The University of Texas at Austin

in Partial Fulfillment

of the Requirements

for the Degree of

Doctor of Philosophy

The University of Texas at Austin

May 2017

Dedication

To my family, for their love and sacrifices

Acknowledgements

I would like to express my most sincere gratitude and appreciation to my supervisor, Dr. Kenneth Liechti, without whose support and guidance this work would not have been possible. His insightful suggestions and great encouragement have been critical during the difficult times in my research and personal life. I am truly grateful for the experience gained during my time in his interface research group.

I would also like to give special thanks to Dr. Rui Huang who served as my co-supervisor. His incisive ideas in analysis and modeling have given me another perspective of my research.

I am grateful to Dr. K. Ravi-Chandar, Dr. Nanshu Lu, and Dr. John Foster for serving on my dissertation committee. I would like to thank them for their valuable time, advice, and effort in reviewing my dissertation.

Appreciation is also extended to Dr. Paul S. Ho, who provided part of the financial support during my first two years in the program. I am grateful for the experience working with him. I would further like to thank Dr. Stelios Kyriakides for introducing me to this program during my first visit. It was through his help I could begin my research journey in mechanics.

I would like to thank all the faculty whose course I have taken over my time at the University of Texas at Austin. They have been inspiring and helpful to broaden my knowledge in both Material Science and Engineering Mechanics. These course will serve as the corner stone of my future researches.

My sincere gratitude goes to our technical staff: Joe Poluda, Stephen Sanders, and Pablo Cortez, who helped me fabricate the parts for the specimens and experiments. I would like to thank Joe Poluda especially for his effort in preparing the substrates for the

specimens. Without his help, the experimental program could not have been accomplished in a timely manner. I would also like to thank Côme Pelée de Saint Maurice from Ecole Polytechnique, Paris, France for his great assistance in the experimental program during his summer internship in the interface research group. It was his help that made the system integration effortless in the experiment. I feel fortunate to have such great research group members for their constant interest and helpful discussions.

I am grateful to Semiconductor Research Corporation (SRC) for funding part of my research. I would also like to thank the Department of Aerospace Engineering and Engineering Mechanics for providing me teaching assistantships during my time here.

Using Far-field Measurements for Determining Mixed-Mode Interactions at Interfaces

Chenglin Wu, Ph.D

The University of Texas at Austin, 2017

Supervisor: Kenneth Liechti

Co-Supervisor: Rui Huang

Traction–separation relations (TSR) can be used to represent the interactions at a bimaterial interface during fracture and adhesion. The goal of this work is to develop a direct method to extract mixed-mode TSRs using only the far-field measurements.

The first topic of the dissertation deals with extracting mixed-mode TSRs based on a combination of global and local measurements including load-displacement, crack extension, crack tip opening displacement, and fracture resistance curves. Mixed-mode interfacial fracture experiments were conducted using the end loaded split (ELS) configuration for a silicon-epoxy interface, where the epoxy thickness was used to control the phase angle of the fracture mode-mix. Infra-red crack opening interferometry (IR-COI) was used to measure the normal crack opening displacements. For the resistance curves, an approximate value of the J-integral was calculated based on a beam-on-elastic-foundation model that referenced the measured load-displacement data. A damage-based cohesive zone model with mixed-mode TSRs was then adopted in finite element analyses, with the interfacial properties determined directly from the experiments. With the mode-I fracture toughness from a previous study, the model was used to predict mixed-mode

fracture of a silicon/epoxy interface for phase angles ranging from -42˚ to 0˚. Additional measurements would be necessary to further extend the reach of the model to mode-II dominant conditions.

The second topic of the dissertation addresses characterization of interfacial interactions between copper through-silicon vias (TSV) and silicon substrates. A suitable choice of via length allowed a direct method to be implemented for determining the mode-II traction-separation relation between silicon and copper TSVs. This interface was loaded in a nano-indentation experiment on specimens with pre cracks that were fabricated using focused-ion-beam (FIB) milling. The elastic and plastic properties of the copper vias were characterized from micro-pillar compression experiments and associated finite element analyses. Analytical and numerical models were developed for extracting the parameters of traction-separation relation.

The third topic of the dissertation explores a more general approach to directly extract the mixed-mode traction-separation relations using only far-field measurements from laminated beam specimens. Balanced laminated beam configurations were used to conduct the mixed-mode fracture experiment on a silicon-epoxy interface. The far-field measurements included the displacement at the middle of the bottom adherend at a point behind of the crack front, the force-displacement response, and the angle of rotation at the end of the top adherend. With these far-field measurements, the J integrals in mode-I and mode-II could be calculated separately when the ratio between the thickness and the bending stiffness is the same for both the top and bottom adherends. The local separations at the crack tip are also calculated using these far-field measurements. The traction-separation relations are then obtained directly through numerical differentiation of the obtained J integral with respect to the local separations. This method was validated by comparing to the local measurements of normal separation using IR-COI technique. The

extracted normal and shear TSR showed decoupled behavior in damage initiation and evolution which indicate that it is impossible to model using potential-based TSRs. A promising attempt was made to subtract out the elastic deformations of the epoxy that was used in this work. This was achieved by conducting a cohesive zone analysis using an extracted pair of normal and shear traction-separation relations for a particular mode-mix without the epoxy between the adherends.

Table of Contents

List of Tables

List of Figures

CHAPTER 1: INTRODUCTION

1.1 INTERFACIAL FRACTURE MECHANICS

Interfacial fracture in multi-layer structures has been a critical issue for thin film/substrate systems in electronic packages (Ho et al. 2004; Liu et al. 2007). Especially in chip-package systems, interfacial fractures along die and die-attach, die and epoxy molding compound interfaces are commonly observed after thermal processing (Zhang et al. 2008). These interfacial fractures normally propagate under mixed-mode conditions due to differences in layer thicknesses, materials, residual stresses as well as the globally applied loading. From a mechanics perspective, these problems have led to a wide range of fundamental and applied research.

The linearly elastic fracture mechanics (LEFM) and the cohesive zone modeling (CZM) approaches are commonly used for interfacial fracture problems. The former is often used in brittle fracture related problems where the fracture process zone is small and the materials are elastic. Williams (Williams 1959) conducted the pioneering work in the early development stages of the LEFM approach, in which he investigated the stresses ahead of crack between two dissimilar materials. This lead to extensive research seeking analytical solutions to interfacial fracture problems (Rice and Shih 1965, Rice 1968, Hutchinson et al. 1987, Rice 1988, Hutchinson and Suo 1992). In their solutions, the extent of material dissimilarity was found critical in determine the stress behavior ahead of interfacial crack tip (Dundurs 1969). This dissimilarity leads to the oscillatory singularity in the solutions which indicates the possible interpenetration of crack surfaces near the crack tip. This effect was found to be more significant when shear loading is involved. To quantify the shear component, the concept of phase angle (ψ) was introduced (Rice 1988, Hutchinson and Suo 1992) and referred to as the mode-mix, whose tangent is defined as

the proportion of the shear stress in comparison to the normal component. Due to the presence of oscillatory singularity, the evaluation of phase angle involves an arbitrary length scale which is related to the distance between the location where the mode-mix is obtained and the crack tip. In multi-layer structures, this length scale is usually taken as the thickness of the thinnest layer (Hutchison and Suo 1992). Interfacial toughness is then obtained as a function of the mode-mix (Cao and Evans 1989; Chai and Liechti 1992; Wang and Suo 1990). Determination of this function is paramount as it not only can predict interfacial toughness at different mode-mix values but also determines when interfacial cracks propagate under mixed-mode loading conditions. The LEFM approach has gained tremendous popularity due to the availability of abundant solutions. However, limitations arise when analyzing interfacial cracks between purely elastic media without accounting for any interactions between the crack surfaces.

The CZM approach, which does account for such interactions, was first proposed by Dugdale and Barrenblatt (Dugdale 1960, Barenblatt 1962) to describe the near crack tip behavior by accounting for the fracture process zone. By introducing the traction-separation relations (TSRs) of the interfaces, this approach offered a way to model fracture nucleation and propagation which was lacking in LEFM. Needleman (1987), Ungasuwarungsri, and Knauss (1987) first applied this approach in modeling interfacial fracture propagation. CZM soon became popular not only for modeling interfacial delamination (Feraren and Jensen 2004; Li et al. 2005; Parmigiani and Thouless 2007; Valoroso and Champaney 2006), but also for other interface problems such as crack nucleation at bi-material corners (Mohammed and Liechti 2000), plastic dissipation in thin films (Shirani and Liechti 1998), and delamination of composites (Li and Thouless 2006; Moroni and Pirondi 2011; Sørensen and Jacobsen 2003). However, specific interfacial traction-separation relations are required to properly describe the fracture propagation

process and make meaningful predictions. In addition, the mixed-mode nature of TSRs for interfaces has to be accounted for in order to model interfacial fracture growth process (Li et al. 2006, Högberg et al. 2007, Parmigiani and Thouless 2007, Zhu et al. 2009).

The form of TSRs was often assumed in the early development of CZM approach. In the Dugdale model (Dugdale 1960), an idealized traction-separation relation was used which has a constant traction region before failure. The trapezoidal and the bilinear forms of TSRs were later assumed in a more realistic description of interfacial fracture growth (Tvergaard and Hutchison 1996). Other forms of TSRs have been assumed, representing different fracture growth mechanisms. However the following characteristics are generally followed in these assumptions (Park and Paulino 2013): (1) the TSR is independent of superimposed rigid body motion; (2) the fracture energy defined as the area under the TSR curve is finite; (3) the mode-I toughness is usually different from the mode-II toughness; (4) critical separations exist which lead to zero tractions; (5) softening stages exist; (6) a potential for the TSRs may exist or not.

Based on assumption (6), the TSRs can be categorized as potential-based or damage-based. The most commonly implemented potential based TSRs are that developed by Xu and Needleman (1993) in which traction-separation relationships are obtained from the first derivatives of an interface potential function. In this model, normal and tangential behavior is coupled via exponentially decaying functions of normal and tangential separation (McGarry et al. 2013). The ratio of work of tangential separation to the work of normal separation was defined to determine the strength of interface under mode I and mode II separation. Although this ratio was found to be varying in experiments (Dollhofer et al. 2000, Warrior et al. 2003, Yang et al. 2001), it was often assumed to be constant in many implementations (Rahulkumar et al. 2000, Yuan and Chen 2003, Zavattieri et al. 2008). In the potential-based model, the absence of damage means that there will yield zero

dissipation in the case of closed deformation loop. This path independence nature causes troubles when modeling unloading process for interfacial fracture problems where the loading protocol is not monotonic. In the damage-based TSRs, the decaying function of traction is often determined by the damage factor which is a function of the vectorial separation (Ungsuwarungsru and Knauss 1987, Alfano and Crisfield 2001). The damage fact penalized the stiffness to simulate the decaying behavior in tractions. The coupling of the normal and shear behavior was determined by sharing the same damaging factor. In the damage-based model, elastic unloading is expected. The energy dissipation exists based on loading history.

1.2 Interfacial Fracture Experimental Methods

Numerous fracture specimens and loading configurations have been developed (Suo and Hutchinson 1988, Reeder and Crews Jr. 1990, Chai and Liechti 1992, Davidson and Sundararaman 1996, Birringer et al. 2011) to characterize interfaces covering wide ranges of mode-mix. Laminated structures with beam type geometries have been commonly used for their simplicity and conveniences for measurements. The double cantilever beam (DCB), the end notched flexure (ENF) test (Barrett and Foschi 1977, Chai and Mall 1988), the end-loaded split (ELS) test (Wang and Vukanh 1996) and the mixed-mode bending (MMB) (Charalambides et al. 1989, Charalambides 1990) are some of the commonly used configurations in interfacial fracture experiments. The sandwich structures (Suo and Hutchinson 1988, Liechti and Freda 1989, Liechti and Marton 2002, Bing and Davidson 2010) are especially favored as they provide various loading configuration options and relative easy in sample preparation. Most of the above mentioned work focus on characterization of fracture toughness.

For characterizing TSRs of the interface, the double cantilever beam (DCB) specimen (Kanninen 1973, Chow et al. 1979, Williams 1989, Zhu et al. 2009) was mainly used for mode-I interfacial fracture. Its main advantage is providing a nominally mode-I loading condition. However, the DCB specimen can also be used to extract mixed-mode TSRs when loaded asymmetricaly (Sørensen and Kirkegaard 2006, Mangalgiri et al. 1986, Sundararaman and Davidson 1997). Other commonly used mixed-mode specimens include the four point bend test (Charalambides et al. 1989, Charalambides 1990) and the end loaded split (Hutchinson and Suo 1992, Wang and Vukanh 1996). The nature of mixed-mode experiments has always required the need for innovation which has brought about a lot of modifications to previously existing mixed-mode test specimens (Reeder and Crews Jr. 1990, Fernlund and Spelt 1994, Davidson and Sundararaman 1996, Bing and Davidson 2010). Each specimen however, has its own advantages and limitations with respect to the mode-mix range provided, the material system dependence and the ease of implementation.

As mentioned in the earlier section, local crack tip measurements such as crack front location and opening are often required for extraction of TSRs. Crack opening interferometry (COI) (Liechti 1993), digital image correlation (DIC) (Pan et al. 2009) and laser generated stress pulses (Pronin and Gupta 1998) have been developed in the past decade to provide such measurements. Crack opening interferometry has been used to characterize crack tip behavior in glass/adhesive systems (Chai and Liechti 1992, Liechti 1993, Swadener et al. 1999, Mello 2003), copper/sapphire bi-crystals (Kysar 2001), functionalized silicon surfaces (Na et al. 2011, Na et al. 2016) and silicon/epoxy interface (Gowrishankar et al. 2012). In the latter three reports, the silicon/epoxy interface was characterized using this technique with infrared (IR) light sources as silicon is transparent to IR radiation. The main advantage of this technique is that it provides high resolution depending on the wavelength of the light source. Its major limitation lies in the extent of

transparency of the materials to the IR light. In addition, this technique only provides normal crack opening displacements (NCODs) hence could not be used to measure the crack tip behavior in the tangential direction.

1.3 DETERMINING MIXED-MODE TSRS

The determination of TSRs are generally approached either directly or iteratively. In the direct approach, the specific mode-mix is identified using an LEFM analysis prior to the extraction of TSRs. The energy release rate is then calculated approximately using analytical solutions. The local crack tip deformations is then measured experimentally. The TSRs can then be directly evaluated by taking of the derivative of the energy release rate with respect to the measured crack tip displacement. This method was demonstrated by many groups (Stigh and Andersson 2000, Sørensen and Jacobsen 2003, Andersson and Stigh 2004, Sorensen et al. 2008, Zhu et al. 2009, Li et al. 2011, Li et al. 2013, Gowrishankar et al. 2012). However this extraction approach can be constrained by resolution issues in locating the crack front and measuring the crack tip opening displacements (CTODs). The iterative approach, however, determines the parameters of TSR with assumed forms by comparing numerical solutions of variables such as load, crack extension (resistance curves), crack opening displacements to measurements. By matching the local measurements to CZM results (Cox and Marshall 1991, Swadener and Liechti 1998, Mohammed and Liechti 2000, Li et al. 2005, Mello and Liechti 2006, Sørensen et al. 2008, Gain et al. 2011, Shen and Paulino 2011, Na et al. 2011) or by comparing far-field measurements such as load-displacement response, specific TSRs are extracted corresponding to mode-mix.

The extraction of TSRs relying on only far-field measurements is essentially an inverse problem, which can be categorized into two types. In the first type, the extraction

uses whole-field deformation measurements such as moiré interferometry (Guo et al. 1999, Mohammed and Liechti 2000). The second type uses experimentally measured load-displacement or resistance curve data to find the optimal parameters for the cohesive-zone laws as mentioned earlier.

The first approach is based on the Almansi theorem of elasticity (Sokolnikoff 1946), which states that if the displacements and tractions are simultaneously prescribed over a finite region of the boundary of an elastic body, the whole elastic field is then uniquely determined. As an example of this approach, Hong and Kim (2003) developed the field projection method to extract the cohesive-zone laws from far-field measurements. In this full inversion analysis, a solution method was developed that utilizes the path-independent interaction J-integral applied to an eigenfunction expansion of the cohesive crack-tip field. First, a fundamental elastic-field solution to a semi-infinite crack with a cohesive zone is developed, which was used as an auxiliary probe field. By applying interaction J-integrals between the auxiliary field and the measured displacement data , the coefficients of the eigenfunction expansion are then determined. This method ensured the uniqueness of the TSRs in the cohesive zone and provided an powerful tool to extract TSRs under mixed-mode conditions.

The second approach is commonly applied to laminated beam type specimens, where the path-independent J-integral can be estimated through beam theories or finite element analysis. A functional form of the TSRs is usually assumed depending on the material systems and the corresponding fracture processes. Then the characteristic parameters of the assumed functional form are found iteratively by optimizing the parameters to match the numerical results obtained using finite element analysis to measured data. This approach is also defined as the iterative approach mentioned in Section 1.1. In the cases when the CTODs can be directly measured, the assumption of the

functional form of TSRs can be relaxed. This approach becomes the direct method mentioned in Section 1.1. This type of approach has significant draw backs in the following areas: (1) the J-integral is approximated based on beam theory without fully considering the interactions along the interfaces; (2) this approach is very sensitive to the resolution of the CTOD measurements, which is hard to control in small-scale experiment; (3) this approach cannot generally be applied in mixed-mode conditions due to the coupling of the normal and shear tractions along the interface. Among these drawbacks, the third one is the most difficult to overcome since due to the universality of mixed-mode fracture at interfaces.

To overcome this drawback, extensive efforts have been made to partition the energy release rate (ERR) into mode-I (opening mode) and mode-II (sliding mode). Williams (1998) conducted the pioneering work in mode-partition using beam theory on DCBs made of isotropic materials. Both pure mode I and II conditions were obtained in the absence of axial loads. However, the mixed-mode partition was limited to symmetric DCBs. Schapery and Davidson (1990) combined numerical and analytical methods to predict the ERR under the mixed-mode conditions provided by asymmetric DCB specimens. Hutchinson and Suo (1990) reported on the partition of ERR using a combined approach with Euler beam theory and 2D elasticity, with stress intensity factors.. They also made comments on what were seen as conceptual errors in William's work. However, later experimental work by Charalambides et al. (1992) pointed out that the partition theory developed by Williams work agreed was in better agreement with the experiments. This is due to the fact that large bridging might have occurred in Charalambides' experiments. However, most of the analysis were focused on perfectly bonded interfaces. Nguyen and Levey (2009) presented an exact theory of interfacial debonding in layered elastic composites using Fourier series. In their work, non-linear springs were assumed along the

interface. Wang et al. (2013) developed expressions for EER in layered isotropic double cantilever beams with non-rigid cohesive interfaces. Conroy et al. (2015) conducted mixed-mode experiments and pointed out that partition is involved in general. This is due to the fact that the traction distribution in the cohesive zone is dependent on the coupling of the governing equations for separation distributions. Ouyang and Li (2009) reported on the decoupling of tension and shear interactions in the governing equation for the shear traction distribution in the end-notched flexure experiment and conducted experiments extracting interfacial properties in pure Mode-I (Ouyang et al. 2011) and moderate mix-modes by varying the thickness of the adhesive (Ji et al. 2012). In their work, the single leg bending (SLB) configuration was used. The range of mode-mix was limited because both adherends were made of the same material and had the same thickness. The relationship between the local crack tip displacements and measurements of global parameters such as load and load-line displacement and rotation was not revealed. As a result, the local CTOD displacements were measured from images captured near the crack tip using a CCD camera. The resolution of the local CTOD measurements was about 3.7 μm/pixel, which cause challenges for silicon/epoxy interfaces where critical separations are normally on the order of several μm (Gowrishankar et al. 2014, Wu et al. 2016).

1.4 OBJECTIVES

The main objective of this dissertation is to develop methods to extract mixed-mode traction-separation relations for interfaces using far-field measurements with little or no local measurements. Specifically, in the next three chapters, the objectives are:

1. Exploring the determination of the mixed-mode TSRs of the silicon/epoxy interface using both global variables and local crack tip measurements.

2. Developing a method to characterize the TSV/Si interface using the load-displacement response from nano-indentation.
3. Developing a direct method to extract mixed-mode TSRs using only measurements at the loading points of laminated beam specimens.

CHAPTER 2: DETERMINING MIXED-MODE TSRS USING LOCAL AND FAR-FIELD MEASUREMENTS

In this chapter, a direct method is proposed to extract mixed-mode traction-separation relations based on measurements of fracture resistance curves and crack tip opening displacements. Mixed-mode interfacial fracture experiments were conducted using the end loaded split configuration for a silicon-epoxy interface, where the mode mix was varied with the epoxy thickness. An infra-red crack opening interferometry (IR-COI) was used to measure the normal crack opening displacements, while both normal and shear components of the crack-tip opening displacements were obtained by digital image correlation (DIC). A damage-based cohesive zone model with mixed-mode traction-separation relations was adopted in finite element analyses, with the interfacial properties determined from the experiments. The mixed-mode cohesive zone model can then be used to predict mixed-mode fracture of the same interface for a range of mode-mix within the limits of the experiments.

2.1 EXPERIMENTS

In this section, we describe the specimen preparation, loading devices, and measurement techniques (IR-COI and DIC) that were used in the experiments.

2.1.1 Specimen preparation

A schematic of the specimen geometry and apparatus is shown in Fig. 1. The specimen consists of two silicon strips joined by a layer of epoxy. The n-type Si (111) wafers supplied by WRS Materials were polished on both sides to facilitate the use of IR-COI. The wafers were 50 mm in diameter and nominally 590 μm in thickness. An automatic dicer (Disco, model DAD 321) was used for cutting wafers into 50 by 5 mm (for top adherends) and 40 by 15 mm (for bottom adherends) strips, which were then cleaned

individually by ultra-sonication in de-ionized water to remove any accumulated debris. The top adherend was coated with an Au/Pd thin film from one end of the strip to a length of about 25 mm. The relatively low adhesion energy between the Au/Pd coating and the epoxy (~ 0.07 J/m^2) allowed an initial crack to form with minimal damage to the silicon/epoxy interface.

The epoxy in the experiments was prepared by mixing the resin (modified bishpenol-A epoxy, Araldit® GY502) and hardener (polyamidoamine, Aradur®955) in a ratio of 100:45 by weight. The epoxy mixture was then de-gassed in a vacuum chamber. To prepare the specimen, a silicon strip was placed on Teflon® tape with shims of different thickness to control the height of the epoxy layer. A bead of the degassed epoxy was dropped on the silicon surface and spread out with a spatula. Then the silicon strip coated with the Au/Pd thin film was pressed on the bead with a weight to spread the epoxy into a layer between the two silicon strips. The specimen was cured at 65 ˚C for 3 hours and then allowed to cool to room temperature. For the DIC measurements (Fig. 1b), the lower adherend was diced to the same width as the top adherend so that the side faces of the specimen could be polished to have the required texture. Upon cooling of the specimen, a random pattern was generated in the region of interest by polishing of the side of the silicon strip with a high grit (>600) sand paper, which allowed correlation software to match subsets of the images (Gowrishankar 2014).

A total of 6 groups of specimens were prepared for both the IR-COI and DIC measurements. The epoxy thickness for these specimens were 5, 8, 9.3, 12, 23.3, and 50 μm, measured by caliper.

2.1.2 Load-displacement measurements

Once the specimen was prepared, it was mounted onto the loading device as shown in Figure 1. The loading device consists of a linear actuator coupled with a load cell connected to a loading head. The displacement controlled loading protocol was prescribed at the end of the top silicon strip. The loading rate was controlled to be at 0.1 μm/s. Both the displacement and load measurements were taken simultaneously.

A typical load-displacement response is shown in Figure 2 with a loading-unloading cycle. The loading response started with a slightly nonlinear segment due to contacts and formation of an initial crack by debonding of the Au/Pd coated part of the interface. The response then became linear elastic until crack growth started along the silicon/epoxy interface. The crack growth led to the non-linear response as the slope decreased gradually with increasing crack length. The unloading response was largely linear elastic, but with a smaller stiffness than the loading response as expected for a longer crack. As a global measurement, the load-displacement responses were used to determine the global J-integral for the fracture-resistance curves as discussed in the later sections.

2.1.3 IR-COI measurements

The transparency of silicon to infra-red enabled the measurement of crack length and normal crack opening displacement (NCOD) by classical crack opening interferometry (Liechti, 1993). This infrared crack opening interferometry (IR-COI) technique essentially uses the interference between the two rays reflected from the crack surfaces to determine the distance between them. The experiments were performed using an infrared microscope (Olympus BH2-UMA) that was fitted with an internal beam splitter and an IR filter (1,040 ± 15 nm) to provide the normal incident beam. A digital camera (Lumenera Corpporation, Infinity 3) with a resolution of 1,392 × 1,040 pixels captured the images. The images were then processed to determine the location of the crack front and the NCOD (Gowrishankar

et al. 2012). Figure 3a shows a fringe pattern obtained by IR-COI and the variation of crack length with applied displacement. The procedure for measuring the crack length has been described in detail elsewhere (Gowrishankar et al. 2012). The crack front remained stationary until the applied displacement reached about 0.25 mm, after which the crack growth was observable by IR-COI. The corresponding NCOD profiles near the crack front at different applied displacements are shown in Fig. 3b. The location $x = 0$ was set at the location of the initial crack front as established by the initial intesntiy pattern. The resolution of the IR-COI technique implemented in this work was approximately 330 nm for the crack length and 20 nm for measurements of crack length and NCOD, respectively.

2.1.4 DIC measurements

DIC was implemented by analyzing images of areas of interest as time elapsed during experiment using the ARAMIS® correlation software. The images were taken with the help of a 45° prism mirror fixed to a groove parallel to the specimen (Fig. 1b). This allowed a surface of the specimen that was intersected by the crack front to be viewed during the experiment, thereby allowing both the normal and tangential displacements near the crack front to be obtained. The DIC technique essentially provides a full field measurement of the in-plane deformation, but two reference points were identified on the silicon strips at the same horizontal location as the crack front (Fig. 4a). The relative displacement between these two points, including both normal and tangential components with respect to the interface, were determined as the components of the crack tip opening displacements (CTOD) and recorded as a function of the applied displacement as shown in Fig. 4b. The resolution in the CTOD measurement was about 80 nm.

2.2 MODELING AND ANALYSIS

To interpret the experimental data and then to predict mixed-mode interfacial fracture, a simple beam on elastic foundation (BEF) model was adopted first, followed by a mixed-mode cohesive zone model and finite element simulations using the cohesive surface approach in ABAQUS®.

2.2.1 Beam on Elastic Foundation

Based on the loading condition, then end-loaded split (ELS) specimen can be considered as a cantilever beam on an elastic foundation, with which the energy release rate (J-integral) can be calculated based on the global measurements of the load and displacement. A model based on beam-on-elastic-foundation was presented in a previous study (Gowrishankar et al. 2012), which yielded the force-displacement response at the loading point as

$$P = \frac{3E_{si}I_{si}\Delta}{a^3}\left(1+\frac{3}{\lambda a}+\frac{3}{(\lambda a)^2}+\frac{3}{2(\lambda a)^3}\right)^{-1}, \tag{2.1}$$

where P is the applied force, Δ is the displacement at the loading point, a is the crack length (measured from the loading point to the crack tip), $\lambda = \left(\frac{6K_e}{E_{si}h_{si}^3}\right)^{\frac{1}{4}}$, $I_{Si} = \frac{1}{12}b_{Si}h^3{}_{Si}$, b_{Si} is the width of the silicon strip, h_{Si} is the thickness of the silicon strip, and E_{si} is Young's modulus of silicon. The parameter K_e represents the stiffness of the elastic foundation, which may be approximated for the ELS specimen as $K_e = E_e / h_e$ with E_e as Young's modulus of epoxy and h_e as its thickness. The predicted load-displacement response by Eq. (2.1) compared well with the measurement (Fig. 2). The crack length can then be determined from the measurements of P and Δ as

$$a_{eff} = \frac{1}{\lambda}\left[\left(3E_{si}I_{si}\left(\frac{\Delta}{P}\right)\lambda^3-\frac{1}{2}\right)^{\frac{1}{3}}-1\right]. \tag{2.2}$$

The crack lengths thus obtained are shown in Figure 3a, in excellent agreement with the crack lengths measured by IR-COI. In these calculations, E_{si} and E_e are taken as 165.5 GPa and 2.03 GPa, respectively. The in-plane tensile modulus of the Si(111) strips was measured in three-point bending (Gowrishankar 2014). The beam thickness h_{Si} was 0.59 mm, and its width b_{Si} was 5 mm, while the epoxy thickness h_e was 8 μm.

The corresponding energy release rate or J-integral for the crack growth by the BEF model is (Gowrishankar et al. 2012)

$$J\left(P,a\right)=\frac{6\left(Pa\right)^2}{E_{si}b_{si}^2h_{si}^3}\left(1+\frac{1}{\lambda a}\right)^2. \tag{2.3}$$

With the effective crack length in Eq. (2.2), the global J-integral can be directly obtained using the force and displacement data as

$$J(P,\Delta)=\frac{6P^2}{\lambda^2E_{si}b_{si}^2h_{si}^3}\left(\frac{E_{si}b_{si}h_{si}^3\lambda^3}{4}\left(\frac{\Delta}{P}\right)-\frac{1}{2}\right)^{\frac{2}{3}}. \tag{2.4}$$

2.2.2 Fracture resistance curves

Fracture resistance curves (Fig. 5) were critical to the extraction of the traction–separation relations. A resistance curve was generated for each epoxy thickness using the crack extension (Δa) obtained from the IR COI measurements and the J-integral calculated by means of Eq. 4 and the measured load-displacement response. For each ELS specimen, the initial crack did not grow appreciably (Δa <0.2 μm) until the J-integral reached a critical level (J_0). Subsequently, as the J-integral increased, the observable crack length increased. Eventually, the crack growth is expected to reach a steady state with a constant J-integral (J_{SS}) under the displacement-controlled loading condition. However, the experimental data did not always show clear evidence of the steady state, possibly due to the limitation placed by the field of view available to the IR-COI system. In such cases, the last data point on the resistance curve was taken as the closest approximation of the steady state. The amount

of observable crack growth to reach the steady state is labeled as Δa_{SS}, which corresponds to the steady-state damage zone size in the cohesive zone model as discussed later. Clearly, Figure 5 shows that the resistance to fracture increased with decreasing epoxy thickness. However, since decreasing the adhesive layer thickness is usually expected to decrease the resistance to fracture (Chai 1988, 1990), the effect of fracture mode-mix on toughness for this epoxy (Chai and Liechti 1992) is considered in the next section as a potential contributing factor. In addition, the three quantities defined for each resistance curve, J_0, J_{SS}, and Δa_{SS}, will be used to determine the key parameters of the traction–separation relations in the cohesive zone model.

2.2.3 Linearly elastic fracture analysis

Based on linear elastic fracture mechanics (LEFM) (Rice, 1988; Hutchinson and Suo 1992), the traction on the interface directly ahead of the crack tip for an interfacial crack can be written in a complex form as

$$\sigma + i\tau = (K_1 + iK_2)(2\pi r)^{-1/2} r^{i\varepsilon} \tag{2.5}$$

where σ and τ are the normal and shear tractions, $K = K_1 + iK_2$ is the complex stress intensity factor, r is the distance to the crack tip, and $\varepsilon = \frac{1}{2\pi} \ln\left(\frac{1-\beta}{1-\beta}\right)$ with Dundur's parameter $\beta = \frac{1}{2} \frac{\mu_1(1-2\nu_2) - \mu_2(1-2\nu_1)}{\mu_1(1-\nu_2) + \mu_2(1-\nu_1)}$. The ratio between the shear and normal stresses in Eq. (2.5) depends on r unless $\varepsilon = 0$. Therefore, an arbitrary length (l) has to be used to define the phase angle of mode-mix as,

$$\psi_K = \tan^{-1}\left(\frac{\mathrm{Re}\left(Kl^{i\varepsilon}\right)}{\mathrm{Im}\left(Kl^{i\varepsilon}\right)}\right), \tag{2.6}$$

Using different length scales leads to a shift in the phase angle. In the present study, we take $l = h_e$ for the ELS specimen and calculate the phase angle using a semi-analytical method and a plane strain finite element model of the ELS specimen.

The semi-analytical method recognizes that the ELS specimens in the present study are sandwich specimens where the complex stress intensity factor *K* of the interfacial crack depends on the elastic properties of the materials as well as the thickness of the sandwiched layer through (Suo and Hutchinson 1989)

$$K = h_e^{-i\varepsilon}\left(\frac{1+\alpha}{1-\beta^2}\right)^{1/2}\left(K_I + K_{II}\right)e^{i\omega}, \tag{2.7}$$

where K_I and K_{II} are the so-called global stress intensity factors associated with the reference homogeneous specimen (silicon strips joined without epoxy) but loaded in the same manner. The global stress intensity factors were obtained from tabulated values given in (Li et al. 2004) for a transversely loaded strip being separated from an infinitely thick substrate, which gives a global phase angle of the mode-mix, $\psi_K = \tan^{-1}(K_{II}/K_I) = -36°$. The angle ω depends on the elastic mismatch between silicon and epoxy, which is -8° by numerical calculations as tabulated in (Suo and Hutchinson 1989). Then, by Eq. 2.6 with $l = h_e$, the local phase angle of the mode-mix is -44° for the ELS specimen. Note that this result represents the limiting case for an epoxy layer that is very small compared to the thickness of the silicon strip and other in-plane length scales (e.g., the crack length).

In view of the assumptions in the semi-analytical method, a plane strain, linearly elastic finite element model (Fig. 6a) was also used to calculate the stress intensity factors and phase angles for the ELS specimens with a range of epoxy thicknesses. A stationary crack along the upper silicon/epoxy interface was assumed, and the interface ahead of the crack was perfectly bonded. A typical mesh near the crack tip, where the singular elements were used, is shown in Fig. 6b. The real and imaginary parts of the complex stress intensity factor at the crack tip were calculated and the corresponding phase angle of the mode-mix was obtained from Eq. 2.6. As shown later (Section 2.3.1), the phase angle depends on the epoxy thickness but approaches the asymptotic limit (-44°) as the epoxy thickness

decreases, thereby allowing the mode-mix in the experiments to be controlled by varying the epoxy thickness of the ELS specimens.

2.2.4 Mixed-mode cohesive zone analysis

To simulate interfacial crack growth in the ELS specimens, a finite element model was constructed using the commercial package ABAQUS®, where the silicon/epoxy interface was modeled by surface-based cohesive interactions with a mixed-mode traction-separation relation. At each point along the interface, the normal and shear tractions are related to the relative displacement across the interface through,

$$\begin{aligned} \sigma_n(\delta_n,\delta_t) &= (1-D)K_n\delta_n \\ \sigma_t(\delta_n,\delta_t) &= (1-D)K_t\delta_t \end{aligned} \tag{2.8}$$

where $D = f(\delta_n,\delta_t)$ is a local damage parameter, generally a function of the interfacial separations in both the normal and tangential directions (δ_n and δ_t). Prior to damage initiation (D = 0), the normal and shear traction-separation relations are un-coupled and linear elastic with respective stiffnesses, K_n and K_t. The quadratic nominal stress criterion (QUADS) was used as the criterion for damage initiation,

$$\left(\frac{\sigma_n}{\sigma_{n0}}\right)^2 + \left(\frac{\sigma_t}{\sigma_{t0}}\right)^2 = 1, \tag{2.9}$$

where σ_{n0} and σ_{t0} are the maximum possible stresses in normal and shear directions, respectively. For the ELS specimens in the present study, it was found that damage initiation was primarily controlled by the normal traction (Gowrishankar 2014). This was simulated by setting σ_{t0} to be much larger than σ_{n0} so that the second term on the left hand side of Eq. (2.9) was negligible. For this reason, σ_{t0} = 1 GPa was used in the cohesive zone model. As a result, the critical normal traction for damage initiation by Eq. (2.9) is nearly independent of the mode-mix ($\sigma_n \approx \sigma_{n0}$), while the corresponding shear traction and the vectorial traction ($\sigma = \sqrt{\sigma_n^2 + \sigma_t^2}$) do depend on the mode-mix.

The mode mix for the cohesive zone model can be defined locally based the ratio between the displacement components or the traction components. By using the same stiffness for the normal and shear components in Eq. (2.8), $K_n = K_t = K_0$, the two ratios become identical and hence the phase angle of mode mix for the cohesive zone mode is:

$$\psi = \tan^{-1}\left(\frac{\sigma_t}{\sigma_n}\right) = \tan^{-1}\left(\frac{\delta_t}{\delta_n}\right) \tag{2.10}$$

It is noted that the locally defined phase angle may not be a constant value within the cohesive zone. In this study, we take the phase angle at the initial crack tip as the mode mix of each specimen. As shown in Figure 8, the phase angles by the cohesive zone model are close to those based on the LEFM approach, but different from those based on the DIC measurements. This difference may be caused by the uncertainties in the selected locations as the reference points for the DIC measurements.

The mixed-mode traction-separation relation after damage initiation depends on the evolution of the damage parameter D in Eq. (2.8). Following the assumption that damage initiation is controlled by the normal traction, the critical displacements at the point of damage initiation are approximately, $\delta_{n0} = \sigma_{n0}/K_0$ and $\delta_{t0} = \delta_{n0}\tan\Psi$. The corresponding vectorial displacement is $\delta_0 = \sigma_0/K_0$ where $\sigma_0 = \sigma_{n0}/|\cos\Psi|$ is the vectorial traction. For a particular mode mix, when the vectorial displacement $\delta = \sqrt{\delta_n^2 + \delta_t^2} > \delta_0$, the damage parameter evolves from 0 to 1 as a function of δ. For this study, an exponential function was used for the damage evolution, which takes the form:

$$D(\delta_m) = 1 - \frac{\delta_0}{\delta_m}\left[1 - \frac{1 - \exp\left(-\alpha\dfrac{\delta_m - \delta_0}{\delta_f - \delta_0}\right)}{1 - \exp(-\alpha)}\right] \tag{2.11}$$

where δ_m is the maximum value of the vectorial displacement δ that has been reached at the point throughout the loading history, δ_f is the vectorial displacement when the interface is fully damaged (D = 1) at the point, and α is a shape parameter for the exponential softening. As a result, when δ decreases (unloading), δ_m does not change and D remains a constant so that the traction decreases linearly with a reduced stiffness by Eq. (2.8). In other words, the damage is unrecoverable.

The local J-integral with a contour enclosing the cohesive zone can be evaluated using the tractions and separations that acre active there, so that (Rice, 1988)

$$J(\delta_n^*, \delta_t^*) = \int_0^{\delta_n^*} \sigma_n d\delta_n + \int_0^{\delta_t^*} \sigma_t d\delta_t \tag{2.12}$$

where δ_n^* and δ_t^* are the normal and shear separations at the initial crack tip. The use of the same stiffness in the normal and tangential directions in Eq. (2.8) ensures that the vectorial traction ($\sigma = \sqrt{\sigma_n^2 + \sigma_t^2}$) is in the same direction as the vectorial displacement so that the local J-integral can be calculated by a single integral over the vectorial traction-separation relation $\sigma(\delta)$, namely

$$J(\delta^*) = \int_0^{\delta^*} \sigma \, d\delta \tag{2.12}$$

where δ^* is the vectorial separation at the initial crack tip (CTOD). With the damage evolution in Eq. (2.11), the mixed-mode fracture toughness can be obtained by the J-integral with $\delta^* = \delta_f$, i.e.,

$$\Gamma(\psi) = \int_0^{\delta_f} \sigma d\delta \tag{2.14}$$

As shown in Figure 7, the vectorial traction-separation relation consists of a linear elastic part ($0 < \delta < \delta_0$) and an exponential softening part ($\delta_0 < \delta < \delta_f$), which can be integrated separately to yield

$$\Gamma_1(\psi) = \int_0^{\delta_0} \sigma d\delta = \frac{1}{2}\sigma_0 \delta_0 \tag{2.15}$$

and

$$\Gamma_2(\psi) = \int_{\delta_0}^{\delta_f} \sigma d\delta = \sigma_0 \left(\delta_f - \delta_0\right)\left(\frac{1}{\alpha} - \frac{1}{e^{\alpha} - 1}\right) \tag{2.16}$$

As a result, $\Gamma(\psi) = \Gamma_1(\psi) + \Gamma_2(\psi)$. This decomposition of the fracture toughness turned out to be useful for determining the traction-separation relation.

In ABAQUS, the mixed-mode traction-separation relations can be specified in a tabulated form. First, a stiffness K_0 is specified for the linear part of the traction-separation relation in both the normal and tangential directions. Next, for damage initiation, σ_{n0} and σ_{t0} are specified in Eq. (2.9), which are independent of mode mix. In the present study, the values of K_0 and σ_{n0} were extracted from experiments as discussed in Section 2.6, whereas σ_{t0} was set to be 1 GPa as noted before. The exponential damage evolution in Eq. (2.11) requires input of two parameters for each mode mix, $\delta_f - \delta_0$ and α, which can be tabulated with the corresponding energy ratio (m_1) for each mode-mix. By definition, the energy ratio is related to the phase angle of mode mix as

$$m_1 = \frac{\int_0^{\delta_n} \sigma_n d\delta_n}{\int_0^{\delta} \sigma d\delta} = \left(\cos\psi\right)^2 \tag{2.17}$$

In the cohesive zone modeling (CZM) of the ELS specimen, the silicon/epoxy interface was modeled by surface-based cohesive interactions with the mixed-mode traction-separation relation just described. An example of the mesh with some opening at the initial crack tip and the tractions due to the interactions within the cohesive zone is shown in Fig. 6c. The surface-based approach in ABAQUS differs slightly from the cohesive element approach. The latter treats the interface as a solid layer with an artificial thickness and implements the traction-separation relation as its constitutive behavior. However, it was found that using the cohesive elements did not correctly return the input tangential traction-separation relation under mixed-mode conditions. The likely cause of

this issue is in the calculation of the shear strain for the cohesive element, which includes an additional term due to the gradient of normal separation, but is not part of the traction-separation relation. On the other hand, in the surface-based approach, the traction-separation relation is defined as a mechanical contact property between two surfaces and is implemented within the general contact pair framework in ABAQUS/Standard. This allows direct calculations of the interfacial separations as the relative displacements between the nodes on the slave surface and their corresponding projection points on the master surface in the normal and shear directions, without involving any strain or the thickness of the interface. It was found that the surface-based approach correctly reproduced the input mixed-mode traction-separation relations when the tractions and separations were tracked. The nonlinear finite element model with the cohesive surface interactions was then used in conjunction with the ELS experiments to determine the mixed-mode traction-separation relations for the silicon/epoxy interface.

2.3 EXTRACTION OF TSR PARAMETERS

The first step in establishing the key parameters in the mixed-mode traction-separation relations was to determine the variation of the phase angle of the mode-mix with epoxy thickness from the results of LEFM analyses and the cohesive zone modeling in comparison with the DIC measurements. Then the resistance curves for three of the ELS specimens shown in Figure 5 were used to extract the parameters of the traction-separation relations that were associated with damage initiation and evolution for three different phase angles. The data for the other three specimens were used to validate the model in Section 2.4. Finally, the range of mode-mix phase angles accessible to this model was extended to pure mode I ($\psi = 0$) by including data from DCB wedge tests of the same interface (Gowrishankar et al. 2012).

2.3.1 Mode Mix

The phase angle of the mode-mix for the ELS specimen is determined from the LEFM analyses with $l = h_e$ in Eq. 2.6 as shown in Figure 8. The semi-analytical method predicts an asymptotic limit (-44°) when the epoxy thickness is very small compared to other in-plane dimensions, as discussed in Section 2.2.3. The fact that this limit phase angle is independent of the epoxy thickness stems from Eq. 2.7 and the choice of the length scale $l = h_e$ in Eq. 2.6, which cancel out the exponential terms in the length scale. On the other hand, the results from the linearly elastic, finite element analyses (Fig. 6b) exhibited a very clear dependence on the epoxy thickness with the phase angles ranging from $-41° \le \psi \le -25.5°$, while respecting the analytical limit as the epoxy thickness tends to zero.

The results from cohesive zone modeling of the ELS specimens (Fig. 6c) with a traction-separation relation that was typical of those subsequently extracted from the experiments compare closely with the LEFM results for the phase angles. In this case, the phase angle was obtained by applying Eq. (2.10) to the displacements at the initial crack tip, which remained a constant for each ESL specimen up to the point of damage initiation. As a result, the pre-damage phase angle is nearly identical to the LEFM value. Thus, based on the cohesive zone modeling, the ELS experiments conducted in this study covered the range $-42° \le \psi \le -26°$ by varying the epoxy thickness.

Following Eq. 2.10, the phase angle of the mode-mix could be determined by measurements of the normal and tangential CTODs, as shown in Fig. 4 by the DIC technique. The CTOD data (Fig. 4b) obtained from the DIC measurements was approximated by two linear fits for each displacement component. In each case, the lower slope was associated with the development of the cohesive zone, while the larger slope was associated with the passage of the traction-free portion of crack faces past the fiducial

marks (Fig. 4a). The phase angles plotted in Figure 8 were obtained from the ratio of the lower slopes from the normal and tangential displacement responses and in essence are an average of the elastic and softening behaviors in the cohesive zone. Apparently, these phase angles were considerably different from those obtained by the LEFM and cohesive zone modeling. As will be seen from later discussion of the finite element solutions, there is more structure to the CTOD data than the linear approximations being made at this stage, but the signal to noise ratio from the DIC measurements was not sufficient to resolve this structure. This may be due to the fact that the fiducial marks were in the silicon adherends, rather than on the crack faces. Since obtaining displacements near such discontinuities is difficult with DIC in general, future efforts at using DIC to determine phase angles should be directed at resolving these issues, most likely by making use of the full field nature of the DIC data.

2.3.2 Damage Initiation

The point of damage initiation in the cohesive zone model is assumed to coincide with the point of observable crack growth by IR-COI measurements in the ELS experiments. This is justified by noting that the normal crack opening is relatively small before damage initiation and thus may not be observable. Moreover, the resolution for the crack growth measurement was about 330 nm. As shown in Figure 9a, the measured crack growth increased considerably from less than 20 nm to about 1 μm after a certain applied displacement, Δ_0, which was taken as the critical loading displacement for damage initiation. Meanwhile, the normal CTOD at the same applied displacement $\delta_n(\Delta_0)$ was measured by IR-COI (Figure 9b). The corresponding J-integral as indicated in the resistance curve (Figure 9c) is then taken to be identical to the elastic part of the fracture toughness in Eq. (2.15), namely, $J_0 = J(\Delta_0) = \Gamma_1 = \frac{1}{2}\sigma_0\delta_0$. For a particular ELS

specimen, the phase angle of mode mix was established in Figure 8 and hence, $\delta_0 = \delta_n(\Delta_0)/|\cos\Psi|$ and $\sigma_0 = 2J_0/\delta_0$. The stiffness of the interaction is then obtained as $K_0 = \sigma_0/\delta_0$, whereas the maximum normal traction is $\sigma_{n0} = K_0\delta_n(\Delta_0)$. Therefore, the stiffness K_0 and the strength σ_{n0} can be extracted for each specimen by combining the measurements of the crack extension and the normal CTOD. The results are listed in Table 1 for three of the six ELS specimens, while the other three specimens will be used for validation (Section 2.4). We note that the extracted values for K_0 and σ_{n0} varied slightly from specimen to specimen. In the mixed-mode cohesive zone model as described in Section 2.2.4, they are independent of mode mix and should be constants for all specimens. As a result, the variations are thus considered as data scattering, and the average values are taken for K_0 and σ_{n0} as the parameters of the cohesive zone model in the subsequent analysis.

2.3.3 Damage Evolution

The damage evolution for each mode-mix (Eq. 2.11) is governed by two additional parameters are required for damage evolution for each mode-mix, δ_f and α. Both may be mode dependent and specified as a tabulated input in ABAQUS. For each ELS specimen, the two parameters were extracted based on the resistance curve and the relation in Eq. (2.16). The steady state J-integral of the resistance curve was taken as the mixed-mode fracture toughness, i.e., $\Gamma(\Psi) = J_{ss}$, and then, $\Gamma_2(\Psi) = J_{ss} - J_0$. Moreover, for a given mode mix with corresponding $\Gamma_1(\Psi)$ and $\Gamma_2(\Psi)$, the crack growth to reach the steady state (Δa_{ss}) depends on the index α, as shown in Figure 10. It was found that $\alpha = 6$ yielded good agreement with the experiments for all specimen in the present study. Once the value of α was selected, the other parameter δ_f was obtained by Eq. (2.16) as

$$\delta_f(\Psi) = \delta_0 + \left(\frac{J_{ss}-J_0}{K_0\delta_0}\right)\frac{\alpha(e^{\alpha}-1)}{e^{\alpha}-1-\alpha} \tag{2.18}$$

Following the above procedure, we were able to extract the following parameters for the mixed-mode traction separation relation from the ELS experiments: stiffness K_0, normal strength σ_{n0}, α and δ_f, as listed in Table 2.1. In addition, we have assumed that shear strength $\sigma_{t0} = 1$GPa. Among all these parameters, only δ_f depended on the mode mix and must be specified by the tabulated input (Table 2). Note that the values of δ_f and δ_0 in Table 2 are slightly different from those in Table 1, since they were re-calculated by using the average values of K_0 and σ_{n0} along with the measure toughness (Γ) for each specimen.

Recall the phase angle of mode mix as defined by Eq. (2.10) ranged from -42° to -26° for the ELS specimens used in the present study (Fig. 8). As a result, the extracted parameters are expected to be applicable only within the same range of mode mix. To extend the range of mode mix, we took advantage of a previous study (Gowrishankar et al. 2012) where nominally mode-I double-cantilever beam (DCB) specimens were used to determine the mode-I traction-separation relation for a similar silicon/epoxy interface. The stiffness was assumed to be 2 GPa/μm, slightly larger than the extracted value (1.33 GPa/μm) in the present study. The maximum normal traction obtained from the DCB specimen was 18 MPa, much lower than the average value (37.3 MPa) from the ELS specimens. This discrepancy may be attributed to the different approaches used to determine the maximum traction. Nevertheless, by the assumptions in the mixed-mode cohesive zone model, we may use the same stiffness (K_0 = 1.33 GPa/μm) and the same strength (σ_{n0} =37.3 MPa) for mode I ($\Psi = 0$). On the other hand, the mode-I fracture toughness was 1.8 J/m^2 by the DCB experiment. Using this fracture toughness, we determine the corresponding δ_f for mode I by Eq. (2.18), where $\delta_0 = \frac{\sigma_{n0}}{K_0} = 0.028$ μm, $J_{ss} = 1.8$ J/m^2, $J_0 = \frac{1}{2}\sigma_{n0}\delta_0 = 0.52$ J/m^2, and $\alpha = 6$. By including the value of δ_f (0.236 μm) for mode I in the tabulated input (Table 2), the range of mode mix is extended

to be between -41° and 0° for the mixed-mode cohesive zone model. Additional experiments would be necessary to further extend the range of mode mix, especially for the cases close to pure mode II ($\Psi = 90°$).

2.4 DISCUSSION

At this stage, we have obtained mixed-mode traction-separation relations for specimens whose epoxy thickness was 5, 9.3 and 50 μm as embodied in the data supplied in Table 1. Although the parameters were extracted from measured crack extension and crack tip opening displacements as well as the resistance curve for each specimen, the average values of the extracted stiffness and normal strength were used for the final slate of parameters listed in Table 2. As a result, the model was first verified by conducting finite element analyses of the same specimens that were used to extract parameters and comparing the results with measurements of their load-displacement responses, normal crack tip opening displacements and the resistance curves. This was followed by applying the same model to the other ELS specimens with different mode-mixes for further validation.

First we compare the results (Fig. 11) for the ELS specimen with an epoxy thickness of 50 μm, which was one of the three specimens used for the parameter extraction. The traction-separation relation that results from the parameters given in Table 2 is shown for reference (Fig. 11a). The dominance of the normal component of the input traction-separation relation is clear at this mode-mix of -26°. The history of the vectorial tractions and separations at the initial crack tip from the finite element analysis was consistent with the input, despite the change of the phase angle during damage evolution. Note that the values of the output shear traction-separation relation were slightly higher than the ones that were input and vice versa for the normal traction-separation relations. However, these

differences cancelled out for the vectorial traction-separation relation. The measured load-displacement response (Fig. 11b) and normal CTOD (Fig. 11c) were captured very well by the model. Note that both the IR-COI measurements and the finite element analysis were able to resolve the normal crack opening displacements sufficiently well to capture the passage of the elastic and softening portions of the cohesive interaction (Fig. 9b also), whereas the current implementation of DIC (Fig. 4b) was not. The fracture resistance curves are compared in Fig. 11d. Here, based on the traction distribution along the interface, the crack extension obtained from the finite element model was the distance between the initial crack tip and the new crack tip defined at the location where the traction was equal to the strength , or where the damage zone ($0 < D < 1$) and the elastic interaction zone ($D = 0$) met. This definition is consistent with the assumption that $J_0 = \Gamma_1$, which was used in Section 4 for parameter extraction. Moreover, the J-integral that was used for extraction of the parameters of the traction-separation relation was based on the beam on elastic foundation (BEF) model, Eq. 2.4. When this equation was used with the load-displacement response obtained from the finite element analysis, the obtained resistance curve agrees closely with the data plotted in Fig. 11d. However, the BEF model is an approximation and does not account for the part of the cohesive zone where damage is evolving. Nonetheless, the contribution of this region to the J-integral can be obtained from the finite element analysis and Eq. 2.12 or 2.13, giving a more accurate J-integral. Note that it is not accessible from the experiments without direct measurements of the tractions and the shear component of CTOD. As shown in Fig. 11d, the BEF approximation correctly predicts the initiation and steady-state values of the J-integral (J_0 and J_{ss}), but underestimates the J-integral for the resistance curve in between.

The stage is now set to determine the traction-separation relations for the same silicon epoxy interface at any mode-mix between 0 and -42° using the measured steady

state toughness $\Gamma(\psi)$ (Figs. 5 & 12) and the input parameters listed in Table 2. The analytical procedure is described and then validated with finite element analyses in comparison with the data obtained from the three ELS specimens that were not used for parameter extraction.

For the case with mode-mix not provided in the tabulated input (Table 2), the parameters of the traction-separation relations can be obtained by interpolation. Let m_1^A and m_1^B be two adjacent energy ratios in the tabulated input. For an energy ratio m_1 in between these two values ($m_1^A < m_1 < m_1^B$), the corresponding critical separation, $\hat{\delta} = \delta_f - \delta_0$, is obtained by linear interpolation between the input values for m_1^A and m_1^B. As a result, the effective critical separation is predicted as a function of mode mix as

$$\hat{\delta}(\psi) = \hat{\delta}_A + \left(\hat{\delta}_B - \hat{\delta}_A\right)\frac{(\cos\psi)^2 - (\cos\psi_A)^2}{(\cos\psi_B)^2 - (\cos\psi_A)^2} \tag{2.19}$$

for $\psi_A < \psi < \psi_B$. Correspondingly, the fracture toughness as a function of the phase angle is: $\Gamma(\psi) = \Gamma_1(\psi) + \Gamma_2(\psi)$, where

$$\Gamma_1(\psi) = \frac{1}{2K_0}\left(\frac{\sigma_{n0}}{\cos\psi}\right)^2 \tag{2.20}$$

and

$$\Gamma_2(\psi) = \frac{\sigma_{n0}\hat{\delta}(\psi)}{\cos\psi}\left(\frac{1}{\alpha} - \frac{1}{e^{\alpha} - 1}\right) \tag{2.21}$$

using the same values of K_0, σ_{n0}, and α. The results of this process are shown as the interpolated variation of the toughness with mode-mix between -42° and 0° (Fig. 12). The phase angles of the three ELS specimens not used for parameter extraction were -31°, -35° and -38°, respectively, and the measured fracture toughness values are in close agreement with the interpolated values. With this interpolation procedure implemented in the finite element model, the same input parameters, including the tabulated data (Table 2) and the values of K_0, σ_{n0}, and σ_{t0} can be used in the finite element analyses for other

experimental configurations. The results are compared with the measurements in Fig. 13 for an ELS specimen whose epoxy thickness was 23.3 μm ($\psi = 31°$). The normal and shear components of the interpolated traction-separation relation are shown first (Fig. 13a). The corresponding vectorial traction-separation relation is compared with the tractions and separations that were obtained from the output of the finite element analysis, once again establishing internal consistency of the model. The computed load-displacement and normal CTODs (Fig. 13 b-c) were in excellent agreement with measurements. The resistance curve (Fig. 13d) with the J-integral computed from the beam on elastic foundation model tracked its measured counterpart well. The J-integral computed using the local tractions and separations at the crack tip rose more quickly to steady state as before. Similar levels of agreement were achieved for the other two ELS specimens. Therefore, it appears that a robust model of mixed-mode fracture between silicon and epoxy has been developed for phase angles between -42° and 0°. All that would be needed to extend the reach of the model would be a toughness measurement at a mode-mix outside this range. Although measurements of normal crack tip opening displacements would provide further validation, they are not required for extending the model. However, the present model is likely to run into trouble for mode-mixes that are close to pure shear, where damage initiation may not be controlled by the normal tractions as assumed in the present study and the shear strength, σ_{t0}, in Eq. 2.9 has to be determined more accurately.

The final point to be made in this discussion relates to the scale of the bridging provided by this silicon/epoxy interface. The data (Fig. 10a) for Δa_{ss}, which corresponds to the length of the cohesive zone as a function of mode-mix, was normalized (Fig. 10b) by the thickness of the silicon strips and compared with the normalized fracture length scale $\bar{l} = \dfrac{\bar{E}\Gamma}{\sigma_0^2 h_{si}}$ (Parmigiani and Thouless 2007). When the strength σ_0, which was

independent of the mode-mix and was obtained from the parameter extraction exercise and the measured values of the toughness Γ (Figs. 5 & 12) were used in the expression, the normalized fracture length scale ranged (Fig. 10b) from about 0.7 to 2.7, while the normalized cohesive zone lengths represented by Δa_{ss} ranged from 2 to 2.8. The difference can be attributed to the fact that the fracture length scale parameter l is useful for general scaling arguments, whereas Δa_{ss} is specific to the case at hand. It has been shown, (Parmigiani and Thouless 2007) that, when the ratio of shear toughness is ten times that associated with tensile fracture, small scale bridging can be achieved for $\bar{l}$ values of 100. From Fig. 12, we expect a much larger ratio of toughness values and small scale bridging to occur for one to two lower orders of $\bar{l}$. This means that large scale bridging was indeed in effect for the silicon/epoxy interface being considered here. This may further explain the discrepancy between the phase angles obtained from DIC (Fig. 8) and the values obtained from the LEFM analyses. Nonetheless, even under large scale bridging, the phase angles obtained from the linearly elastic portion of the traction-separation relations do still make close reference to values obtained from LEFM analyses. This is not surprising based on the results presented in Fig. 9b of Parmigiani and Thouless (2007), but it does provide a convenient and common point of reference for phase angles obtained from the two approaches.

Some of the additional results including the comparison between experiment and FEA with extracted TSR input were shown in Figure 14 and 15 for specimens with 5 and 9.3 μm, respectively. Figure 16 and 17 showed the comparison of experimental and FEA results with tabular input for the cases with epoxy thickness of 8 and 12 μm, respectively.

2.5 CONCLUSIONS

This work builds on a previous characterization of the traction-separation relations of a silicon/epoxy interface that was separated under nominally mode I conditions (Gowrishankar et al. 2012). In the present work, mixed-mode conditions were provided by an end-loaded-split (ELS) configuration, where the epoxy was sandwiched between two silicon strips. The mode-mix provided by the ELS configuration was varied by varying the thickness of the epoxy layer. A series of experiments were conducted under displacement control. The normal crack opening displacements in the interior of the specimen were measured by infra-red crack opening interferometry. In some experiments, digital image correlation was used to measure the crack-tip displacements in both the normal and tangential directions. Finite element models were developed that accounted for the elastic behavior of the silicon and epoxy and the interactions between them using a damage-based cohesive zone model. The key parameters for the traction-separation relations were extracted from the measured resistance curves and normal crack opening displacements along with finite element solutions for a range of values of the softening parameter.

For the range of mode-mix considered here (-42° to 0°), it was noted that, although the steady state toughness was a function of the mode-mix, the elastic behavior, normal and shear strengths and the softening parameter were not. The mixed-mode traction-separation relations from this model were validated by comparing to the ELS experiments using epoxy thickness values and associated phase angles that were not used for parameter extraction. The load-displacement responses, normal crack tip opening displacements and resistance curves were all captured very well. Interestingly, resistance curves based on J-integral calculations that also accounted for the damaging portion of the traction-separation relations had a different shape between J_0 and J_{ss} than those that were only based on the elastic foundation analyses. This is to be expected, although the measurement-based

parameter extraction was, and can only be, founded on the latter, and the J-integral obtained locally from the path surrounding the cohesive zone provides the actual resistance curve for the silicon/epoxy interface.

CHAPTER 3: CHARACTERIZING INTERFACIAL SLIDING OF THROUGH-SILICON-VIA BY NANO-INDENTATION

In this Chapter, an experimental method is proposed to determine the shear sliding behavior of the interface between a copper through-silicon-via (TSV) and silicon. This interface was loaded in a nano-indentation experiment on specimens that were fabricated using focused-ion-beam (FIB) milling. The elastic and plastic properties of the copper via were first characterized by micro-pillar compression experiments. The interfacial sliding is described by a cohesive zone model with a traction-separation relation including a linearly elastic part followed by frictional sliding at a constant shear traction. Both analytical and numerical models were developed for extracting the parameters of the traction-separation relation for the shear behavior of the interface. The traction-separation relation with the extracted parameters may be used to study via extrusion and associated reliability analysis for integrated TSV structures.

3.1 INTRODUCTION

3D integration emerged as a solution to the wiring limits imposed on chip performance, power dissipation, and packaging form factor beyond the 14 nm technology node (Garrou et al. 2012). The through-silicon-via (TSV) is critical as it improves the chip-performance by providing short vertical interconnects. However, the mismatch of thermal expansion coefficients (CTE) between Cu vias and Si wafers can induce considerable levels of thermal stress which impairs device performance and reliability (Jiang et al. 2015). One particular concern is Cu extrusion (De Wolf et al. 2011, Heryanto et al. 2012, Messemaeker et al. 2013, Jiang et al. 2015) induced by the thermal stresses, which often causes failure in TSVs and neighboring structures during fabrication or thermal cycling. Early research suggested that the via extrusion can be suppressed or reduced by enhancing

the bonding behavior between TSV and silicon in sliding resistance (De Wolf et al. 2011). However, it is quite challenging to experimentally characterize the sliding behavior of the interface between copper TSV and silicon. In this work, a characterization method was proposed using nano-indentation.

The proposed method may be considered as a variation of the fiber pushout test which is commonly known for characterizing fiber/matrix interfaces in composite materials (Bechel et al. 1998). The dimensions of TSVs make the nano-indentation experiment ideal for characterizing their properties and interactions with the silicon matrix. At this scale, similar experiments have been used to examine the compressive behavior of micro pillars. Typically, the micro-scale experiments are prepared through focused ion beam (FIB) milling (Bei et al. 2007), which is very suitable for both copper and silicon (Alexandre et al. 2008) due to their excellent responsiveness to FIB. Still, challenges exist in fabricating the sample on existing TSV structures without damaging the interface or Cu via of interest.

A variety of analytical investigations have been conducted on similar pushout problems. The most successful approach is the one based on shear lag theory (Shetty 1998, Hutchinson and Jensen 1990). There are couple of assumptions are involved in this theory; the end effects are often neglected and the radial stress is considered to be uniform. However limited by these assumptions, the shear lag theory provides a closed-form solution of the problem. Finite element modeling is also commonly used for this type of problem (Liang and Hutchinson 1993) to characterize the energy release rate and sliding friction of the fiber-matrix interface. In this work, both LEFM and CZM were used to determine the TSR of TSV/Si interface.

3.2 EXPERIMENT

Two different experiments were conducted: (1) copper micro-pillar compression experiment; (2) copper via pushout experiment. The micro-pillar experiment was used to determine the elastic and plastic properties of the copper via, while the pushout experiment revealed the interfacial sliding behavior between the via and its silicon matrix. Both experiments were conducted using a nano-indenter (Agilent XP) with a truncated cone probe as the loading device. The specimens were prepared from an integrated TSV structure using a FIB/SEM dual beam system, which contains both ion beam and electron beam columns, intersecting at an angle of 52°. This allowed the specimens to be milled with accurate control of depth.

3.2.1 Material Properties

The as-received TSV structure contained periodic arrays of blind Cu vias in a 780 μm (001) Si wafer (Fig. 18). The nominal via diameter and depth were 10 and 55 μm, respectively. The spacing between the copper vias was 40 μm along the (100) direction and 50 μm along the (110) direction of the silicon wafer. To prepare the micro-pillar specimen, the silicon wafer was diced and polished until one row of the vias was about 20 μm away from the polished side. For each micro-pillar specimen, the top 100 nm was milled off in order to eliminate the effect of surface roughness. Then the silicon surrounding the selected via was milled down by 3 μm in a concentric ring. The inner radius was the same as the via diameter (10 μm). The outer radius was 18 μm. Subsequently, a second ring pattern with a smaller outer radius (13 μm) was used to mill off the silicon immediately surrounding the copper pillar to a nominal depth of 55 μm. Finally, additional silicon was removed to expose the side of the micro-pillar (Fig. 19). Due to the ion beam divergence, the obtained copper micro-pillar was tapered by an angle of 2° with a 6-μm diameter at the top.

The micro-pillar compression experiment was conducted using the nano-indenter with a truncated cone probe with an 8 μm tip diameter at a rate of 1 nm/s. A total of three loading/unloading cycles were applied with prescribed maximum displacements of 500, 1800, and 6000 nm. The force-displacement responses are shown in Figure 22. For comparison, a finite element analysis was conducted to simulate the elastic-plastic deformation of the copper micro-pillar, adopting the associated flow model with isotropic hardening (ABAQUS®, V6.14). The Ramberg-Osgood equation was used to describe the relationship between the plastic strain and stress:

$$\varepsilon_p = \frac{3}{7}\frac{\sigma_e}{E}\left(\frac{\sigma_e}{\sigma_0}\right)^{n-1}, \tag{3.1}$$

where ε_p is the equivalent plastic strain, σ_e is the equivalent stress, σ_0 is the yield stress, E is Young's modulus, and n is the hardening exponent. For the copper via, we set E to be 110 GPa and determined σ_0 and n based on the load-displacement response from the micro-pillar compression experiment. By taking the yield stress to be 216 MPa and the hardening exponent to be 3, the finite element analysis yielded a force-displacement response which is in close agreement with the experimental data (Fig. 22). The corresponding von Mises stress and equivalent plastic strains are shown in Figure 23a, with contour plots showing a slight gradient due to the tapered cross-section of the micro-pillar specimen. For the same nominal yield strength, higher hardening exponents lead to softer force-displacement responses (Fig. 23b). The obtained strain hardening exponent $(n = 3)$ is smaller than the typical value of 5 for bulk copper (Callister and Rethwisch, 2014), indicating that the copper TSVs have a stronger hardening response, possibly due to relatively small grain sizes (Jiang et al., 2015).

3.2.2 Via Pushout Experiment

The specimen preparation for the via pushout experiments (Fig. 24) was similar to the preparation of the micro-pillar specimens. About 100 nm of surface material was first removed to obtain a smooth top surface (Fig. 24a). The ring pattern milling was then performed to obtain a 3 μm free-standing portion of the via (Fig. 24b). An annular wedge crack with a draft angle of 3° was introduced by controlling the beam energy to 30 kPa with a working distance of 7 mm (Fig. 24c). The resulting annular crack was about 1μm as shown in Figure 24d. After this, the blind via was turned into a through via (Fig. 24 e-f) by milling away the silicon and copper from the side at 6 μm below the front of the annular crack. The final specimen is shown in Figure 25, which has a total via length of 9 μm and a bonded length of 5 μm.

The pushout experiment was performed with the truncated cone tip under a prescribed displacement loading protocol of 1 nm/s. The force-displacement responses for three specimens are shown in Figure 26. When the force was lower than 6 mN, there was a linearly elastic relationship between the force and displacement. This indicates that the copper via remained elastic and no crack growth had occurred. Once the force level exceeded 6 mN, a slightly nonlinear response can be observed, which could be the result of either copper plasticity or crack growth or both. Remarkably, the force reached a peak value of approximately 12 mN, followed by a sudden drop under the displacement-controlled loading, which was most likely due to unstable crack growth along the interface. Subsequently, the indentation force remained constant (~4 mN) as the indenter continued pushing the via, which suggests frictional sliding between the via and the surrounding silicon. Unloading at this stage showed elastic characteristics with the same slope as the initial elastic response. Based on the average measured peak force (~12 mN), the interfacial shear strength was initially estimated to be 76 MPa, assuming a contact area based on the

bonded length and the via diameter. The constant sliding force provided an estimate of the steady-state frictional shear strength of about 25 MPa.

Moreover, SEM images of the specimen (Fig. 27a) after the pushout experiment show clear evidence of interfacial sliding but no severe plastic deformation at the top of the via. This suggests that plastic deformation of the copper via was limited due to relatively low indentation forces. On the other hand, with an initial crack at the interface and a relatively small interfacial area, the force was sufficient to cause unstable crack growth along the interface and subsequent frictional sliding.

The interface was further examined using energy-dispersive X-ray spectroscopy (EDS) after pushing the via out to expose the via side of the interface through the etching window (Fig. 25b). The red dashed square identifies the region (Fig. 25 b) where the spot for the EDS spectrum (Fig. 25c) was located. The obtained composition data are listed in Table 1, where it can be seen that the strongest signal was from copper (74.3%), followed by silicon (10.8%) and tantalum (1.1%). Tantalum is commonly used as a barrier layer between the copper via and the silicon matrix. The presence of silicon on the via side of the interface suggests that the crack growth and sliding occurred close to the interface between silicon and the tantalum barrier layer as illustrated schematically in Figure 25d. Note that the EDS signals are based on back scattered electrons from the copper which pass through the tantalum and silicon on their way to the sensor.

3.3 Analysis and Results

The stress and fracture analyses associated with the via pushout experiment were conducted at three levels. The first was a shear lag analysis, which was motivated by the measured load-displacement response. This was followed by finite element analyses, first

based on linearly elastic fracture mechanics and then a specialized cohesive zone model, both using the commercial finite element code ABAQUS®.

3.3.1 Shear Lag Analysis

In developing a shear lag analysis for the TSV pushout experiment (Fig. 26a), it was assumed that the indenter was a rigid flat punch that provided a uniform normal traction and end displacement (Δ) to the top of the via. The copper via was assumed to be linearly elastic in a rigid silicon matrix. The force balance for an element of the via (Fig. 26b) relates the shear traction (τ) at interface to the axial stress (σ_f) in the via through

$$\tau = \frac{D_f}{4}\frac{d\sigma_f}{dx}, \tag{3.2}$$

where D_f is the via diameter. The axial stress in the via is related to its axial displacement (δ) through Hooke's law of elasticity:

$$\sigma_f = E_f \frac{d\delta}{dx}, \tag{3.3}$$

where E_f is Young's modulus of copper.

Motivated by the measured load-displacement response, the interface between the via and silicon was assumed to follow a shear traction-separation relation with two segments (Fig. 26c), first linearly elastic (before fracture) and then a constant traction for frictional sliding. i.e.,

$$\tau = \begin{cases} k\delta, & \delta \le \delta_0 \\ \tau_c, & \delta_0 < \delta \end{cases}, \tag{3.4}$$

where k is the initial stiffness of the interface, δ_0 is the critical separation for fracture, and τ_c is the frictional shear strength of the interface. Correspondingly, the peak traction is $\tau_0 = k\delta_0$.

When the end displacement $\Delta < \delta_0$, the axial displacement δ is less than δ_0 everywhere and thus the traction-separation relation is linearly elastic. In this case, substituting Eq. (3.3) and (3.4) into (3.2) results in

$$\frac{E_f D_f}{4k}\frac{d^2\delta}{dx^2} = \delta . \tag{3.5}$$

Solving Eq. (3.4) with proper boundary conditions, we obtain that

$$\delta = \Delta \frac{\cosh\left(\frac{x}{\lambda}\right)}{\cosh\left(\frac{H}{\lambda}\right)}, \tag{3.6}$$

where $\lambda = \sqrt{\frac{E_f D_f}{4k}}$ is a characteristic length and H is the bonded length of the specimen. Here we used two boundary conditions: end displacement on top ($\delta = \Delta$ at $x = H$) and zero axial force at bottom ($\sigma_f = 0$ at $x = 0$). The corresponding axial stress in the via is then obtained by inserting Eq. (3.6) into (3.3), and the resultant indentation force is

$$P = \frac{\pi}{4} D_f^2 \sigma_f = \frac{\pi D_f^2 E_f \Delta}{4\lambda} \tanh\left(\frac{H}{\lambda}\right), \tag{3.7}$$

which gives a linear force-displacement relation as the first stage of the pushout experiment.

When the applied end displacement $\Delta > \delta_0$, part of the interface undergoes frictional sliding with $\delta > \delta_0$ while the other part remains linearly elastic with $\delta < \delta_0$. Let H_1 be the length of the via where the interface remains linearly elastic (Fig. 26a). For this part ($0 < x < H_1$), we solve Eq. (3.4) to obtain

$$\delta = \delta_0 \frac{\cosh\left(\frac{x}{\lambda}\right)}{\cosh\left(\frac{H_1}{\lambda}\right)}, \tag{3.8}$$

where the displacement is set to be δ_0 at $x = H_1$. For the upper part ($H_1 < x < H$), the constant shear traction in Eq. (3.4) is substituted into Eq. (3.2), which leads to

$$\frac{E_f D_f}{4}\frac{d^2\delta}{dx^2} = \tau_c, \tag{3.9}$$

Solving Eq. (3.9) we obtain

$$\delta = \frac{2\tau_c}{E_f D_f}x^2 + C_1 x + C_2, \tag{3.10}$$

where C_1 and C_2 are coefficients to be determined from the boundary conditions. Applying the displacement and stress continuity conditions at $x = H_1$, we obtain

$$\begin{aligned} C_1 &= \frac{\delta_0}{\lambda}\tanh\left(\frac{H_1}{\lambda}\right) - \frac{4\tau_c H_1}{E_f D_f} \\ C_2 &= \delta_0\left[1 - \frac{H_1}{\lambda}\tanh\left(\frac{H_1}{\lambda}\right)\right] + \frac{2\tau_c H_1^2}{E_f D_f} \end{aligned} \tag{3.11}$$

Furthermore, applying the end displacement condition at $x = H$, we obtain an equation for determining H_1 or equivalently, the sliding zone size $c = H - H_1$:

$$f = \frac{\Delta}{\delta_0} - 1 - \tanh\left(\frac{H-c}{\lambda}\right)\frac{c}{\lambda} - \frac{2\tau_c}{E_f D_f \delta_0}c^2 = 0. \tag{3.12}$$

Acceptable values of c (i.e., $0 < c < H$) are obtained from Eq. (3.12) when $\Delta > \delta_0$ and $\Delta < \Delta_c$, where

$$\Delta_c = \delta_0 + \frac{2\tau_c}{E_f D_f}H^2. \tag{3.13}$$

Correspondingly, the indentation force is obtained as

$$P = \frac{\pi}{4}D_f^2\sigma_f = \frac{\pi D_f^2}{4}\left[\frac{4\tau_c c}{D_f} + E_f\frac{\delta_0}{\lambda}\tanh\left(\frac{H-c}{\lambda}\right)\right]. \tag{3.14}$$

When $\Delta \geq \Delta_c$, the entire interface undergoes frictional sliding ($c = H$). In this case, we have

$$P = \pi D_f \tau_c H, \tag{3.15}$$

which is a constant, independent of Δ.

The force-displacement response of the push-out experiment predicted by the shear lag model consists of three segments: a linearly elastic segment (Eq. 3.7), an intermediate nonlinear segment (Eq. 3.14), and a constant force segment (Eq. 3.15). It is found that the force-displacement response depends sensitively on the bonded length (H) of the specimen (Fig. 27). In this case, we take $\delta_0 = 100\text{nm}$, $k = 0.8$ MPa/nm and $\tau_c = 25\text{MPa}$ for discussion. With the same traction-separation relation, a larger bonded length results in a stiffer initial load-displacement response and hence higher loads in all three segments. The response in the second segment is of particular interest, where the interface is partially elastic and partially frictional. For a relatively long specimen ($\text{H} > 20\ \mu\text{m}$), the force increases as the indenter displacement increases, but the slope is lower than the elastic segment. For a shorter specimen ($\text{H} < 20\ \mu\text{m}$), the force decreases with increasing displacement. In all cases, the force drops abruptly at $\Delta = \Delta_c$, after which the interface is fully frictional and the force remains constant. The discontinuous drop of the indentation force is a result of the assumed discontinuous traction-separation relation for the interface. By Eq. (3.12), there are two possible solutions for the sliding zone size *c*. Prior to the drop ($\Delta < \Delta_c$), one solution is greater than the bonded length and thus eliminated. When $\Delta = \Delta_c$, both solutions are acceptable and one of them corresponds to the fully sliding case with $c = H$. As a result, the associated indentation force drops abruptly from the partially sliding solution to the fully sliding solution.

Interestingly, the shear-lag analysis predicts that the intermediate segment between the linearly elastic ($\Delta < \delta_0$) and fully frictional ($\Delta \geq \Delta_c$) segments of the force-displacement response diminishes as the specimen length decreases. For $\text{H} = 5\,\mu\text{m}$, the force-displacement response appears to have only two segments as the intermediate segment becomes negligibly small. In this case, $\frac{\Delta_c - \delta_0}{\delta_0} = \frac{2\tau_c}{E_f D_f \delta_0} H^2 << 1$, and the force-

displacement response from the indentation experiment can be directly converted to the traction-separation relation of the interface. Specifically, the slope of the linearly elastic response can be used to determine the stiffness *k* via Eq. (3.7), the displacement at the peak force gives the critical separation δ_0, and the constant force in the fully frictional segment can be converted to the frictional shear strength τ_c by Eq. (3.15). Moreover, the peak shear traction can be extracted approximately from experiment as

$$\tau_0 = \frac{P_{\max}}{\pi D_f H}, \tag{3.16}$$

where $P_{\max}$ is the peak force. It should be noted here that Eq. (3.16) only applies to short bonded lengths as an approximation to Eq. (3.14) with $c = 0$. In terms of designing the TSV specimen for the pushout experiment, perhaps the most important implication of the shear-lag analysis is that short vias are preferable for directly extracting interfacial parameters from the measured load-displacement response. Thus the bonded length of the specimen was selected to be 5 μm, with which the shear lag analysis was used to obtain a good estimate of the parameters as listed in Table 4.

3.3.2 Linearly Elastic Fracture Analysis

A linearly elastic fracture analysis was conducted using the finite element package ABAQUS® in order to obtain the fracture toughness of the TSV/silicon interface and the corresponding mode-mix in the via pushout experiment. In addition, the potential for using compliance measurements as a way of measuring the crack length was explored.

The approach followed the one outlined in Liang and Hutchinson's work (1993). The model was axisymmetric (Fig. 29a) and assumed that the copper via, silicon matrix, and the diamond indenter were all linearly elastic and isotropic. The material properties used in the finite element model are listed in Table 5. The initial crack length was 1μm in order to match the experimental configuration and the crack faces were modeled by contact

surfaces in view of the potential for crack face contact under mode II dominant conditions (Comninou and Dundurs 1980, Dundurs 1978). Eight-node quadratic elements were used for all the elements except those at the crack tip, which were singular elements. The indenter load was set at 12 mN, corresponding to the average peak value of the load measured in the experiment. The geometrical and mesh details of the finite element model are shown in Figure 28a. The corresponding values of the stress intensity factors were obtained as: $K_{IC} = -0.56\ \text{GPa}\sqrt{\text{m}}$ and $K_{IIC} = 0.98\ \text{GPa}\sqrt{\text{m}}$. The negative value of the mode-I stress intensity factor indicates that there was indeed contact between the crack surfaces and fracture occurred under the mode II (shear) condition. The corresponding value of the J-integral (not accounting for the negative mode I stress intensity factor) was 7.9 J/m^2, which is therefore viewed as the mode II fracture toughness (J_{II}) of the TSV/silicon interface. Similar values of the fracture toughness were obtained from the shear-lag analysis as listed in Table 2, by integrating the traction-separation relation up to the maximum shear traction, i.e., $J_{II} = \tau_0 \delta_0 / 2$. From the shear stress contours (Fig. 28c), the highest shear stresses occurred at both the crack tip and the bimaterial corner between the copper and silicon at the bottom of the via. Furthermore, based on this linearly elastic analysis, the stresses exceeded the shear yield strength of the copper (216 MPa) along the entire interface which was the motivation for including the plasticity effects in the next section.

The potential for using specimen compliance to track the crack length was explored by conducting finite element analyses of stationary cracks ranging from 50 nm to 4 μm for a 5- μm via. The compliance only increased by about 3% for cracks ranging from 50 nm to 1 μm (Fig. 29) but increased sharply thereafter. For displacement control, this means that the J-integral also increases with increasing crack length, which is an unstable situation. As indicated earlier, the initial crack from FIB was 1 μm and unstable growth

was in fact observed in the experiments. Furthermore, the modest increase in compliance from the initial crack length made compliance measurements of crack length in the experiment unrealistic.

3.3.3 Cohesive Zone Analysis

Nonlinear finite element analysis with cohesive zone modeling provides another way to extract the interfacial properties. In doing so, it is no longer necessary to assume that the matrix is rigid. It also allows any plastic deformations in the copper to be accounted for. The finite element code ABAQUS® was again used for the analysis although the mesh was slightly modified (Fig. 28b) in order to accommodate cohesive elements ahead of the initial crack front. The silicon was still assumed to be linearly elastic and isotropic, but the stress-strain behavior of the copper followed the constitutive behavior that was extracted from the micro pillar experiment (Fig. 20). A user-defined cohesive element (UEL) subroutine was developed for the interface. Each cohesive element has four nodes, with two nodes shared with the corner nodes of a bulk silicon element and the other two with a bulk copper element. In the traction-separation relation, the separation δ is defined as the relative vectorial displacement between the nodes that are connected to the silicon and copper. In this work, it was assumed that the elastic portion of the normal and shear interactions had the same stiffness k, which ensures that the traction and displacement vectors are aligned (Wu et al. 2016). This gives a normal traction-separation relation as $\sigma = k\delta_n$ for both tension and compression. The strength in the normal direction was assumed to be infinite. However, the shear interaction had a finite strength $\tau_0 = k\delta_0$ corresponding to onset of sliding at a relative shear displacement δ_0. The frictional sliding shear strength was set to be τ_c when the relative shear displacement is greater than δ_0.

To compare with the load-displacement responses in experiments, we set τ_c to be 25 MPa as before and slightly varied the other parameters (δ_0 and k) to best fit the response before frictional sliding. This scheme led to an average peak shear traction of 77.2 MPa for the onset of sliding. The extracted parameters are compared with those obtained using the analytical approach in Table 5. It can be seen that the two sets of extracted parameters are in close agreement. It is worth noting here that the average J-integral calculated from the traction-separation relation prior to sliding is about 7.06 J/m^2, which is close to that obtained by the LEFM analysis. This shows the consistency between LEFM and cohesive zone modeling approaches on the critical J-integral. The agreement in the extracted strength values is due to the short via and the resulting unique and striking features of the force-displacement response. Both the compliance of the matrix and plasticity in the via may contribute to the stiffness of the load-displacement response. However, since τ_0 was about a third of the yield strength of the copper, the amount of plastic deformation turned out to be small. The extent of plastic deformation can be seen in the distributions of the von Misses stress and equivalent plastic strain (Fig. 30) at the peak load. It can be seen that the plastic strain was highly localized near the crack tip and therefore did not affect the global force-displacement response (Fig. 31). The numerical model also accounted for the compliance of the elastic matrix, which led to an approximately 13% increase in the stiffness of the traction-separation relation and correspondingly a smaller value for δ_0 compared to the shear lag analysis.

For the frictional sliding part, a coefficient of friction may be estimated as $\mu = \tau_c / \sigma_c$, where σ_c is the compressive normal traction at the interface and is mainly caused by the mismatch of thermal expansion between the copper via and the silicon wafer. From the analytical model developed in (Jiang et al. 2013), the normal traction can be estimated as

$$\sigma_c = -\Delta T(\alpha_{Cu} - \alpha_{Si})\left(\frac{1-\nu_{Cu}}{E_{Cu}} + \frac{1+\nu_{Si}}{E_{Si}}\right)^{-1}, \tag{3.17}$$

where ΔT is the temperature change (~250˚C) during the manufacturing process, and the coefficients of thermal expansion are: $\alpha_{Cu} = 17\,\text{ppm/˚C}$ and $\alpha_{Si} = 2.3\,\text{ppm/˚C}$. Note that there is another contribution to the radial traction at the interface which is due to the indentation itself. However, this was found to be more than one order of magnitude lower than the thermal contribution and hence ignored. With the extracted frictional shear strength $\tau_c = 25$ MPa, the coefficient of friction was then estimated to be 0.089.

3.4 CONCLUSIONS

This chapter has described the development of a pushout experiment to extract the shear interactions between a copper TSV and silicon. Specimens were fabricated by identifying selected vias and using FIB to etch away the silicon beneath the vias and create an initial circumferential crack between the copper and silicon. A nano indenter was then aligned with each via in turn so that they could be pushed out of the silicon matrix under displacement control. A shear lag analysis was used to develop the optimum geometry that would allow the parameters associated with the shear interaction between copper and silicon to be extracted directly and provide good initial estimates of the traction and relative displacement for the initiation of slip as well as the frictional shear strength of the interface. This claim was validated by conducting a cohesive zone analysis of the pushout experiment that accounted for the plasticity in the copper via and the shear interaction between copper and silicon. The shear traction required to initiate slip was 80.5 MPa and the corresponding relative displacement across the interface was 179 nm, while the frictional shear stress during slip was 25 MPa. Energy-dispersive X-ray spectroscopy suggested that the locus of failure was in the silicon matrix very close to the tantalum adhesion promoting layer.

CHAPTER 4: DIRECT EXTRACTION OF MIXED-MODE TSR USING ONLY FAR-FIELD MEASUREMENTS

This chapter presents a direct method using only far-field data such as load-displacement and end-rotation responses. First, an Euler-beam analysis was conducted showing that, under a balanced condition, the governing equations for the normal and shear interactions between the fracture surfaces of a laminated beam specimen can be decoupled to allow calculation of the corresponding J-integrals and crack tip displacements using far-field measurements. The mixed-mode TSRs can then be determined directly without local measurements. Subsequently, an experimental approach was developed for a wide range of mode mix at an epoxy/silicon interface by making use of asymmetric ELS and ENF specimens. The extracted TSRs were then implemented as a user-defined cohesive element (UEL) for finite element analyses with decoupled normal and shear interactions. Close agreement between the numerical with experimental results validated the proposed scheme. Further analysis of the extracted TSRs was conducted in order to develop an interpolation scheme of the TSRs at any mode-mix within the range of the characterizing experiments.

4.1 THEORY AND ANALYSIS

The problem of interest consists of a laminated beam specimen with one end clamped and the other end loaded as shown in Figure 35a. The initial crack length along the interface between the two adherend beams is designated as a. The load, displacement, and end-rotations are labeled as P_1, Δ_1, θ_1 for the top adherend and P_2, Δ_2, θ_2 for the bottom one. The origin of the coordinate system was set at the initial crack tip with the x direction pointing towards to the loaded ends. The analysis is conducted based on classical Euler-beam theory.

4.1.1 Kinematics

Considering an infinitesimal section of the specimen as shown in Figure 35b, the displacement fields in top and bottom adherend are approximately

$$u_1(x, z_1) = u_{10} - z_1 \frac{dw_1}{dx}, \quad w_1 = w_1(x, 0) \tag{4.1}$$

$$u_2(x, z_2) = u_{20} - z_2 \frac{dw_2}{dx}, \quad w_2 = w_2(x, 0) \tag{4.2}$$

where u_{i0} $(i = 1, 2)$ are the axial displacements at the neutral axis of each adherend, and w_i is the lateral deflection of each adherend. As a result, the relative normal and shear displacements across the interface are,

$$\delta_n = w_1 - w_2 \quad \text{and} \quad \delta_t = u_{1b} - u_{2t}, \tag{4.3}$$

respectively, with

$$u_{1b} = u_{10} + \frac{h_1}{2}\frac{dw_1}{dx}, \tag{4.4}$$

$$u_{2t} = u_{20} - \frac{h_2}{2}\frac{dw_2}{dx}. \tag{4.5}$$

Note that, in this approach, if there is an adhesive layer between the adherends, δ_n, δ_t would include the deformation of the adhesive as well as those of the interfaces with the upper and lower adherends. A scheme for subtracting out the deformation of any interlayer is discussed later in Section 4.5.

4.1.2 Constitutive relation

Assuming linearly elastic constitutive relations in both the top and bottom adherends, we have the force-displacement relationships as,

$$N_i = A_i \frac{du_{i0}}{dx}, \quad M_i = D_i \frac{d^2 w_i}{dx^2}, \quad A_i = \frac{E_i h_i}{1 - \nu_i^2}, \quad D_i = \frac{E_i h_i^3}{12(1 - \nu_i^2)}, \tag{4.6}$$

where N_i and A_i are the axial force and stiffness for each adherend, M_i and D_i are the moment and bending stiffness for each adherend, v_i and h_i are the Poisson's ratio and thickness of each beam.

4.1.3 Equilibrium

The equilibrium of an infinitesimal section is shown in Figure 4.1b. We thus have,

$$\frac{dN_1}{dx} = \tau \quad \text{and} \quad \frac{dN_2}{dx} = -\tau\,, \tag{4.7}$$

$$\frac{dQ_1}{dx} = -\sigma \quad \text{and} \quad \frac{dQ_2}{dx} = \sigma\,, \tag{4.8}$$

$$\frac{dM_1}{dx} = Q_1 + \frac{h_1}{2}\tau \quad \text{and} \quad \frac{dM_2}{dx} = Q_2 + \frac{h_2}{2}\tau\,, \tag{4.9}$$

where Q_i is the shear force for each adherend, and σ, τ are the normal and shear tractions along the interface between the upper and lower beams.

4.1.4 Governing Equation

Taking the second and first derivatives of the relative normal and shear displacements in Eq. (4.3), respectively, we obtain the corresponding governing equations as follows,

$$\delta_n'' = w_1'' - w_2'' = \frac{M_1}{D_1} - \frac{M_2}{D_2}, \tag{4.10}$$

$$\delta_t' = \frac{N_1}{A_1} - \frac{N_2}{A_2} + \frac{h_1}{2D_1}M_1 + \frac{h_2}{2D_2}M_2. \tag{4.11}$$

4.1.5 J-integral and CTOD

Under a generally mixed-mode condition, the path-independent J-integral can be calculated with a contour enclosing the entire cohesive zone around the crack tip. Taking the contour to immediately follow the interacting surfaces ahead of the crack tip, the J-integral can be separated into two parts for the normal and shear interactions, or mode-I and mode-II components as,

$$J_{\mathrm{I}} = \int_{-\infty}^{0} \sigma \left(\frac{d\delta_n}{dx} \right) dx = \int_{0}^{\delta_n^*} \sigma d\delta_n \,, \tag{4.12.1}$$

and

$$J_{\mathrm{II}} = \int_{-\infty}^{0} \tau \left(\frac{d\delta_t}{dx} \right) dx = \int_{0}^{\delta_t^*} \tau d\delta_t \,, \tag{4.12.2}$$

where δ_n^* and δ_t^* are the normal and shear separations at the initial crack tip ($x = 0$). The tractions (σ and τ) in general are functions of the separations in both directions. The energy release rate of crack growth is then given by the total J-integral, $J = J_{\mathrm{I}} + J_{\mathrm{II}}$.

The second derivative of δ_t with respect to x can be obtained from Eq. (4.11) along with Eq. (4.7) and (4.9), yielding

$$\delta_t'' - \left(\frac{h_1}{2D_1} Q_1 + \frac{h_2}{2D_2} Q_2 \right) = \left(\frac{1}{A_1} + \frac{1}{A_2} + \frac{h_1^2}{4D_1} + \frac{h_2^2}{4D_2} \right) \tau \,. \tag{4.13.1}$$

For the laminated beam specimen, Eq. (4.8) can be integrated to obtain the shear forces in terms of the normal tractions and the applied forces at the loading end, with which Eq. (4.13.1) becomes

$$\delta_t'' + \left(\frac{P_1 h_1}{2D_1} + \frac{P_2 h_2}{2D_2} \right) + \left(\frac{h_2}{2D_2} - \frac{h_1}{2D_1} \right) \int \sigma dx = \left(\frac{1}{A_1} + \frac{1}{A_2} + \frac{h_1^2}{4D_1} + \frac{h_2^2}{4D_2} \right) \tau \,. \tag{4.13.2}$$

To eliminate the coupling with the normal tractions in Eq. (4.13.2), we define a balanced condition:

$$\frac{h_1}{D_1} = \frac{h_2}{D_2} \,. \tag{4.14}$$

Such a condition can be fulfilled by designing the laminated beam specimen using various materials and corresponding thicknesses for the two adherends, as discussed later in Section 4.2. It can be shown that when this condition is satisfied, the governing equations for shear and normal displacements are decoupled.

Under the balanced condition, Eq. (4.13.2) becomes

$$\delta_t'' + \frac{h_1}{2D_1} P = \left(\frac{1}{A_1} + \frac{1}{A_2} + \frac{h_1^2}{4D_1} + \frac{h_2^2}{4D_2} \right) \tau \,. \tag{4.15}$$

where $P = P_1 + P_2$. Then, the shear traction can be written as,

$$\tau = \hat{A} \left[\delta_t'' + \frac{h_1}{2D_1} P \right], \tag{4.16}$$

where $\hat{A} \equiv \left(\frac{1}{A_1} + \frac{1}{A_2} + \frac{h_1^2}{4D_1} + \frac{h_2^2}{4D_2} \right)^{-1}$. We then substitute Eq. (4.16) into Eq. (4.12.2) to obtain the mode-II J-integral as,

$$\begin{aligned} J_{\mathrm{II}} &= \int_0^{\delta_t^*} \tau d\delta_t = \hat{A} \int_0^{\delta_t^*} \left[\delta_t'' + \frac{h_1}{2D_1} P \right] d\delta_t \\ &= \hat{A} \int_0^{\delta_t^*} \left(\frac{\partial \delta_t'}{\partial \delta_t} \frac{\partial \delta_t}{\partial x} + \frac{P h_1}{2D_1} \right) d\delta_t \\ &= \hat{A} \left[\int_0^{\delta_t^*} \delta_t' d\delta_t' + \frac{P h_1}{2D_1} \delta_t^* \right] \\ &= \frac{\hat{A}}{2} \left[\left(\delta_t^{*\prime} \right)^2 + \frac{h_1}{D_1} P \delta_t^* \right] \end{aligned} \,, \tag{4.17}$$

where $\delta_t^{*\prime}$ is the first derivative of the relative shear displacement at the initial crack tip ($x = 0$). Here we assume that both the shear displacement and its first derivative are zero at the clamped end ($x \to -\infty$).

By Eq. (4.11), the first derivative of the shear displacement to the right of the initial crack tip ($0 < x < a$) is

$$\delta_t' = \frac{h_1}{2D_1} P(a - x) \,. \tag{4.18.1}$$

Note that the axial forces are zero in both beams to the right of the crack tip. The first derivative of the shear displacement at the crack tip is then,

$$\delta_t^{*\prime} = \frac{h_1}{2D_1} Pa \,. \tag{4.18.2}$$

Integrating (4.18.1), we obtain the relative shear displacement at the crack tip as

$$\delta_t^* = \delta_t\left(x=a\right) - \frac{Ph_1a^2}{4D_1}. \tag{4.18.3}$$

Since the axial forces are zero for $0 < x < a$, the relative shear displacement at the loading end of the beams is approximately, $\delta_t(x=a) \approx \frac{1}{2}\left(h_1\theta_1 + h_2\theta_2\right)$. Thus we can obtain the shear CTOD at the crack tip as,

$$\delta_t^* = \frac{1}{2}\left(h_1\theta_1 + h_2\theta_2\right) - \frac{a^2}{4}\frac{h_1P}{D_1}, \tag{4.18.4}$$

where θ_1, θ_2 are the end-rotations of the top and bottom adherends, respectively.

We then substitute Eq. (4.18.2) and (4.18.4) into Eq. (4.17) to obtain a simplified expression for J_{II}, namely

$$J_{\mathrm{II}} = \frac{\hat{A}}{4}\frac{h_1}{D_1}P\left(h_2\theta_2 + h_1\theta_1\right). \tag{4.19}$$

Note that the right-hand side of Eq. (4.19) can be fully determined by far-field measurements of P and θ_i. With Eq. (4.18.4), the shear CTOD can also be determined by the far-field measurements. Then, by the definition of J-integral in Eq. (4.12.2), we obtain the shear traction at the initial crack tip as $\tau^* = \frac{dJ_{\mathrm{II}}}{d\delta_t^*}$, which gives the shear traction-separation relation.

Similarly, the fourth derivative of the normal separation can be obtained from Eq. (4.10) along with Eq. (4.7)-(4.9) as

$$\delta_n^{(4)} = -\left(\frac{1}{D_1} + \frac{1}{D_2}\right)\sigma - \left(\frac{h_1}{2D_1} - \frac{h_2}{2D_2}\right)\tau'. \tag{4.20}$$

When the balanced condition in Eq. (4.14) is met, we have a simple relationship between the fourth derivative of the opening displacement and the normal traction as

$$\sigma = -\hat{D}\delta_n^{(4)}, \tag{4.21}$$

where $\hat{D} \equiv \left(\frac{1}{D_1} + \frac{1}{D_2} \right)^{-1}$. Substituting Eq. (4.21) into Eq. (4.12.1), we obtain

$$\begin{aligned} J_I &= -\hat{D}\int \delta_n^{(4)} d\delta_n = -\hat{D}\int \frac{\partial \delta_n^{(3)}}{\partial \delta_n} \frac{\partial \delta_n}{\partial x} d\delta_n \\ &= -\hat{D}\left\{ \left[\delta_n^{(3)} \delta_n' \right]_{x=-\infty}^{x=0} - \int_0^{\delta_n^*} \frac{\partial \delta_n''}{\partial \delta_n'} \frac{\partial \delta_n'}{\partial x} d\delta_n' \right\}, \\ &= \hat{D}\left[\frac{1}{2} \left(\delta_n^{*(2)} \right)^2 - \delta_n^{*(3)} \delta_n^{*\prime} \right] \end{aligned} \tag{4.22}$$

where $\delta_n^{*\prime}$, $\delta_n^{*(2)}$ and $\delta_n^{*(3)}$ are the first, second, and third derivatives of the normal separation at the initial crack tip (i.e., normal CTOD). The normal CTOD and its derivatives are obtained in a similar manner as the shear counterparts. For the beam to the right of the initial crack tip ($0 < x < a$), the governing equation becomes

$$\delta_n^{(2)} = \left(\frac{P_1}{D_1} - \frac{P_2}{D_2} \right)(a - x), \tag{4.23.1}$$

which can be integrated to obtain the normal CTOD

$$\delta_n^* = \Delta_1 - \Delta_2 + \frac{a^3}{6}\left(\frac{P_1}{D_1} - \frac{P_2}{D_2} \right) - a(\theta_1 - \theta_2), \tag{4.23.2}$$

and the derivatives

$$\delta_n^{*\prime} = \theta_1 - \theta_2 - \left(\frac{P_1}{D_1} - \frac{P_2}{D_2} \right)\frac{a^2}{2}. \tag{4.23.3}$$

$$\delta_n^{*(2)} = \left(\frac{P_1}{D_1} - \frac{P_2}{D_2} \right) a, \tag{4.23.4}$$

$$\delta_n^{*(3)} = -\left(\frac{P_1}{D_1} - \frac{P_2}{D_2} \right). \tag{4.23.5}$$

Substituting Eq. (4.23.2-5) into Eq. (4.22), the mode-I component of the J-integral is then

$$J_I = \hat{D}\left(\frac{P_1}{D_1} - \frac{P_2}{D_2} \right)(\theta_1 - \theta_2). \tag{4.24}$$

Therefore, both the mode-I J-integral and the normal CTOD can be determined by far-field measurements of P_i, Δ_i and θ_i. Then, by the definition of J-integral in Eq. (4.12.1), we obtain the normal traction at the initial crack tip as $\sigma^* = \frac{dJ_{\mathrm{I}}}{d\delta_n^*}$, which gives the normal traction-separation relation.

To validate the proposed method, we carried out experiments using the end-loaded split (ELS) and end-notched flexure (ENF) configurations. In the ELS experiments, only the top adherend was loaded, which means that $P_2 = 0$ and $P = P_1$ was measured. In the ENF experiments (see Fig. 36b), we had $\Delta_1 = \Delta_2$, while the total force P was measured. However, the calculation of the mode-I J-integral (Eq. 4.24) requires both end forces (P_1, P_2). While independent measurements of both could be possible by adding a strain measurement on the lower adherend, there was insufficient room to apply a strain gage to the specimen and strain gaging every specimen is costly. On the other hand, it is relatively straightforward to measure the NCOD (δ_n^*) using the IR-COI technique (Gowrishankar et al. 2012). With the measurement of normal CTOD, the force on the top adherend of the ENF specimen can then be obtained from Eq. (4.23.2) as,

$$P_1 = \hat{D}\left\{\frac{P}{D_2} + \frac{6}{a^3}\left[\delta_n^* + (\theta_1 - \theta_2)a\right]\right\}. \tag{4.25.1}$$

Then Eq. (4.24) becomes

$$J_{\mathrm{I}} = \frac{6\hat{D}}{a^2}\left[(\theta_1 - \theta_2)^2 + \frac{\delta_n^*}{a}(\theta_1 - \theta_2)\right]. \tag{4.25.2}$$

4.2 EXPERIMENTAL METHOD

4.2.1 Experiment Configuration

Schematics of the apparatus and the specimen geometry are shown in Figure 36a and 36b, respectively. The loading device is a slightly modified version of the one that was

used in Chapter 2. The bottom clamping condition was changed to an end-clamped condition. A photograph of the experimental setup is shown in Figure 36c. In this experiment, a 45˚ mirror was mounted (Fig. 37a) on the top surface of the top adherend above the loading point. A laser beam was projected onto the surface of the mirror so that the reflection was almost parallel to the axis of the silicon and incident on a position sensing detector (PSD, Thorlabs, PDP90A). Given the initial angle between the incident and reflected beams, and the distance L between the detector and the mirror, the relation between the end-rotation of the silicon beam and the vertical movement (Δd) in the detector is $\theta_1 = \frac{1}{2}\arctan(\Delta d / L)$. The resolution of the end-rotation measurement is then estimated to be at ~10^{-4} radian. To determine the rotation of the lower adherend, a photonic sensor (MTI, KD-245) with a resolution of 100 nm was placed a distance of a_0 ahead of the initial crack tip to measure the deflection Δ_{20} of the lower adherend. Given that the deflection of the lower adherend at the location of the initial crack front was monitored and found to be negligible, the end-rotation of the lower adherend was obtained approximately as $\theta_2 = \Delta_{20} / a_0$. In addition, the end displacement of the bottom adherend was obtained approximately by extrapolation as $\Delta_2 = (a / a_0)\Delta_{20}$. For ENF, the end-rotation of the bottom beam is approximated as $\theta_2 = (\Delta_2 - \Delta_{20}) / (a - a_0)$. The corresponding resolution for the CTODs obtained from Eq. (4.18) and (4.23) was about 100 nm. Error bars in the deduced CTODs were shown to reflect this resolution (Fig. 41).

Classical crack opening interferometry was used to measure the normal crack opening displacement (NCOD) as silicon is transparent to infra-red. This infrared crack opening interferometry (IR-COI) technique essentially uses the interference between the two rays reflected from the crack surfaces to determine the distance between them. The normal infra-red incident beam was provided using an infrared microscope (Olympus BH2-

UMA) that was fitted with an internal beam splitter and an IR filter (1,040 ± 15 nm). The images of the region near the crack front were obtained using a digital camera (Lumenera Corporation, Infinity 3) with a resolution of 1,392 × 1,040 pixels. The images were then processed to determine the NCOD (Gowrishankar et al. 2012). The IR-COI technique implemented in this work has a resolution of 20 nm in the NCOD. It should be noted here that in this experiment, all data were collected and synchronized within single Labview® control program.

4.2.2 Specimen Preparation

The specimen consists of two strips joined by a layer of epoxy. All of the top adherends and some of the bottom adherends were cut from n-type Si (111) wafer supplied by WRS Materials. The wafers were 50 mm in diameter and nominally 1 mm thick. They were polished on both sides to facilitate the use of IR-COI. An automatic dicer (Disco, model DAD 321) was used for cutting wafers into 50 by 5 mm strips for the top adherend and were then cleaned individually by ultra-sonication in de-ionized water to remove any debris accumulated during dicing. To maintain the balanced condition while achieving different mode-mix, the bottom strips were made out of materials with different Young's modulus and thickness. For all specimens, the top adherend was coated with an Au/Pd thin film from one end of the strip to a length of about 19.5 mm. The relatively low adhesion energy between Au/Pd coating and epoxy (~ 0.07 J/m^2) allowed an initial crack to form before fracture of the silicon/epoxy interface. A two component epoxy system (EP30, Masterbond®) was used as the adhesive layer. The epoxy mixture was de-gassed in the vacuum chamber upon mixing. The specimens were cured at room temperature for 72 hours.

Two different lengths of strips were prepared for each of the two experimental configurations (Fig. 4.2b). The length and width of the bottom strips of the ELS were 40×5 mm, respectively and 50×5 mm for the ENF configuration . It should be noted here that, for the ENF specimen, a metal wire (copper alloy) was used between top and bottom adherends in order to reduce the potential effect of friction (Carlsson et al. 1985) between the fracture surfaces of the upper and lower adherends.

4.2.3 Typical Measurements

The experiment was conducted with an applied displacement rate of 1 μm per second. The force versus applied end displacement response for an ELS specimen with silicon as the bottom adherend is shown in Figure 38a. The response was initially linear and started to exhibit slightly nonlinear behavior after an applied displacement of approximately 0.2 mm, as emphasized by the deviation of the dashed straight line. When the force was about to reach the maximum, this nonlinear behavior became more significant. This nonlinear behavior is related to the growth of the cohesive zone. The force decreased after reaching the maximum indicating that the cohesive zone had fully developed and crack propagation had entered steady-state. A linear response was found for the subsequent unloading, which had a lower compliance, thereby confirming that crack extension had occurred during the loading segment.

The corresponding variation in end-displacement (Δ_2) of the bottom adherend is shown in Figure 4.4b. The response was again initially linear followed by a nonlinearly increasing portion as the cohesive zone developed and decreasing during steady state crack growth. The end-rotation of the top adherend increased linearly during the entire loading process (Fig. 38c). The NCOD measurements at the location of the initial crack front were provided as shown in Figure 38d. They increased slowly during the linear portion of the

load-displacement response then increased more rapidly during the development of the cohesive zone and finally increased at a slightly reduced rate during steady state growth. All these measurements indicated that the interfacial crack experienced three stages: Crack face opening without growth, cohesive zone growth and steady-state crack growth.

The NCOD measurements for an ENF experiment are provided in Figure 39b. This shear dominated interfacial fracture growth experienced the same three stages. However, the softer load-displacement response associated with cohesive zone development was more difficult to discern. Although this is a shear dominant experiment, there is some normal opening (Fig. 39b) with a more marked transition to cohesive zone development.

4.3 ANALYSIS AND MODELING

4.3.1 Mode-mix

The analytical method recognizes the ELS specimens as double-layer structure where the complex stress intensity factor K is written as (Suo and Hutchinson 1989)

$$K = h_1^{-i\varepsilon}\left(\frac{1-\alpha}{1-\beta^2}\right)^{1/2}\left(ie^{i\gamma}\frac{1-C_3}{\sqrt{2h^3V}}-\frac{C_2}{\sqrt{2h^3U}}\right)e^{i\omega}P_1 a\,, \tag{4.26}$$

where C_2, C_3, U, V, and γ are the geometric factors given by $C_2=\Sigma\left(\eta+\frac{1}{2}-\Delta\right)$, $C_3=\Sigma/(12I)$, $U=\left[1+\Sigma\eta\left(4+6\eta+3\eta^2\right)\right]^{-1}$, $V=\left[12\left(1+\Sigma\eta^3\right)\right]^{-1}$, $\gamma=\arcsin\left[6\sum\eta^2(1+\eta)\sqrt{UV}\right]$, and $\Sigma=(1+\alpha)/(1-\alpha)$, with $\alpha=\left(\bar{E}_1-\bar{E}_2\right)/\left(\bar{E}_1+\bar{E}_2\right)$ and $\bar{E}_i=E_i/\left(1-\nu_i^2\right)$. The cross section parameters are $\eta=h_1/h_2$, $\Delta=\left(1+2\Sigma\eta+\Sigma\eta^2\right)/\left[2\eta\left(1+\Sigma\eta\right)\right]$, and the angle ω is a function of elastic mismatch parameters α, β and η. The moment of inertia of the composite section is

$$I=\Sigma\left[\left(\Delta-\eta^{-1}\right)^2-\left(\Delta-\eta^{-1}\right)+1/3\right]+(\Delta/\eta)\left(\Delta-\eta^{-1}\right)+(1/3)\eta^{-3}\,.$$

The obtained stress intensity factor was then substituted into Eq. (2.6) to obtain the corresponding phase angle. The epoxy thickness of 50 μm was used as the length scale as

required in Eq. (2.6). The analytical mode-mix results were compared with those obtained using finite element model without considering epoxy layer and were found (Fig. 40) to be in agreement.

The mode-mix results indicate (Fig. 40) that the epoxy layer causes a significant shift in phase angle for ELS specimens especially for substrates with high Young's modulus. However, it did not have a similar effect on the ENF specimens. In a sense, this effect was limited in the shear dominant regime. By combining ELS and ENF specimens, the mode-mix provided in this experiment spanned angles from -50 to 90º. The epoxy thickness was well controlled with an average deviation of ±5 μm which resulted in a deviation in phase angle of approximately ±1.5˚. Table 6 shows detailed information about the specimens and corresponding values of mode-mix angles. From the table, it can be observed that the thickness of the bottom adherend increased as the Young's modulus decreased. For the case of an acrylic bottom adherend, the required thickness, which is the largest of all bottom adherends, is slightly more than 1/10 of the adherend's length, reaching the upper limit when Euler-beam theory still applies. On the other end, when Young's modulus exceeded 210 GPa (stainless steel), the manufacturing process became quite challenging to make adherends with a thickness below 1 mm. Therefore, the ENF configuration was selected to extend the mode-mix to the higher end of shear dominance.

4.3.2 CTOD, J-integral, and TSRs

The normal and shear CTODs were obtained using Eq. (4.23.2) and (4.18.4), respectively and are plotted (Fig. 43) versus applied displacement. The error bars were obtained through uncertainty analysis based on the resolutions of the position sensing device and photonic sensor. The NCOD measured using IR-COI are also plotted for comparison/validation purposes. From the comparison, it is observed that NCODs

determined from global parameters and beam theory had similar responses to those measured by IR-COI. Close agreement was observed from both the linear stage, the concurrent turning point ($\Delta_1 = 0.2\,\text{mm}$), and the non-linear stage. Especially in the linear stage, most of the IR-COI data fell within the error bar range of the deduced NCOD results. This close agreement demonstrated the validity of the proposed method for obtaining CTODs from far-field data. The NCOD reached 2.5 μm as the force reached its peak. The corresponding shear CTOD was at the same level and even higher in the linear stage. However, at the peak force , the shear CTOD were much lower than the NCOD. This indicated a non-proportional displacement loading path which suggests that the damage processes for normal and shear might have initiated at different points in time.

The calculated J-integrals in both opening and sliding modes are plotted against CTODs in Figure 42. Early on, the increments in CTODs were small (Fig. 41) as the end-displacement increased. The corresponding J-integral also increases slowly to an elastic limit of the interfacial behavior (~1 J/m^2). However, as the cohesive zone started to grow, the CTODs increased rapidly causing significant increases in both components of the J-integral until J_I and J_{II} reached their steady-state limits. It is interesting to note that in Eq. (4.17) and Eq. (4.22), the J-integrals were nonlinear functions of CTODs and derivatives of CTODs. This fact is demonstrated in this figure. It is also interesting to observe that J_{II} is greater than J_I by almost 30% which was not seen in Chapter 2. It also should be noted here that the error in calculating J-integral is small that, the error bar on J-integral values is smaller than the symbol shown in the figure.

Upon taking the numerical derivatives of the J-integrals with respect to their respective CTODs, the resulting TSRs in both directions are obtained in Figure 43. In the normal TSR, an initially stiffening response was observed. In the past, the response prior to the maximum traction has been universally represented by linearly elastic behavior.

Time constraints have not allowed further investigation to determine if the stiffening behavior is elastic. A stiffening response is certainly consistent with rubber-like behavior and may relate to randomly oriented polymer chains in the epoxy interphase being oriented normal to the interface as the loading is increased. The normal traction reached its peak at a normal separation of approximately 130 nm which was very close to the values found in previous works (Gowrishankar et al. 2014) and in Chapter 2, albeit with a different epoxy. The peak strength was about 48 MPa which was at the elastic limit of the epoxy (Na 2015) used in present study. After the peak, the normal traction dropped suddenly and eased into a plateau with an average strength of 2 MPa, which ended at a normal separation of 2.5 μm. The descending traction followed a power-law type function of separation, with a steeper decay than has been previously described by exponential functions. The shear TSR had an essentially linear response till the shear traction reached its peak. After the peak, the traction dropped very rapidly to zero with a very small increase in separation for a shear interaction range of 0.7 μm, much smaller than the range of the normal interaction.

Considering the dissimilarities in the behavior of the normal and shear TSRs, the development of the separations and tractions was considered in more detail (Fig. 44). The crack-tip normal and shear separations are compared in Figure 44a where a short linear segment terminates at point ① ($\Delta_1 = 0.085$ mm). After that δ_n^* increases more slowly than δ_t^*. This stage ends at point ② ($\Delta_1 = 0.2$ mm), followed by a faster growth in δ_n^* as δ_t^* did not change much. After point ③ ($\Delta_1 = 0.38$ mm), both CTODs grow rapidly without any specific pattern. The corresponding critical applied displacement points were labeled in a plot of the two tractions versus applied end-displacement (Fig. 44b). Between zero and point ①, the response is linear for both tractions near the original crack front. After point ①, the normal traction increases much more rapidly than the linearly increasing shear traction. After point ②, the normal traction decreases sharply while the shear traction

maintains its constant growth rate. However, after point ③, the shear traction rapidly decayed to zero simultaneously with the normal traction. The implication of this sequence of events is that damage processes in the normal and shear responses are not coupled as commonly assumed. In other words, the mixed fracture process cannot be described by using a single damage parameter for both the normal and shear interactions.

4.3.3 Decoupled Cohesive Zone Modeling

Weak-formulation

To describe the cohesive zone growth observed from the extracted TSRs, a user-defined finite element subroutine (UEL) was programmed within the ABAQUS® (v6.12) finite element package. In this subroutine, a cohesive element based on a weak formulation of the interfacial behavior was implemented, following the approach by Rahul-Kumar et al. (1999), Song et al. (2008), and Alfano et al. (2008). The development of the cohesive elements embedded in this implicit finite element framework requires the virtual work by the cohesive tractions along an interface. This virtual work is

$$\delta W_{coh} = \int_{S_0} \{\delta\Delta\}\{T\}\, dS_0 , \tag{4.27}$$

where S_0 is the interface in the undeformed configuration, $\{\Delta\}$ is the virtual jump displacement across the cohesive element faces and $\{T\}$ is the traction along the interface. The virtual work in the undeformed configuration in terms of nodal displacement $\{u\}$ can be written as,

$$\delta W_{coh} = \{\delta u\}^T \int_{S_0} [N]^T \{T\}\, dS_0 , \tag{4.28}$$

where $[N]$ is the nodal shape function matrix, which corresponds to nodal displacement jumps. The first variation of the virtual work is written as

$$d\left(\delta W_{coh}\right) = \{\delta u\}^T \int_{S_0} [N]^T d\{T\}\, dS_0 . \tag{4.29}$$

The incremental tractions with the corresponding incremental displacement jumps are related through the cohesive Jacobian matrix,

$$d\{T\} = \{C\}\, d\{\Delta\}. \tag{4.30}$$

Therefore, the variation of virtual work can be approximately obtained as,

$$d(\delta W_{coh}) = \{\delta u\}^T \left\{ \int_{S_0} [N]^T [C][N] dS_0 \right\} du \tag{4.31}$$

The integral in the middle forms the cohesive element stiffness matrix used for Newton-Raphson iterations in implicit solution scheme.

In a two-dimensional setting, this Jacobian matrix is then,

$$[C] = \begin{bmatrix} \partial\sigma/\partial\delta_n & \partial\sigma/\partial\delta_t \\ \partial\tau/\partial\delta_n & \partial\tau/\partial\delta_t \end{bmatrix}. \tag{4.32}$$

As observed from the extracted TSRs, the normal traction was found to be independent of shear CTOD and vice versa. Therefore, we set the off-diagonal elements in this Jacobian matrix to zero in order to implement the aforementioned decoupling.

Implementation and results

To import the extracted TSRs into the UEL, we formulated a tabulated input approach. Given a set of separations ($\{\Delta\} = (\delta_n,\ \delta_t)^T$) and the tabulated TSR input, the corresponding Jacobian matrix is

$$[C]\big|_{\{\Delta\}\in(\{\Delta_A\},\{\Delta_B\})} = \begin{bmatrix} (\sigma_B - \sigma_A)/(\delta_{nB} - \delta_{nA}) & 0 \\ 0 & (\tau_B - \tau_A)/(\delta_{tB} - \delta_{tA}) \end{bmatrix}, \tag{4.33}$$

where $\sigma_{A,B}$, $\delta_{A,B}$ were the values in the tabulated TSR input. It should be noted here that for the negative part of normal separation, we use the equivalent modulus from the epoxy layer to obtain the elements of Jacobian matrix ($\left.\frac{\partial\sigma}{\partial\delta_n}\right|_{\delta_n<0} = \frac{E_e}{h_e}$).

The stress contours at the peak force for the ELS specimen with silicon as the bottom adherend are shown in Figure 45. At this moment, the cohesive zone has almost fully developed when the shear traction reached the peak, and the interface crack was about to enter steady-state. We found that the maximum normal stress was not at the same location of the maximum shear stress. This difference resulted from the decoupling of normal and shear damage processes in the extracted TSRs. We then plotted the traction and separation distribution along the interface (Fig. 46). We confirmed that the peak normal traction was ahead of the initial crack tip by 650 μm. The peak shear traction was still at the location of the initial crack tip. This separation of peak tractions brought about issues in defining crack tips using conventional concepts. It also further confirmed that potential-based TSRs could not be used to describe the interfacial behavior in the present study.

We also compared the numerical results to the experimental measurements as a consistency check (Fig. 38a-c). Close agreement was found with these global measurements (i.e., force response, end-rotation, and end-displacement). We also compared the CTODs obtained from the cohesive zone modeling to those from the proposed deduction scheme (Eq. 4.18 and 4.23) shown in Figure 4.13. Slight differences were found after NCOD exceeded the initiation separation which corresponded to the peak traction. This might be due to the Euler beam assumption. The reduced deformation caused by shear contributed to the reduction of CTODs from the deduced scheme. From the favorable comparison of both far-field and local measurements (Fig. 47), the proposed deduction scheme was considered to be validated.

4.4 TSRs, Toughness, and Mode-mix

4.4.1 Normal TSRs

The normal TSRs extracted for mode-mix angles between $-50° < \psi < 50°$ (i.e., lower mode-mix) are plotted in Figure 48a, and those between $50° < \psi < 90°$ (i.e., higher mode-mix) are plotted in Figure 48b. The peak tractions varied (Fig. 49a) between 38.92 MPa and 47.35 MPa. The separation at the onset of damage (δ_{n0}), which corresponds to the peak traction, varied between 108 nm to 132 nm (Fig. 49b). The critical separation (δ_{nc}) varied between 2.1 μm and 2.7 μm. The strength of the normal TSRs extracted for higher mode-mix angles dropped with increasing mode-mix (44.84 MPa, 42.85 MPa, and 38.92 MPa). The distribution of strengths with mode-mix is summarized in Figure 4.15a and indicates that the maximum strength occurred at a mode-mix angle of about 50°. The critical separations also dropped (Fig. 50) for mode-mix angles greater than 50°. It is near this mode-mix that shear begins to dominate to such an extent that full slip has occurred before the normal tractions can fully develop.

In preparation for generalizing the normal TSRs as a function of mode-mix, each extracted TSR was fit to power laws of the form

$$\sigma = \begin{cases} \sigma_0 \left(\dfrac{\delta_n}{\delta_{n0}} \right)^{\alpha}, & 0 < \delta_n < \delta_{n0} \\ \sigma_0 \left(\dfrac{\delta_n}{\delta_{n0}} \right)^{\beta_n}, & \delta_{n0} < \delta_n < \delta_{nc} \end{cases}, \tag{4.34}$$

where σ_0 is the normal strength, α and β_n are the power law exponents for the ascending and descending portions of the TSR. The determination of δ_{nc}, however, relied on the mode-I toughness (shown in Fig. 50). The toughness values can then be obtained by taken the integral of Eq. (4.34) with respect to the normal opening (δ_n). Thus,

$$\Gamma_I = \sigma_0 \left[\frac{\delta_{n0}}{1+\alpha} + \frac{\delta_{nc}}{\beta_n - 1} \left(\frac{\delta_{n0}}{\delta_{nc}} \right)^{\beta_n} \right]. \quad (4.35)$$

The implication of Eq. (4.35) is that δ_{nc} can be determined numerically if the opening at damage initiation (δ_{n0}), the power law indices (α, β_n), and mode-I toughness value (Γ_I).

The fitting parameters for the normal TSRs are plotted as a function of the mode-mix angle (Fig. 51) and actual values are given in Table 7. They were all essentially independent of mode-mix. This observation suggested that the normal strength σ_0 and the power law exponents α and β_n could be averaged over all mode-mix angles and used, along with the variation of the mode-I component of toughness, to determine the critical separation δ_{nc} from Eq. (4.35). Following this idea, the normal strength was set at 42.63 MPa, δ_{n0} was 120 nm, α was 4.5, and β_n was -1.35.

As check on how well the procedure works, the fitted and extracted normal TSRs at a mode-mix of 26.97° (ELS specimen with silicon adherends) compare quite well (Fig. 51a). Close agreement was found in the ascending part, but slight differences were found for the descending part. This may be due to the fitting process. The results for a mode-mix of 61.07° (ENF specimen with the aluminum as the bottom adherend) are shown in Figure 51b. The fitted TSR was in reasonable agreement over the entire range of normal opening.

4.4.2 Shear TSRs

The shear TSRs for all mode-mix are presented in Figure 52. In all cases, the ascending part is linear, albeit with slightly different slopes. The shear strength τ_0 increased as the mode-mix increased. The peaks are followed by much sharper decays than were observed for the normal TSRs, emphasizing that damage evolution is different under tension and shear. This is in contrast to most current representations of mixed-mode TSRs, where damage evolution is assumed to be the same for tensile and shear interactions. The

initial separation (δ_{t0}) corresponding to the shear strength and the critical separation (δ_{tc}) both increase with increasing mode-mix.

The parameters of the extracted shear TSRs are listed in Table 8 as a function of mode-mix. There was no consistent trend with mode-mix and the variation appeared to be small. In fact, the average value of the initial stiffness is 56 MPa/μm, with a coefficient of variation of 8%. Consequently, the mean value was used as the initial stiffness of the all the shear TSRs (k_t). The shear strengths were then recomputed from the measured initial separations through $\tau_0 = k_t \delta_{t0}$. The difference between the recomputed and original values was less than 8%. It was also interesting to note that the ratio $f_t \equiv \delta_{t0} / \delta_{tc}$ between the initial shear separations (δ_{t0}) and critical separations (δ_{tc}) had an average of 0.75 with a coefficient of variation of 5%. Therefore, it is convenient and reasonable to take this value as a constant. The descending part of each shear traction-separation relation was also fit to a power law. Thus, the following fit was suggested for each shear TSR.

$$\tau = \begin{cases} k_t \delta_t, & 0 < \delta_t < \delta_{t0}, \\ k_t \delta_{t0} \left(\dfrac{\delta_t}{\delta_{t0}} \right)^{\beta_t}, & \delta_{t0} < \delta_t < \delta_{tc} \end{cases}, \tag{4.36}$$

where, β_t is the power law exponent for the descending part. The average value over all mode-mix values was -9, with a coefficient of variation of 5%. From the average values of k_t, f_t, β_t, the mode-II toughness can then be obtained

$$\Gamma_{II} = k_t \delta_{t0}^2 \left[\frac{1}{2} + \frac{(f_t)^{\beta_t - 1}}{\beta_t - 1} \right]. \tag{4.37}$$

This allows the initial separation (δ_{t0}) to be extracted as a function of mode-mix from the already measured values of Γ_{II}. The values are included in Table 8. In order to avoid confusion from plotting all the results, the TSRs obtained in the manner just described are compared with the corresponding initial estimates at the mode-mix values of -53 and 87°

in Figure 53. In each case, there is close agreement in both the ascending and descending portions of the TSRs, thereby generalizing Eq. 4.36 for the shear component of the TSRs for the silicon/epoxy interface to all values of mode-mix between -50 and 90°.

4.4.3 Mixed-mode Toughness

As just described, both the normal and shear TSRs can be interpolated between -50 and 90° on the basis of the toughness as a function of mode-mix. For convenience, the variation of toughness with mode-mix was fit to a 4th order polynomial

$$\Gamma_i = a_i\psi^4 + b_i\psi^3 + c_i\psi^2 + d_i\psi + e_i, \tag{4.38}$$

where a_i, b_i, c_i, d_i, e_i for $i = T, I, II$ are the coefficients of the polynomial Table 9. The coefficients for the mode-I toughness were obtained by subtracting the mode-II toughness from the total toughness.

The total toughness versus both global and local phase angles is shown in Figure 54. The total toughness and the mode-II toughness (Fig. 55) both increased with increasing phase angle and exhibited the same asymmetric behavior with respect to mode-mix that has been noted for the total toughness of glass/epoxy and sapphire/epoxy interfaces (Chai and Liechti 1992, Liang and Liechti 1995, Swadener and Liechti 1998, Mello and Liechti 2006). The mode-I toughness was essentially constant for negative mode-mix angles (Fig. 56) and then dropped sharply for angles above 50°. Therefore, for a given mode-mix, the toughness of both fracture modes is known and can be used to determine both TSRs using the aforementioned procedures. As a result, the TSRs for this silicon/epoxy interface can be obtained for phase angles ranging from -50° to 90º, thereby covering almost 80% of the whole spectrum of phase angles.

4.5 DISCUSSION

The efficacy of using balanced laminates, with the attendant decoupling of the normal and shear tractions in the differential equations for the normal and shear separations and mode I and II components of the J-integral, has been demonstrated over a wide range of mode-mix angles. An additional benefit is that the crack tip opening displacements can be obtained from global parameters including load and load point displacement and rotation for each adherend and an Euler beam theory analysis. These global parameters can be thought of as amplified signals of the local deformations at the crack tip. The resolution in crack tip opening displacements is about 100 nm, which is not as good as the 20 nm associated with infra-red crack opening interferometry. However, an advantage of using the global measurements is that both normal and shear crack tip opening displacements can be measured.

When the balanced condition is not satisfied, there are coupling terms in both differential equations and part of the opening mode J-integral contains the work done by the shear tractions, and vice versa. Moreover, more information (such as displacement profile and rotation profile along the boundaries, etc.) is needed to determine each component of the J-integral.

The decoupled extraction of normal and shear components of traction-separation relations over a wide range of mode-mix angles and without any apriori assumptions as to form, damage evolution, etc. allows for a critical examination of cohesive zone modeling approaches. In potential-based cohesive zone modeling, it is required that $T(\Delta) = \partial\phi(\Delta)/\partial\Delta$, where ϕ represents the work done when an interface undergoes a relative separation (Δ). This further requires that the J-integral should be independent of loading-path, which was not the case in the present study. Perhaps the most striking observation regarding the extracted traction-separation relations is that damage initiation

and evolution was different in the two components of the traction-separation relations. This is counter to the common assumption that evolution of damage is the same in the normal and shear components of the traction-separation relations. This led to the presence of two crack fronts; one for opening and the other for slip separation. Another consequence is that there was some residual shear strength after the normal traction had nearly vanished.

The path that the crack tip displacements followed (δ_t^* versus δ_n^*) as the applied displacement was increased at a constant rate is shown in Figure 4.23. In all cases, the response was not proportional and the shear CTOD initially increased much more quickly than the normal component. At higher load levels and lower mode-mix angles $\left(< 49^\circ\right)$, the steep rise in shear displacements transitioned to a plateau-like response where the normal components increased while the shear remained constant. Such a transition did not develop for angles greater than 49°, where the shear CTOD was dominant. For angles of 40, 29 and 10°, the plateau was followed by a faster increase in shear displacement. It did not appear to be possible to convert these observations into a unifying condition. However, the normalized toughness values (Fig. 57) followed the familiar interaction form $\left(\frac{J_I}{\Gamma_I}\right)^\lambda + \left(\frac{J_{II}}{\Gamma_{II}}\right)^\lambda = 1$, where $\lambda = 1.3$, provided the best fit.

The extracted TSRs using the beam analysis include the behavior of epoxy layer, leaving open the question as to how much of the extracted total separation is due to the separation of the two interfaces and how much is due to the bulk epoxy. In doing so, it is recognized that it is likely that a thin interphase layer forms in the epoxy next to the silicon. This interphase is expected (Sharpe 1972) and has been shown to have mechanical and fracture behavior that differs (Rakestraw et al. 1995) from those of the bulk epoxy. The contribution of the bulk behavior of the epoxy to the total separation was assumed to be elastic. The maximum normal traction was similar to the yield strength of the epoxy (Na

2015), so any yielding is expected to be small given the sharp decay in traction (Fig. 51). The contribution was determined by first conducting a finite element analysis of two silicon strips with the corresponding extracted traction-separation relation active between them. This analysis established the extent of the cohesive zone and the tractions acting over it. This distribution of tractions was then applied to a strip of epoxy having the thickness of the epoxy in the experiment. The bottom of the epoxy strip was fixed in both directions.

The applied traction profiles are shown in Figure 59a. The normal and shear deformations (δ_{ne}, δ_{te}) along the top surface of the epoxy layer are shown in Figure 59b. The division between the elastic and damaging part of the cohesive zone can best be identified from the normal deformation at about 850 μm from the traction-free crack tip. The shear deformation followed the trend observed in the numerical results (Fig. 46). The interfacial separations were obtained by subtracting the epoxy deformations from the separations that were obtained from the same analysis that had established the distribution of tractions in the absence of the epoxy. The resulting traction-separation relations for the silicon/epoxy interface at a mode-mix of 40.57° are shown in Figure 60a. After removing the elastic response of the epoxy layer in the cohesive zone, the ascending part of the normal TSR has a much higher stiffness. The initial normal separation (δ_{n0}) was reduced to 60 nm, which was about half of the original value. The effect of the epoxy layer on the descending portion of the traction-separation relation is less noticeable with most of the drop in the interaction range from 2.6 to 1.6 μm coming from the elastic part of the traction-separation relation. In the shear direction, the linear ascending part became slightly nonlinear as the traction reached its peak value. The shear interaction range dropped to 0.74 from 0.78 μm, indicating that the shear deformation in the epoxy at this mode-mix was relatively minor. Similar behavior was found for $\psi = -53.07°$ and $\psi = 87.46°$ (Figure 60b-c).

CHAPTER 5: CONCLUSIONS AND FUTURE WORK

The work in Chapter 2 builds on a previous characterization (Gowrishankar et al. 2012) of the traction-separation relations of an silicon/epoxy interface that was separated under nominally mode-I conditions (Gowrishankar et al. 2012). In the present work, mixed-mode conditions were provided by an end-loaded-split (ELS) configuration, where the epoxy was sandwiched between two silicon strips. The nominal mode-mix provided by the ELS configuration was extended by varying the thickness of the epoxy layer. A series of experiments were conducted under displacement control. The normal crack opening displacements in the interior of the specimen were measured by infra-red crack opening interferometry. In some experiments, digital image correlation was used to measure the crack-tip displacements in both the normal and tangential directions on one of the edges of the specimen, in the region intersected by the crack front. Finite element models of the configuration were developed that accounted for the elastic behavior of the silicon and epoxy and the interactions between them using a damage-based cohesive zone model. The key parameters for the traction-separation relations were extracted from the measured resistance curves and normal crack opening displacements and finite element solutions for a range of values of the softening parameter in the traction-separation relation.

For the range of mode-mixes considered here (-41° to 0°), it was noted that, although the steady state toughness was a function of the mode-mix, the elastic behavior, normal and shear strengths and the softening parameter were not. The mixed-mode traction-separation relations from this model were validated by comparing to the ELS experiments using epoxy thickness values and associated phase angles that were not used for parameter extraction in its development. The load-displacement, and normal crack tip opening displacements vs. applied displacement responses and resistance curves were all

captured very well. Interestingly, resistance curves based on J-integral calculations that also accounted for the damaging portion of the traction-separation relations had a different shape than those that were only based on the elastic foundation analyses. This is to be expected but, the measurement-based parameter extraction was, and can only be, founded on the latter.

Chapter 3 described a via pushout experiment to extract the interfacial properties for shear interactions between a copper TSV and silicon. A shear lag analysis was used to develop initial estimates of the interfacial traction-separation relation including the frictional shear strength of the interface. This was followed by detailed finite element analyses with cohesive zone modeling of the pushout experiment that accounted for the plasticity in the copper via and the shear interactions between copper and silicon. The average critical shear traction required to initiate interfacial sliding was found to be 77.2 MPa and the corresponding relative displacement across the interface was 182.7 nm, while the frictional shear strength was 25 MPa. The traction-separation relation with the extracted parameters may be used to study via extrusion and associated reliability analysis for integrated TSV.

In Chapter 4, an analytical and experimental program was developed to directly and simultaneously extract TSRs over a wide range of mode-mix using only far-field measurements without making any apriori assumptions on the form of the TSRs. A so-called balanced condition was used to decouple the shear and normal tractions along the interface resulting an explicit expression for the J-integral in both opening and sliding modes. The normal and shear CTODs were determined using measurements of load and load-line displacement and rotation of each adherend (global parameters) through Euler-beam theory. The TSRs were obtained from numerical differentiation conducted on each component of the J-integral with respect to the corresponding CTODs. NCOD

measurements from IR-COI validated the normal crack opening displacements determined from the measurement of global parameters. By varying the modulus and thickness of the bottom adherend, mode-mix angles ranging from -50˚ to 90˚ were obtained for the interfacial fracture of a silicon/epoxy interface using both ELS and ENF specimens. An interpolation method was also suggested based on knowing the toughness as a function of phase angle and the invariance of the strength and shape of the normal traction-separation relations with mode-mix. The shape was based on power laws for the ascending and descending portions of the normal and shear traction-separation relations. Cohesive zone modeling using the decoupled TSRs was conducted as well. The numerical results were compared with experimental ones, serving as a further validation of the proposed scheme since the shear CTOD could not be measured using IR-COI.

In its current form, for examples such as wafer bonding and interactions between functionalized surfaces, this approach directly yields the interactions between the adherends. When the adherends are joined by an interlayer, the deformations of the layer as well as the interfacial interactions between the layer and the adherends are both included in the extracted separations. A promising attempt was made to subtract out the elastic deformations of the epoxy that was used in this work. This was achieved by conducting a cohesive zone analysis using an extracted pair of normal and shear traction-separation relations for a particular mode-mix without the epoxy between the adherends. This established the distribution of the tractions over the cohesive zone. These became the boundary conditions for a second analysis of a strip of the epoxy with the same thickness that was used in the experiment being analyzed. The deformations of the epoxy were then subtracted from the separations determined from the balanced beam analysis to reveal the deformations and traction-separation relations of the silicon epoxy interface.

The approach that has been developed here for simultaneously extracting the normal and shear components of the mixed-mode interactions of an interface over a wide range of mode-mix is relatively simple to implement. It has the potential to be applied to a wide range of interfacial problems without any assumptions as to the form of the interactions. These can range from those encountered in structural adhesive bonding to molecular interactions between 2D materials as long as they are amenable to being examined in laminated beam geometries.

In the future, the developed balanced beam approach can be applied to other interfaces such as glass/epoxy, copper/graphene, silicon/silicon, etc. Environmental effects such as moisture and temperature can also be studied using the developed experimental platform. Rate effects can also be addressed, but all such effects will potentially require some modification. The main one has to do with the deformation of any interlayer, particularly if any inelastic and nonlinear behavior of the bulk interlayer material is involved. While these have not been addressed here, a promising framework has been established for doing so.

In this dissertation, two types of asymmetric specimens (ELS and ENF) were used to extend the range of mode-mix. However, it would be more rigorous to use one type of specimen with the same adherends while still covering a wide range of mode-mix. The requirement of similar adherends addresses the fact that, when an interlayer is involved, there are two interfaces. If they are both the same, then the extracted separations can simply be divided by two. This can be achieved by making use of the symmetric DCB configuration with each beam loaded by two independent actuators (Singh et al. 2010). With this setup, we would also obtain more accurate end-rotation measurements with additional displacement measurements at the end of the bottom adherend.

FIGURES

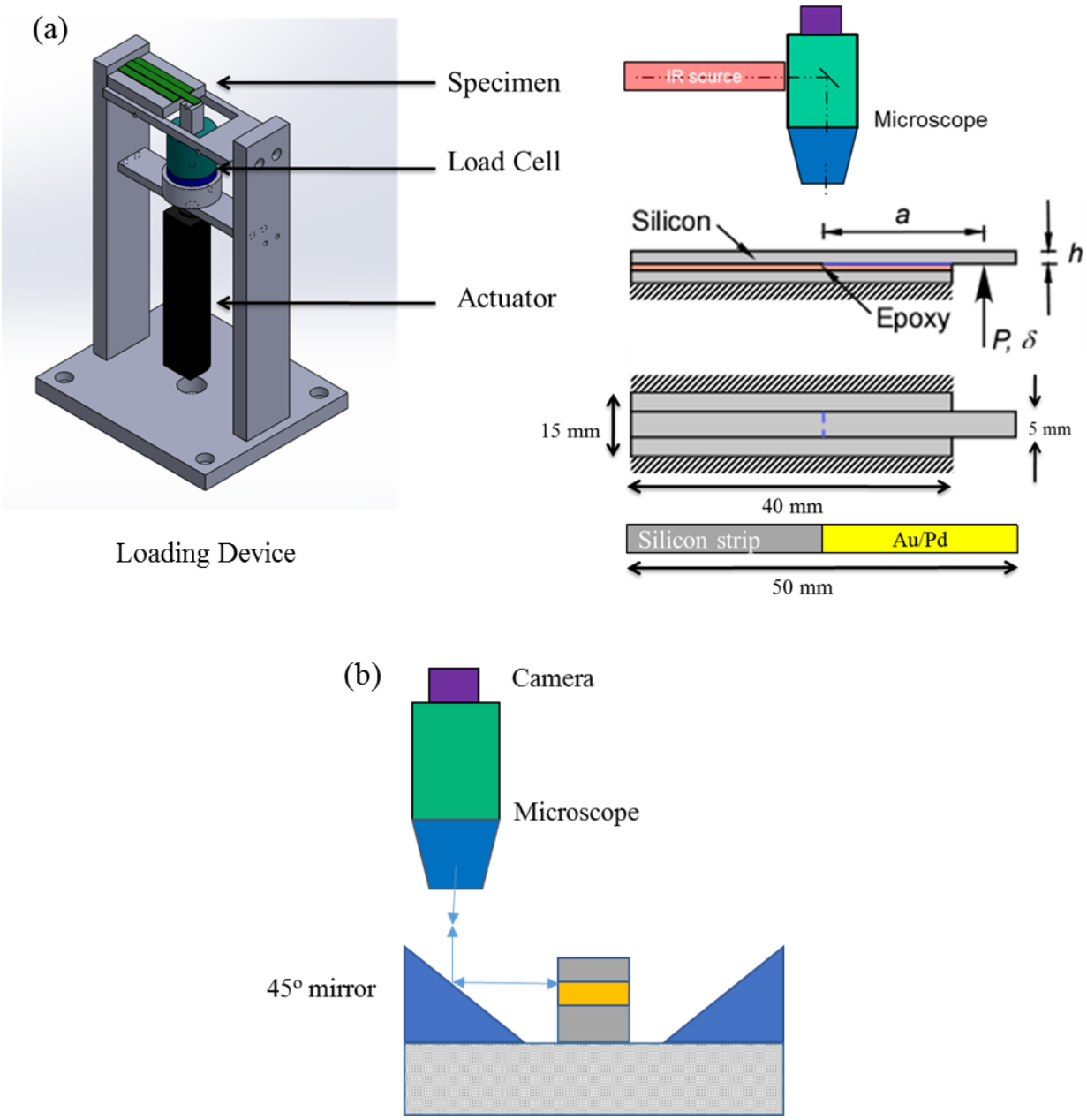

Figure 1: (a) Schematics of the loading device and specimen for the end loaded split (ELS) experiments, with IR-COI measurement, (b) setup for DIC. measurements.

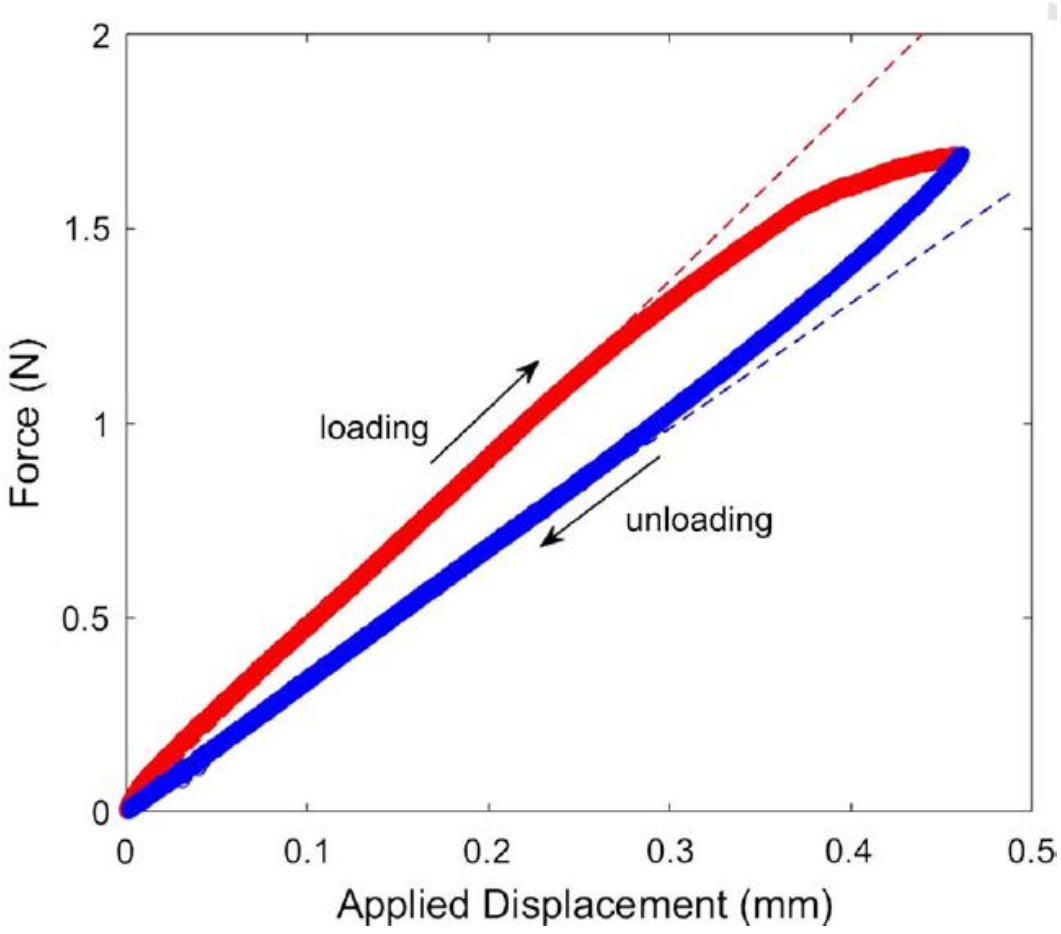

Figure 2: Load versus displacement response for an ELS specimen with epoxy thickness of 8 μm. The initial and final crack lengths are determined by comparing the linear parts of the loading and unloading responses with the beam-on-elastic foundation (BEF) model.

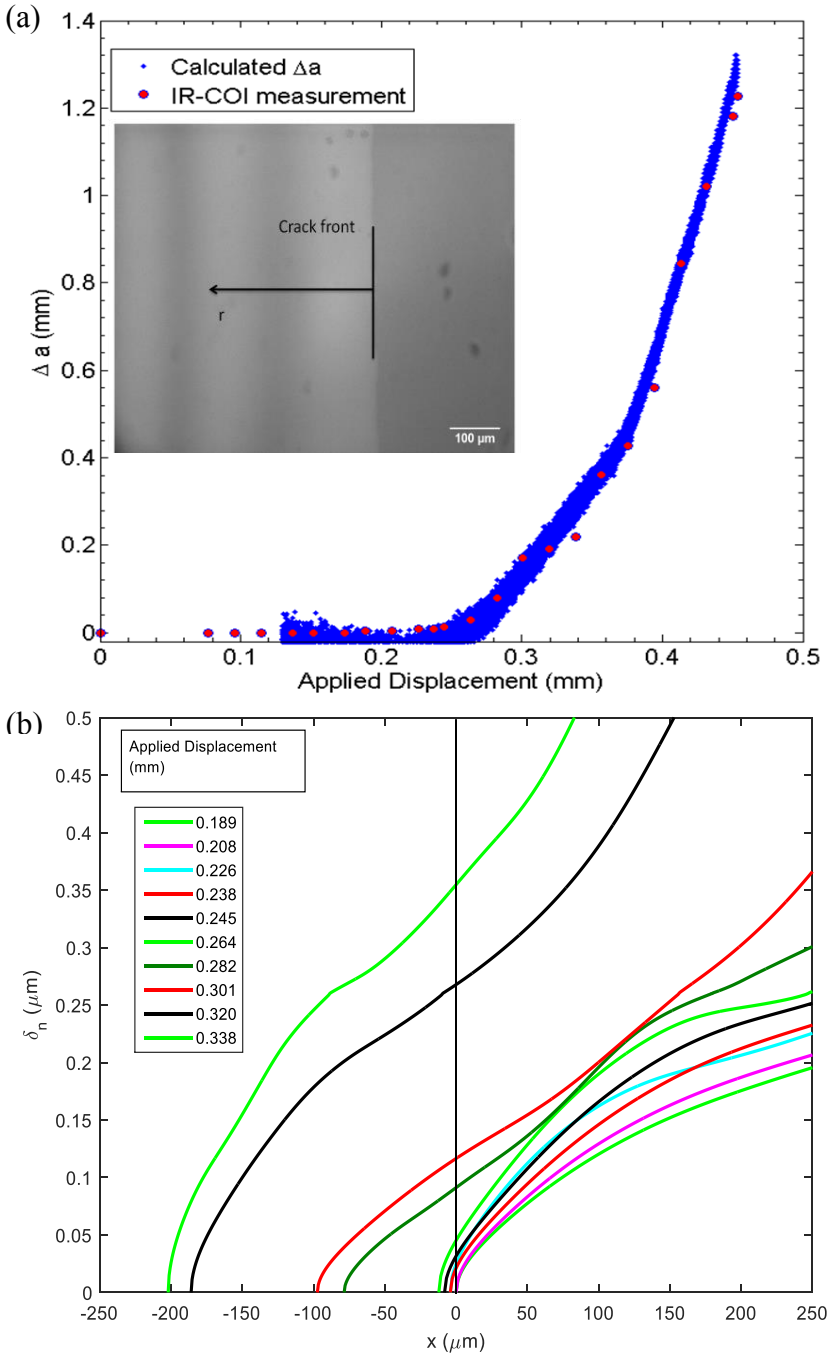

Figure 3: Crack growth versus the applied displacement for the ELS specimen with epoxy thickness of 8 μm: (a) crack length by IR-COI measurements and BEF calculation using the measured load-displacement responses in Fig. 2.2, (b) Measured NCOD profiles at increasing applied displacement.

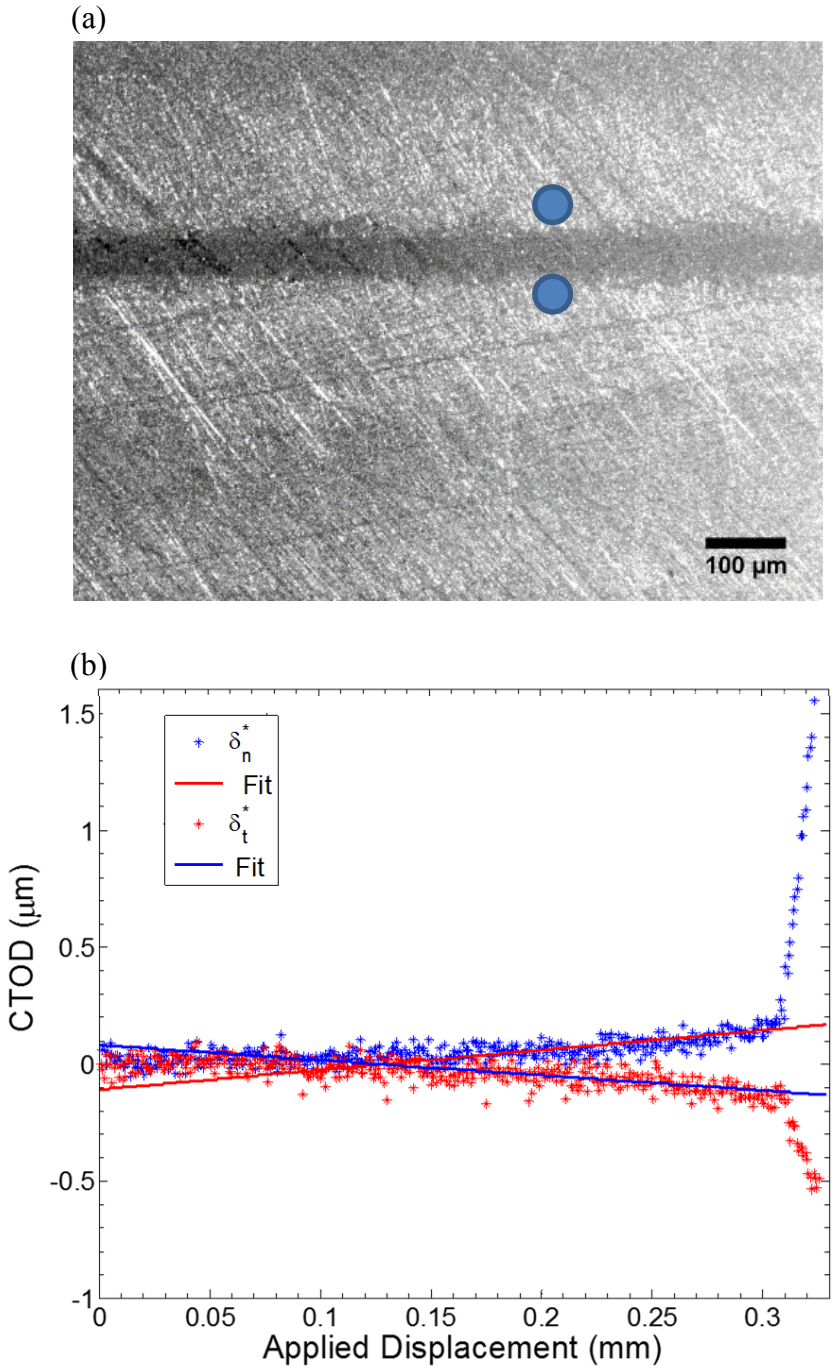

Figure 4: (a) Surface texture of an ELS specimen (50 μm epoxy thickness) for DIC measurement, with two reference points identified at the upper and lower sides of the initial crack front, (b) measured normal and tangential CTODs by DIC.

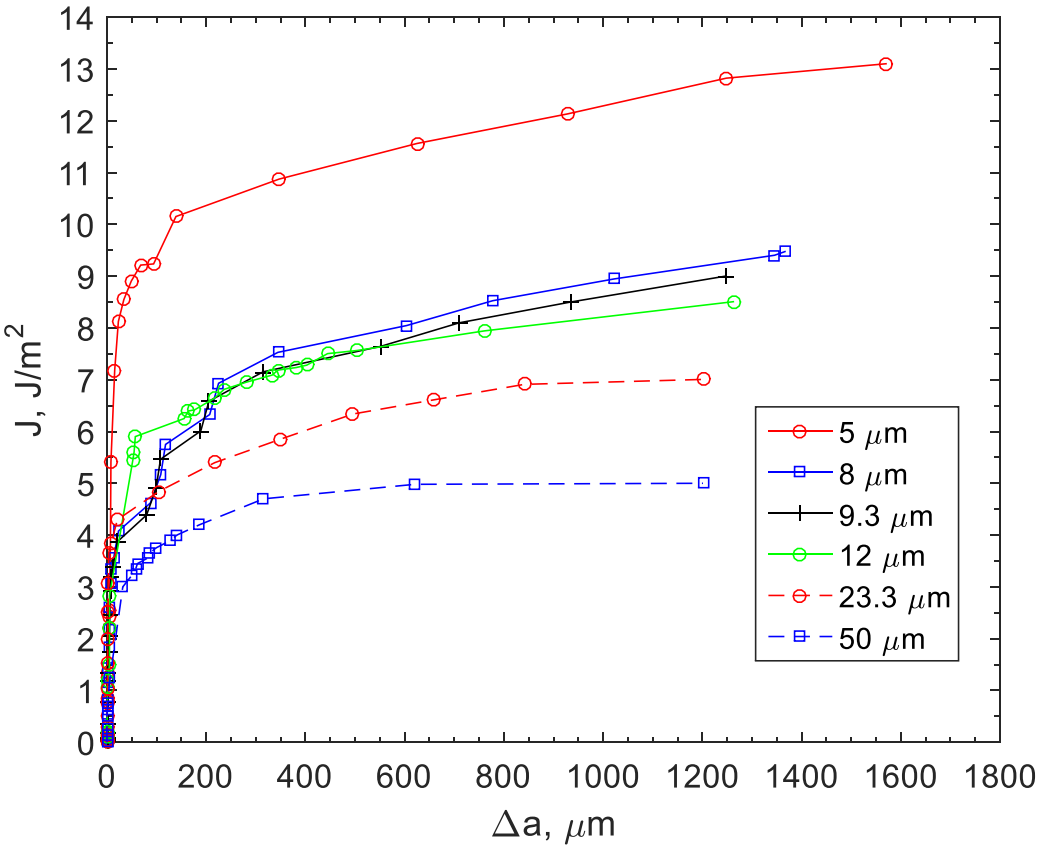

Figure 5: Fracture resistance curves for ELS specimens with different epoxy thicknesses.

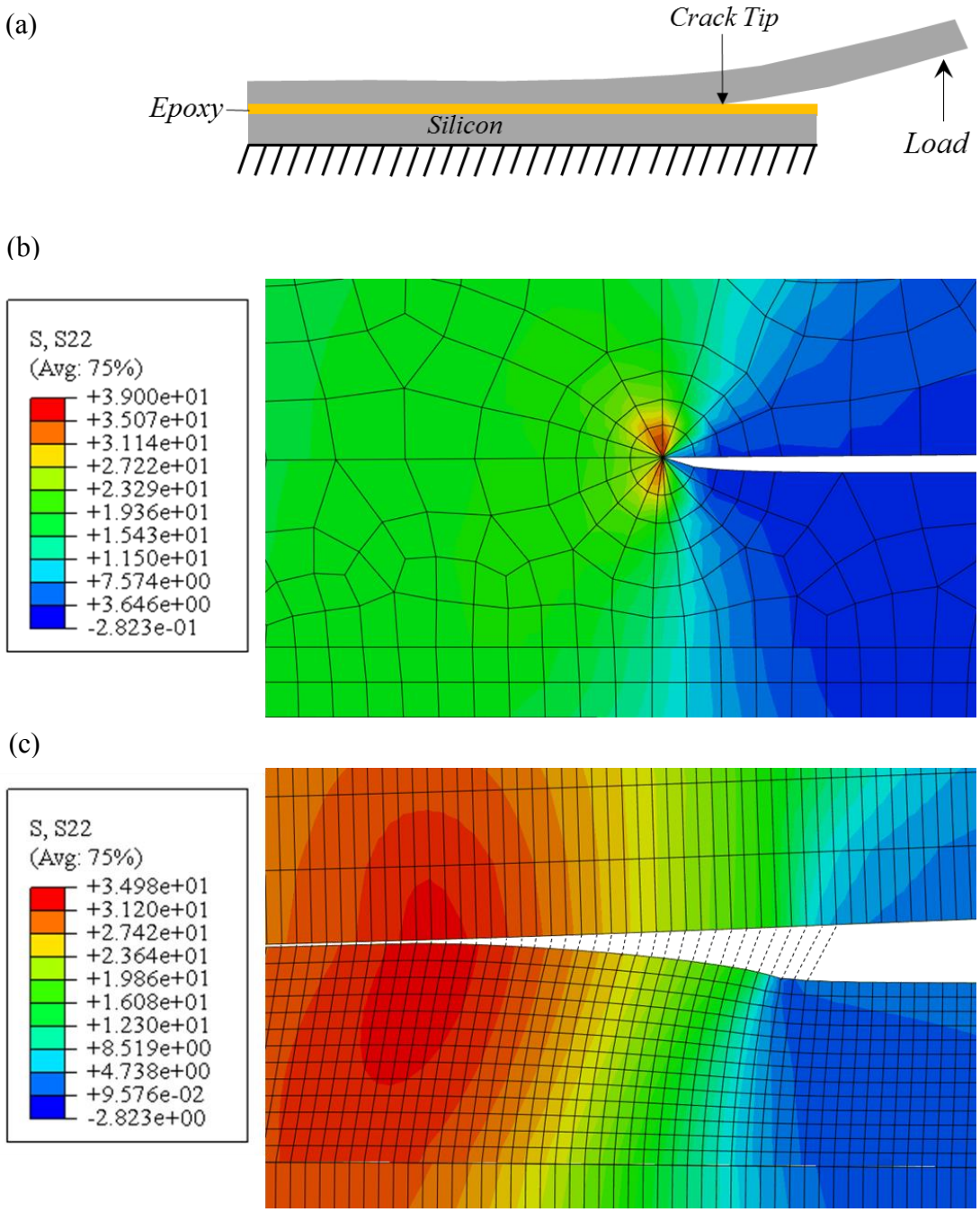

Figure 6: (a) Schematic of a 2D finite element model for the ELS experiments, (b) mesh and normal stress contour near a crack tip in a linear elastic finite element mode, (c) mesh and normal stress contour near the initial crack tip in a nonlinear finite element model with the cohesive surface interactions between silicon and epoxy.

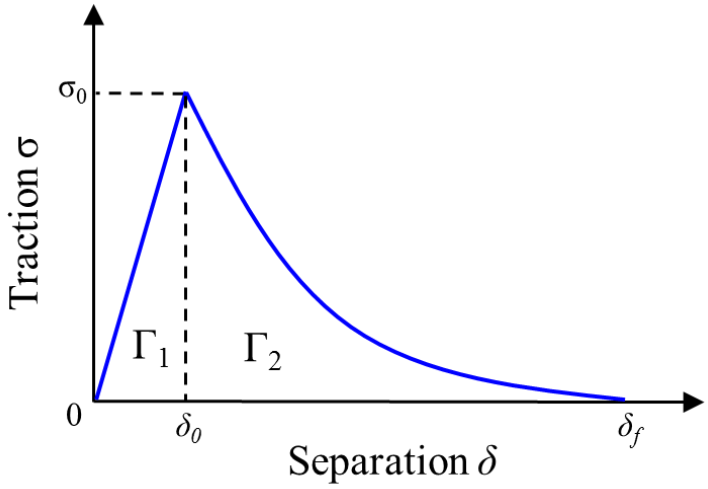

Figure 7: Schematic of a vectorial traction-separation relation.

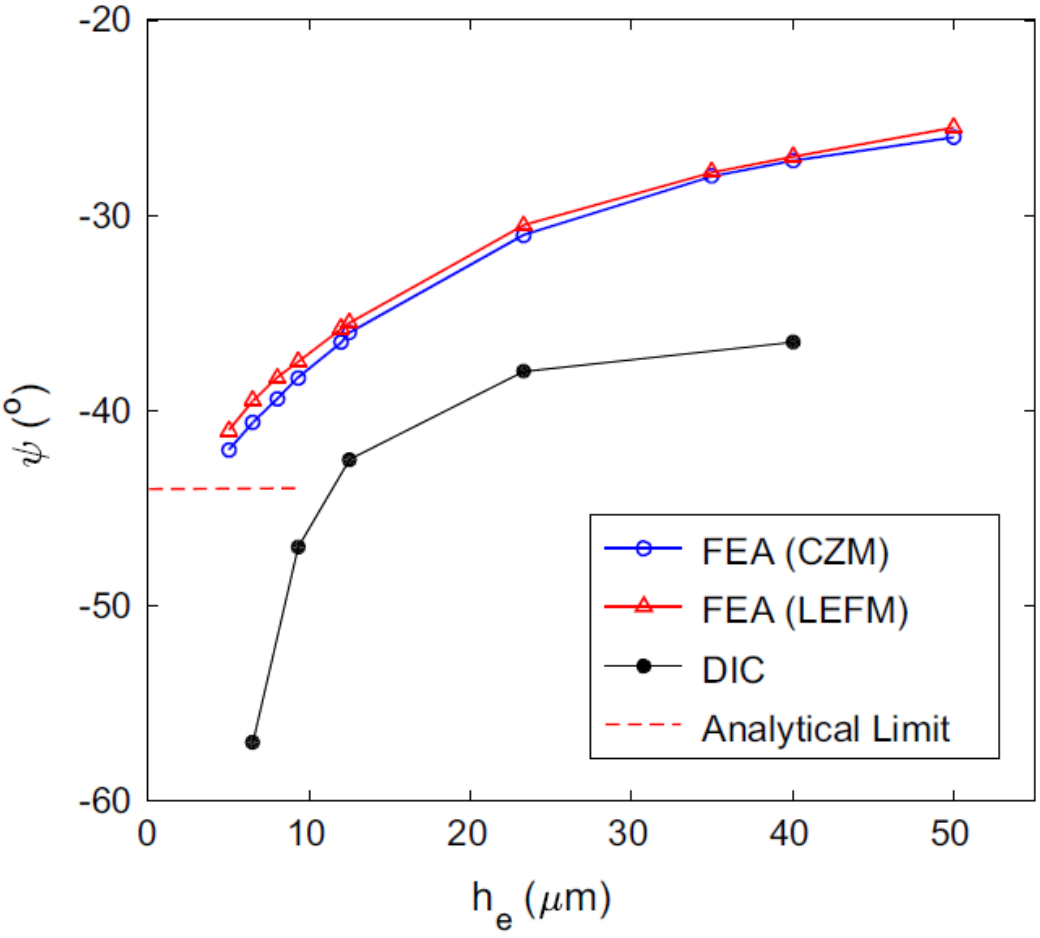

Figure 8: Variation of mode-mix with epoxy thickness in the ELS specimens

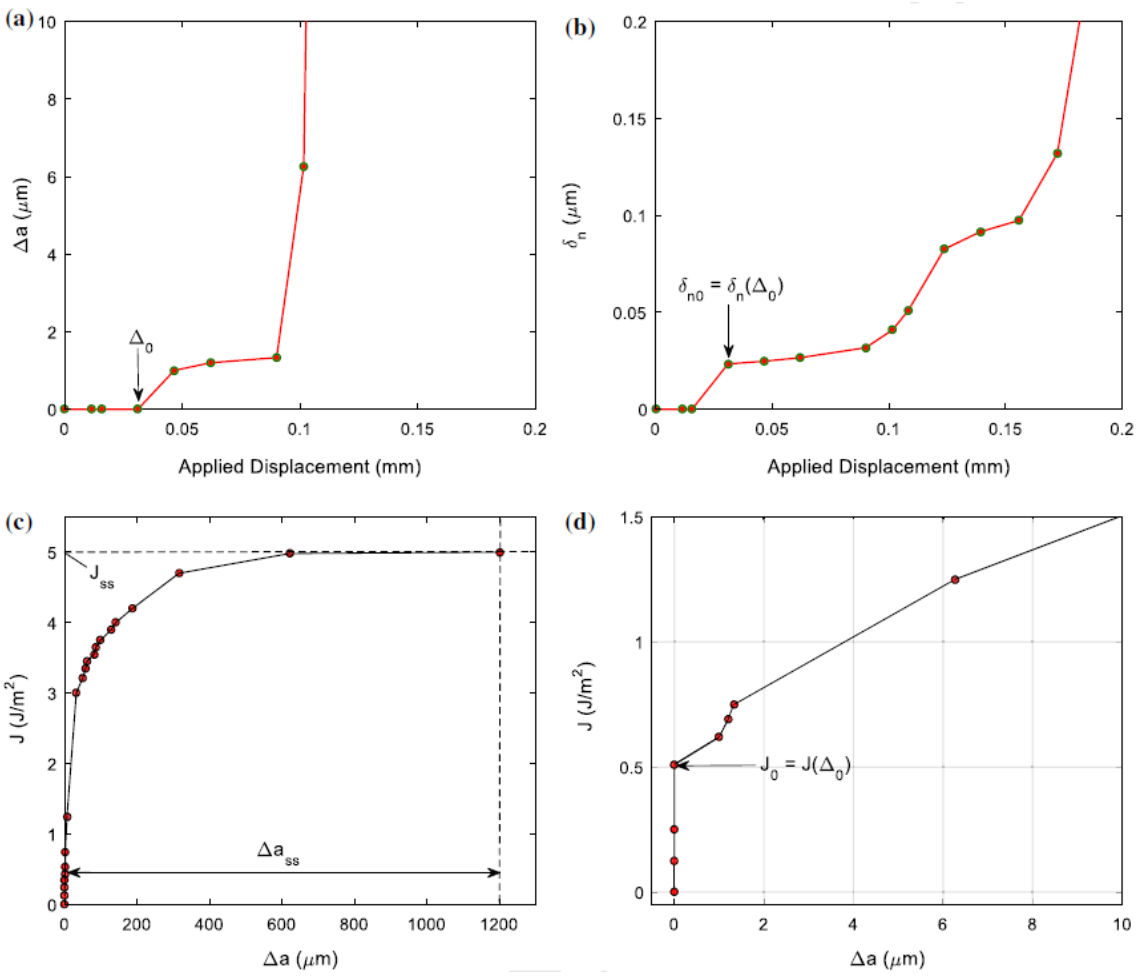

Figure 9: (a) Measured crack growth versus the applied displacement for a specimen with epoxy thickness of 50 μm, (b) measured normal CTOD versus applied displacement, (c) fracture resistance curve, (d) early portion of the fracture resistance curve.

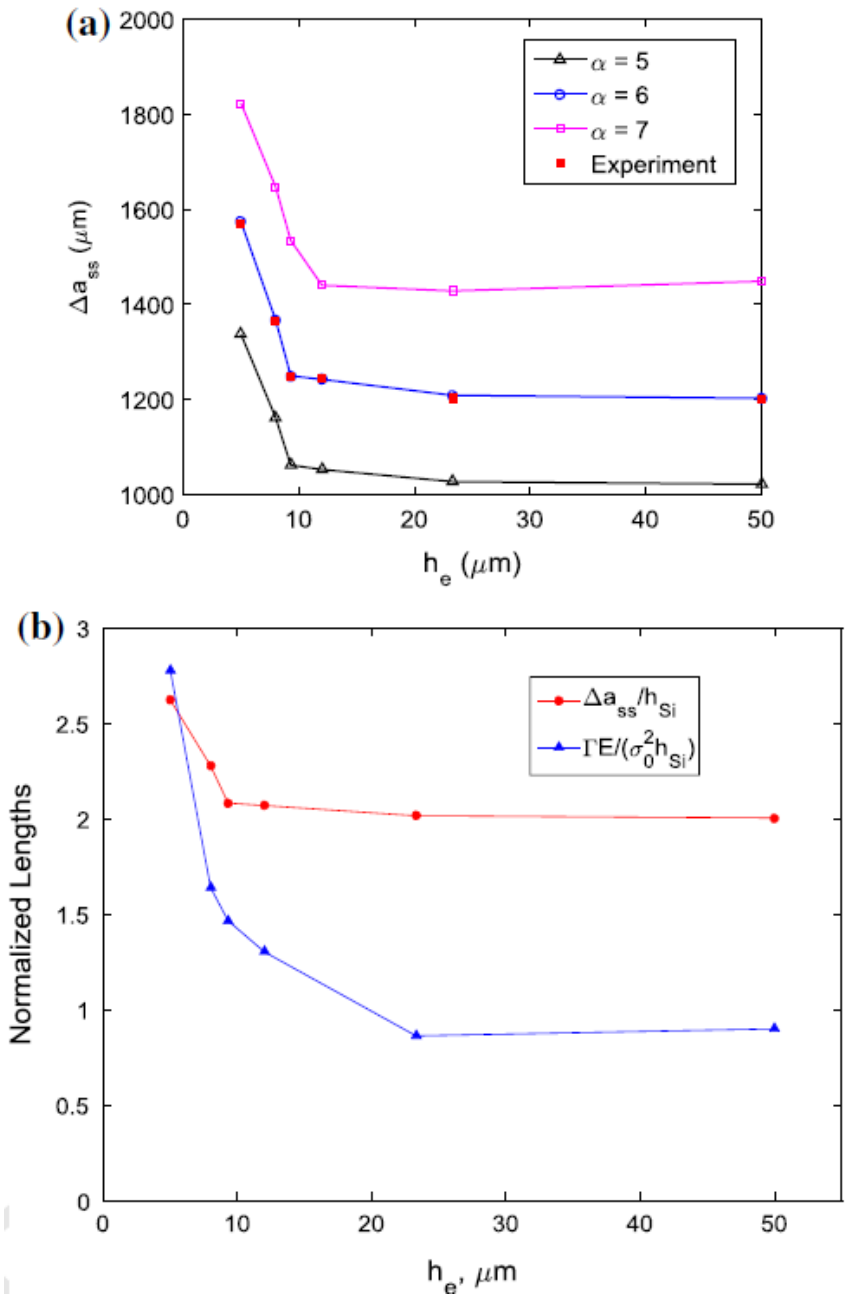

Figure 10: (a) The amount of crack growth required to reach steady state for the ELS specimens. Measured values were compared with cohesive zone models with different values of the softening parameter. (b) Comparison of the normalized values of the measured cohesive zone lengths with the normalized length scale parameter

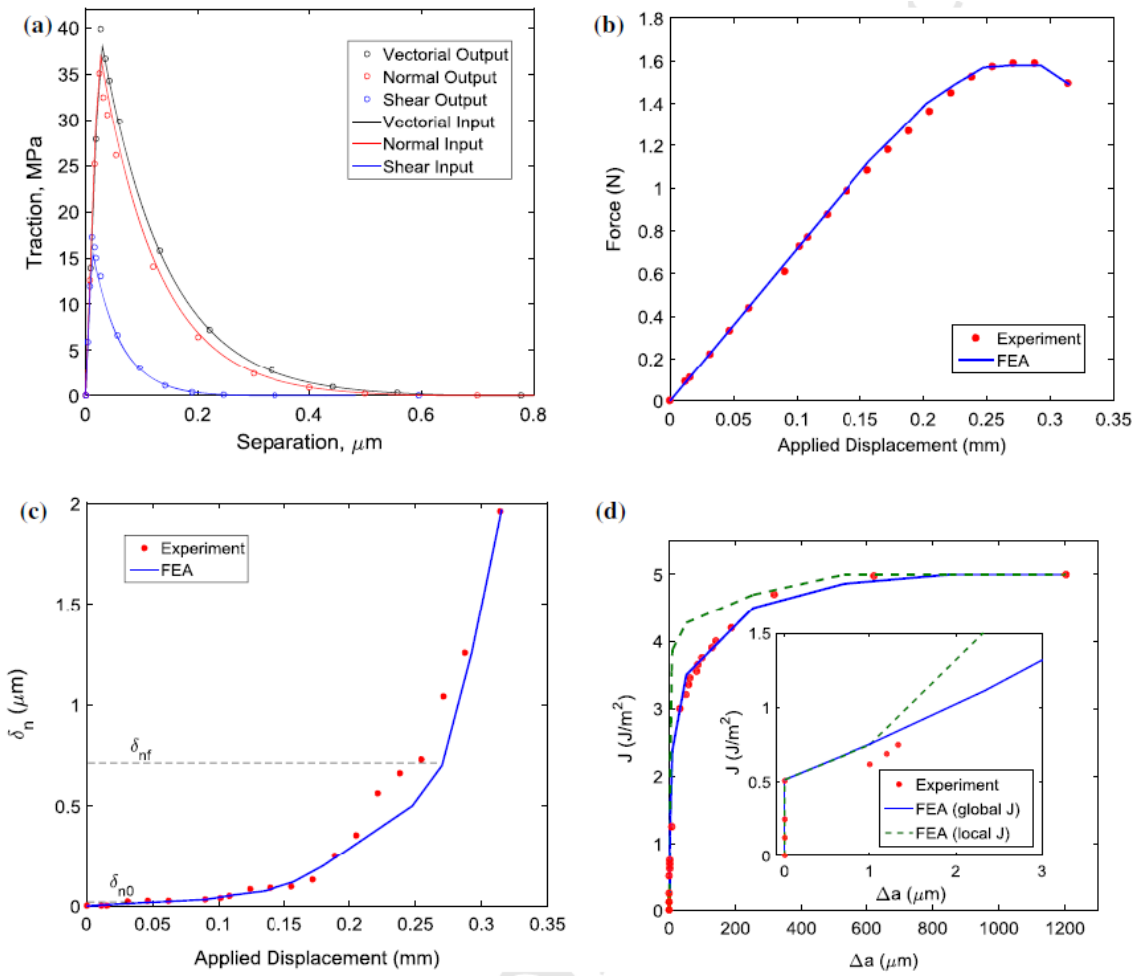

Figure 11: Comparison of experimental and FEA results for the ELS specimen with epoxy thickness of 50 μm: (a) traction-separation relations, (b) load versus displacement, (c) normal CTOD versus applied displacement, (d) fracture resistance curve.

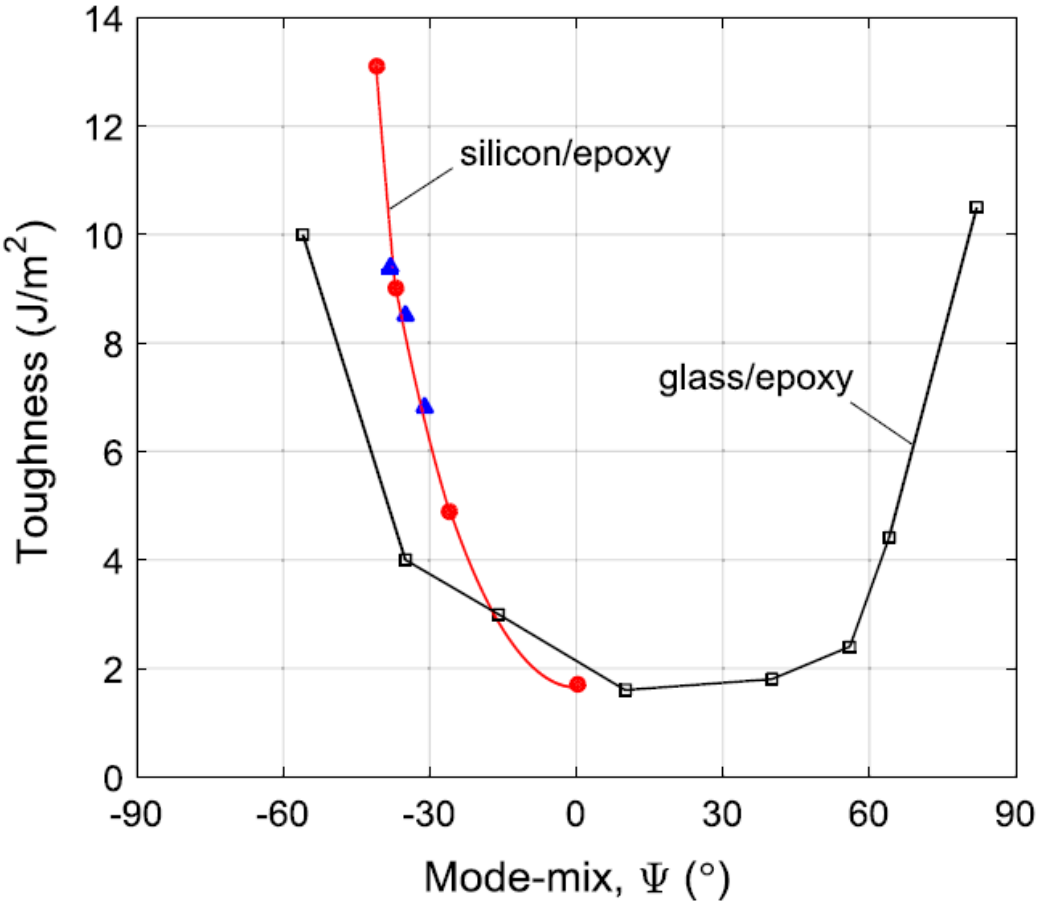

Figure 12: Mixed-mode fracture toughness by interpolation

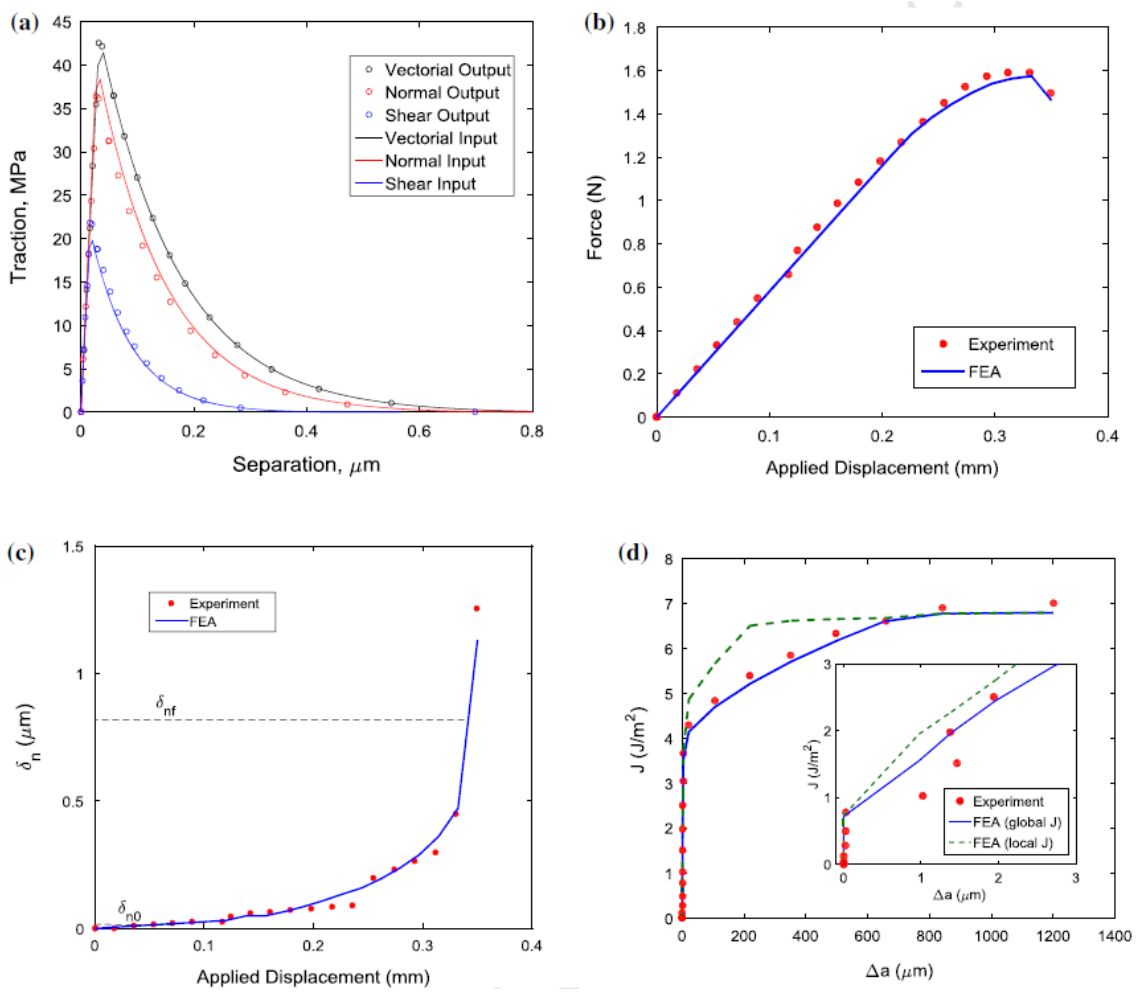

Figure 13: Comparison of experimental and FEA results for the ELS specimen with epoxy thickness of 23.3 μm: (a) traction-separation relations, (b) load versus displacement, (c) normal CTOD versus applied displacement, (d) fracture resistance curve.

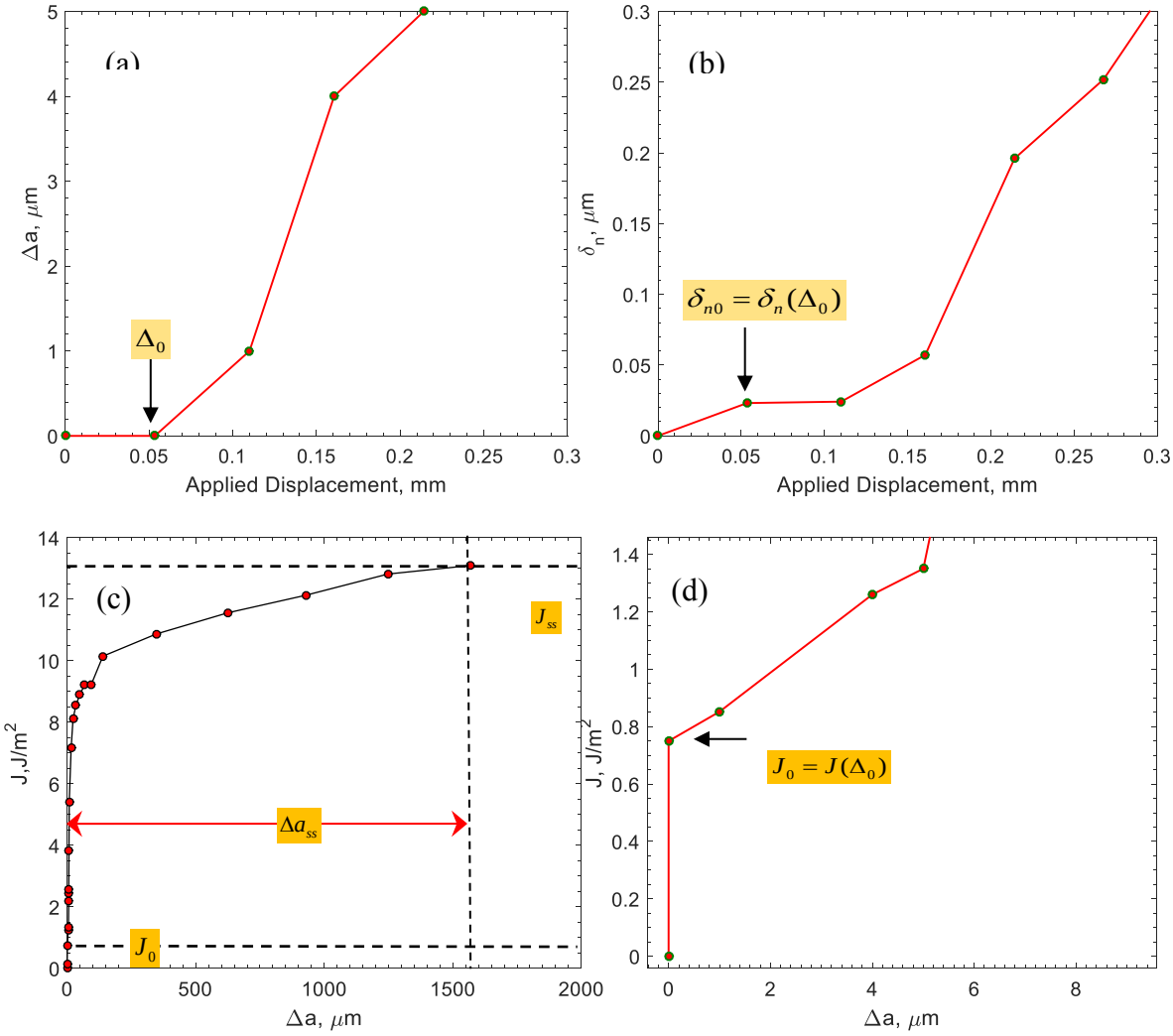

Figure 14: (a) Measured crack growth versus the applied displacement for a specimen with epoxy thickness of 5 μm, (b) Measured normal CTOD versus applied displacement, (c) Fracture resistance curve, (d) Early portion of the fracture resistance curve.

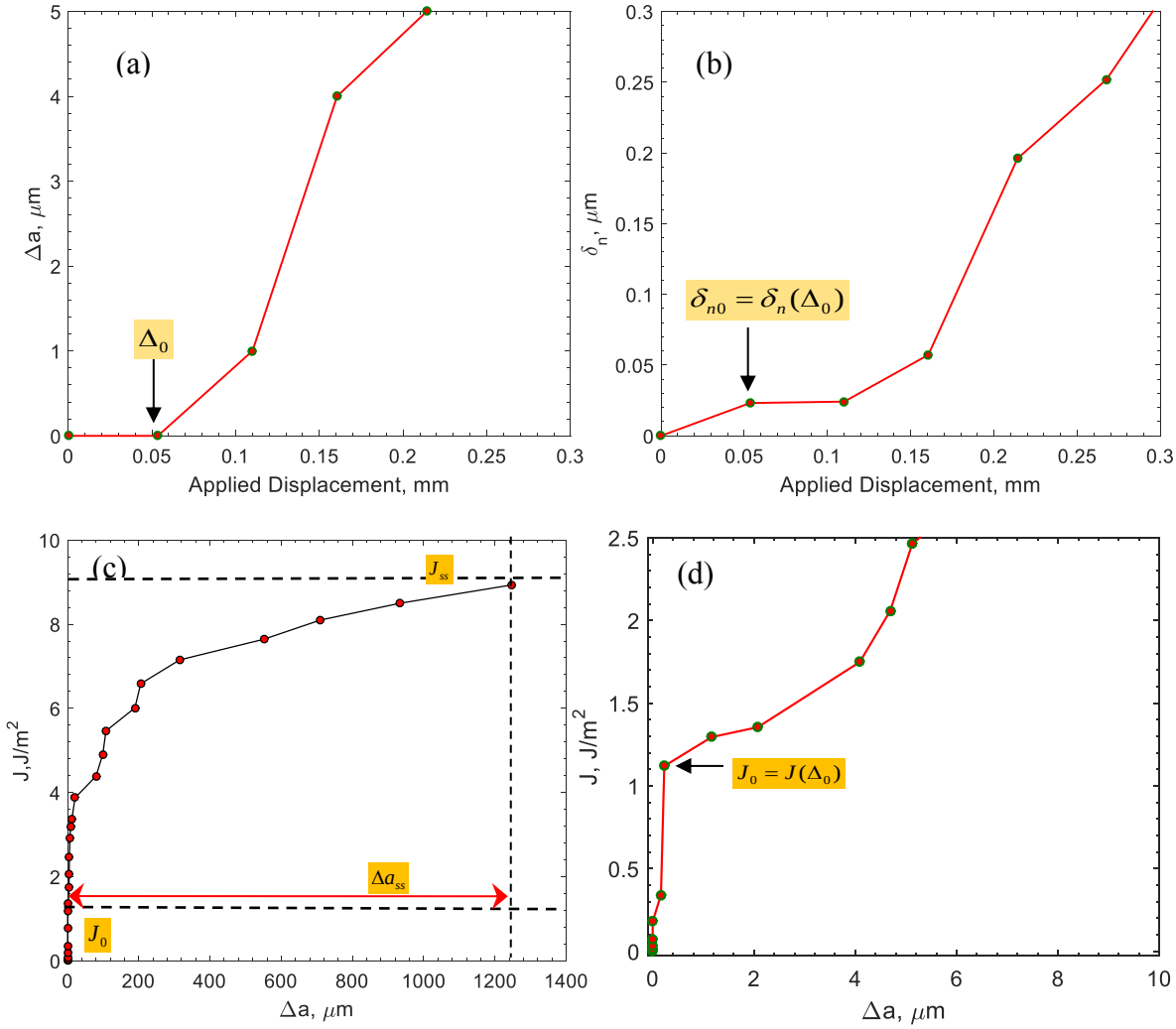

Figure 15: (a) Measured crack growth versus the applied displacement for a specimen with epoxy thickness of 9.3 μm, (b) measured normal CTOD versus applied displacement, (c) Fracture resistance curve, (d) early portion of the fracture resistance curve.

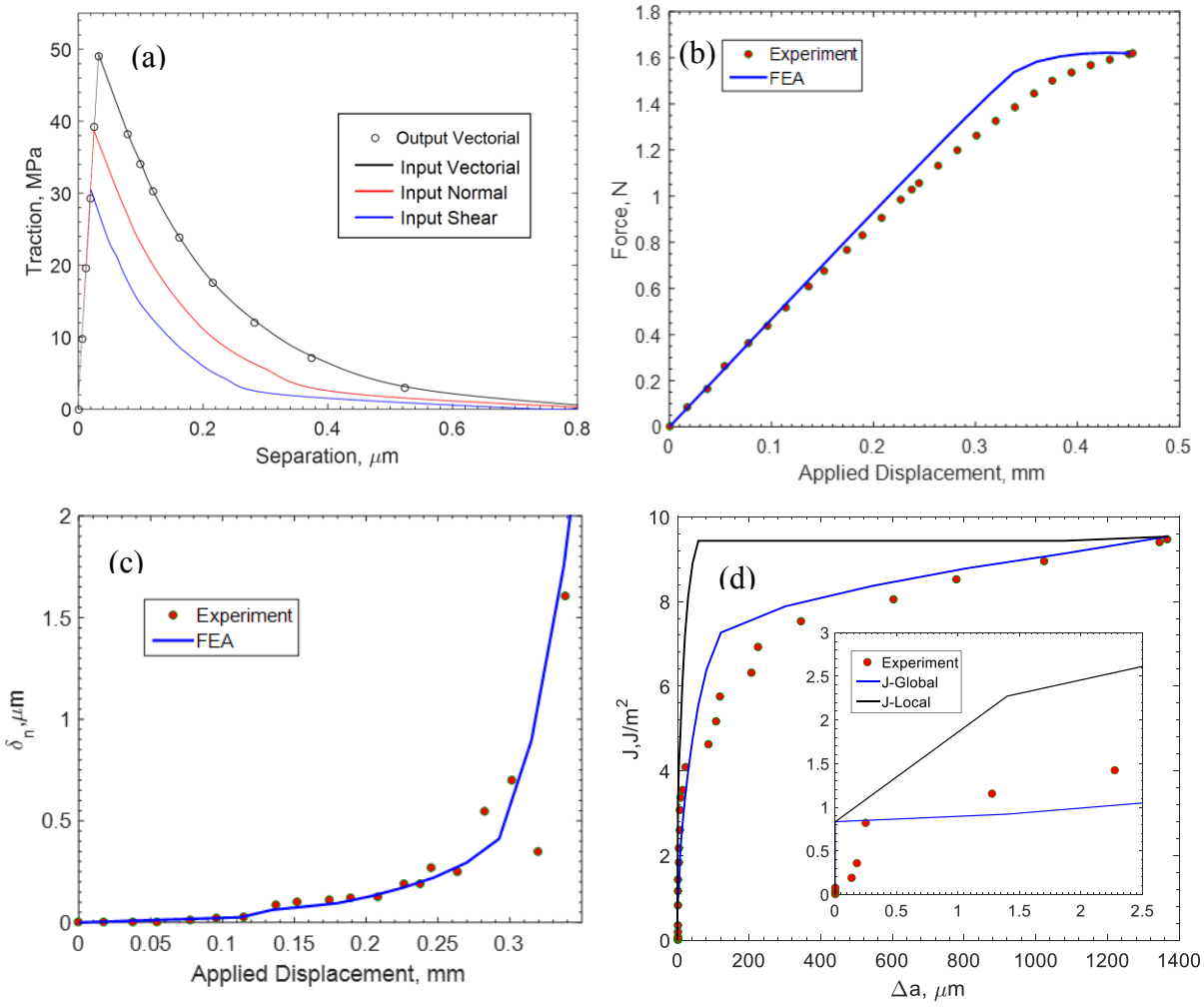

Figure 16: Comparison of experimental and FEA results with tabular input for epoxy thickness of 8 µm: (a) traction separation relationship, (b) load versus displacement curve, (c) normal crack tip opening displacement versus applied displacement curve, (d) resistance curve .

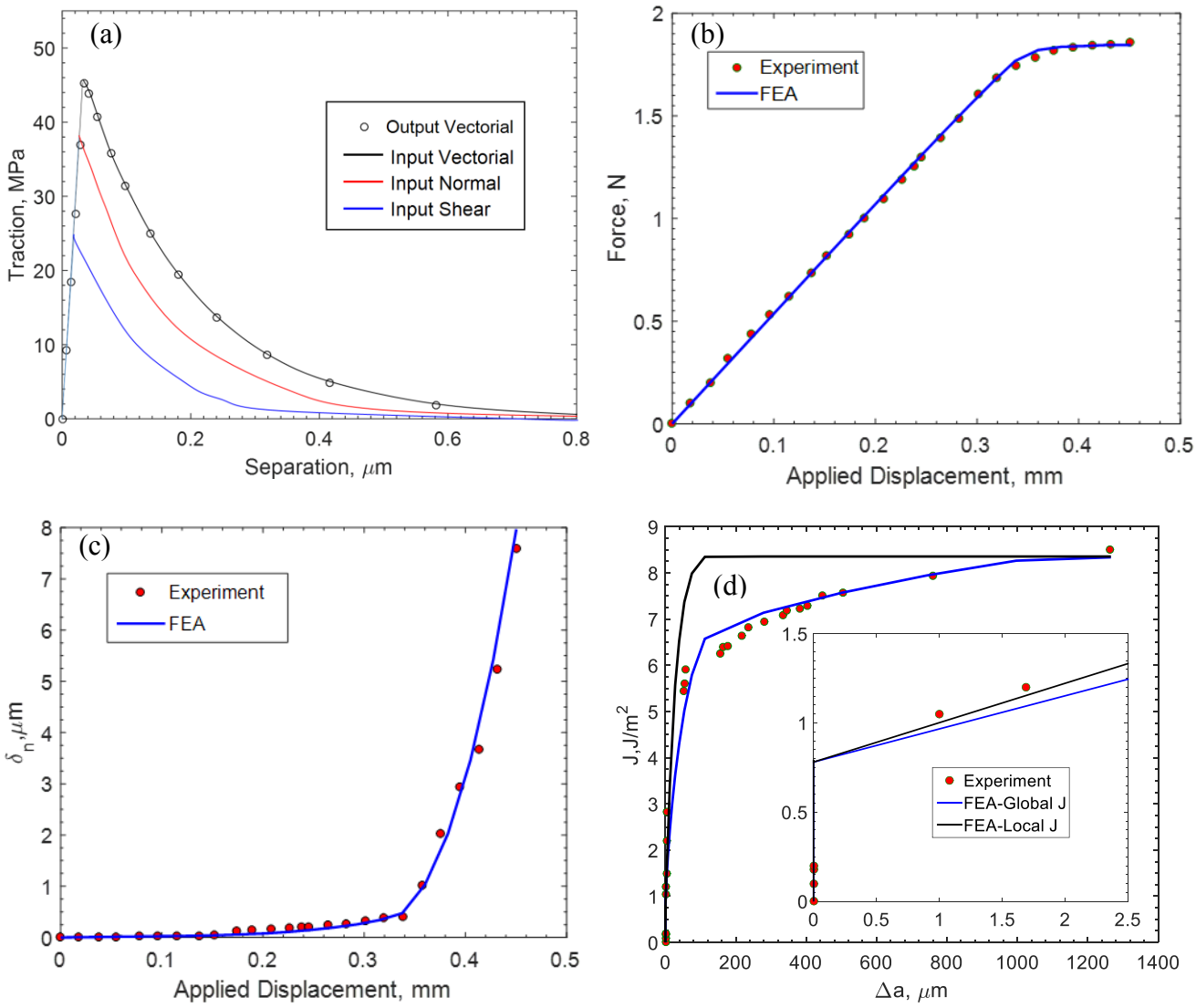

Figure 17: Comparison of experimental and FEA results with tabular input for epoxy thickness of 12 µm: (a) traction separation relationship, (b) load versus displacement curve, (c) normal crack tip opening displacement versus applied displacement curve, (d) resistance curve .

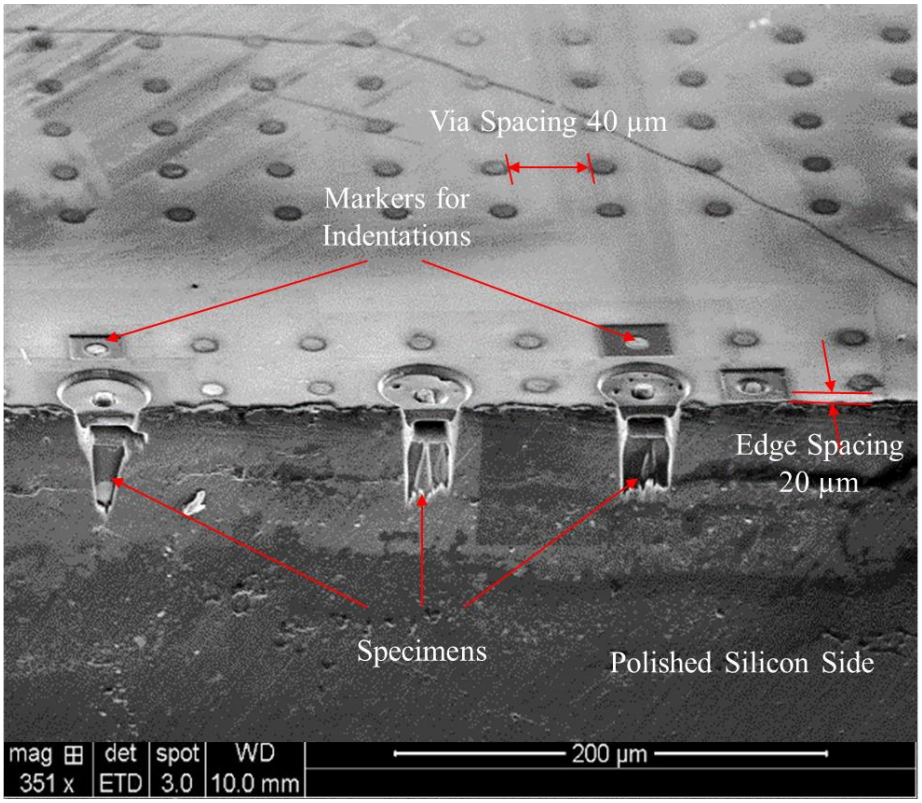

Figure 18: TSV pushout specimens prepared by FIB.

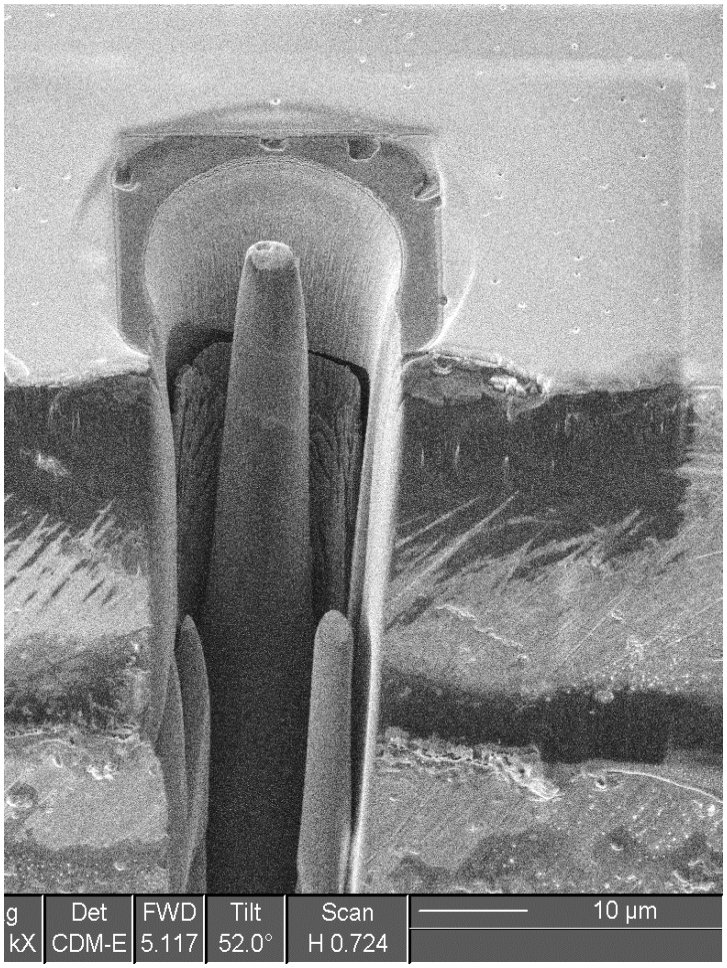

Figure 19: Copper micro-pillar specimen.

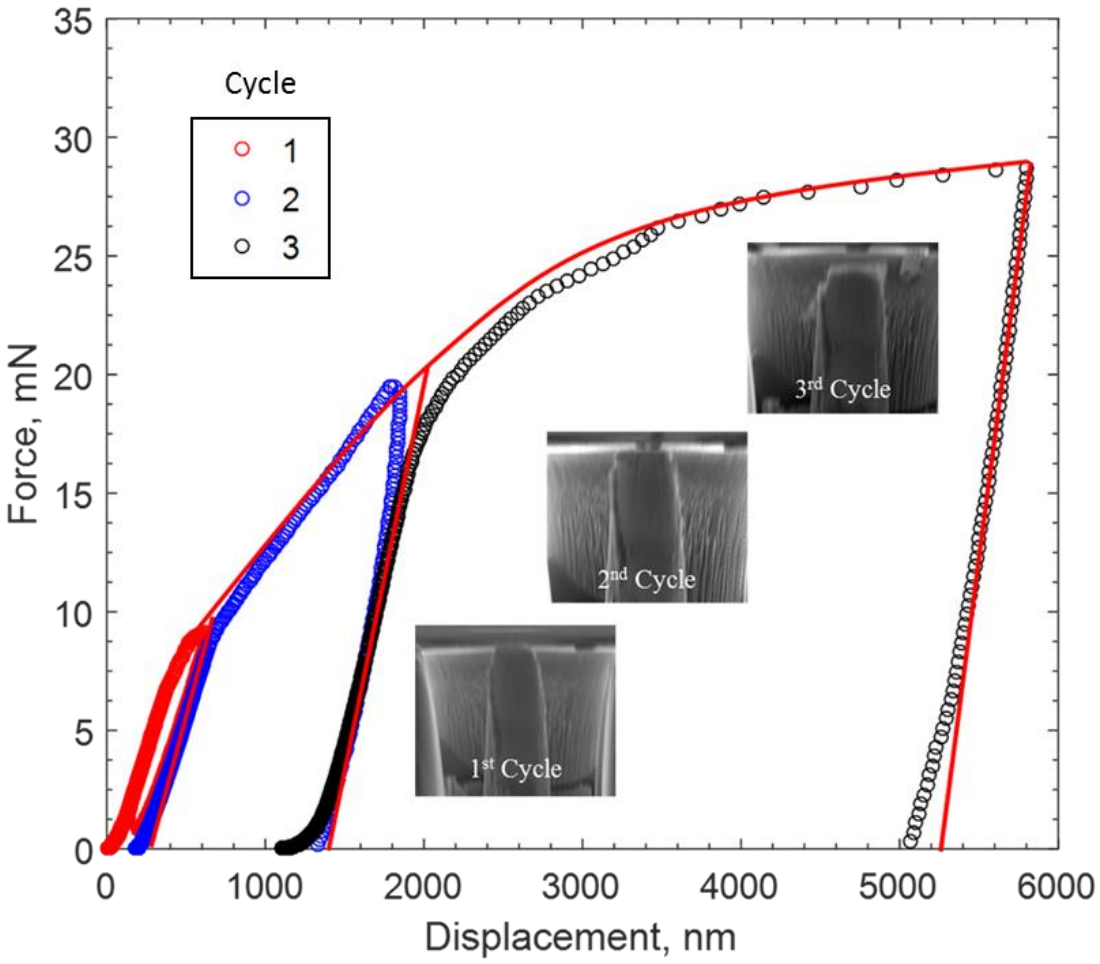

Figure 20: The force-displacement response of a copper micro-pillar.

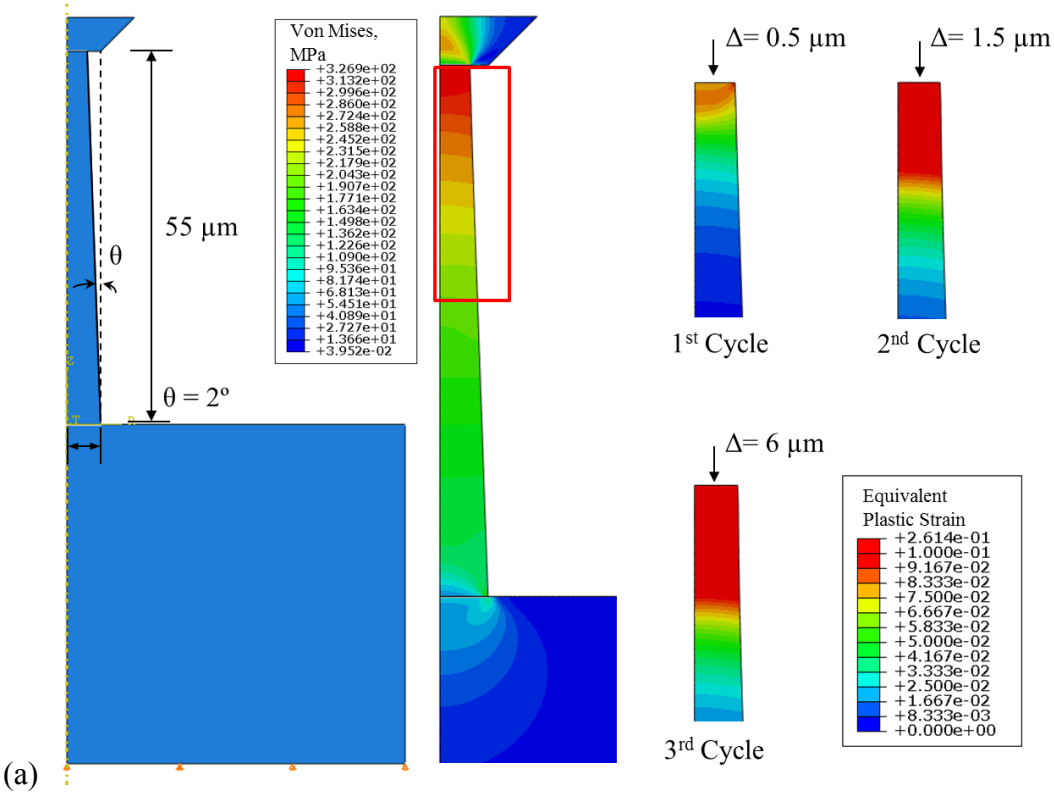

Figure 21: Finite element model of micro-pillar compression: (a) stress and plastic strain contours,

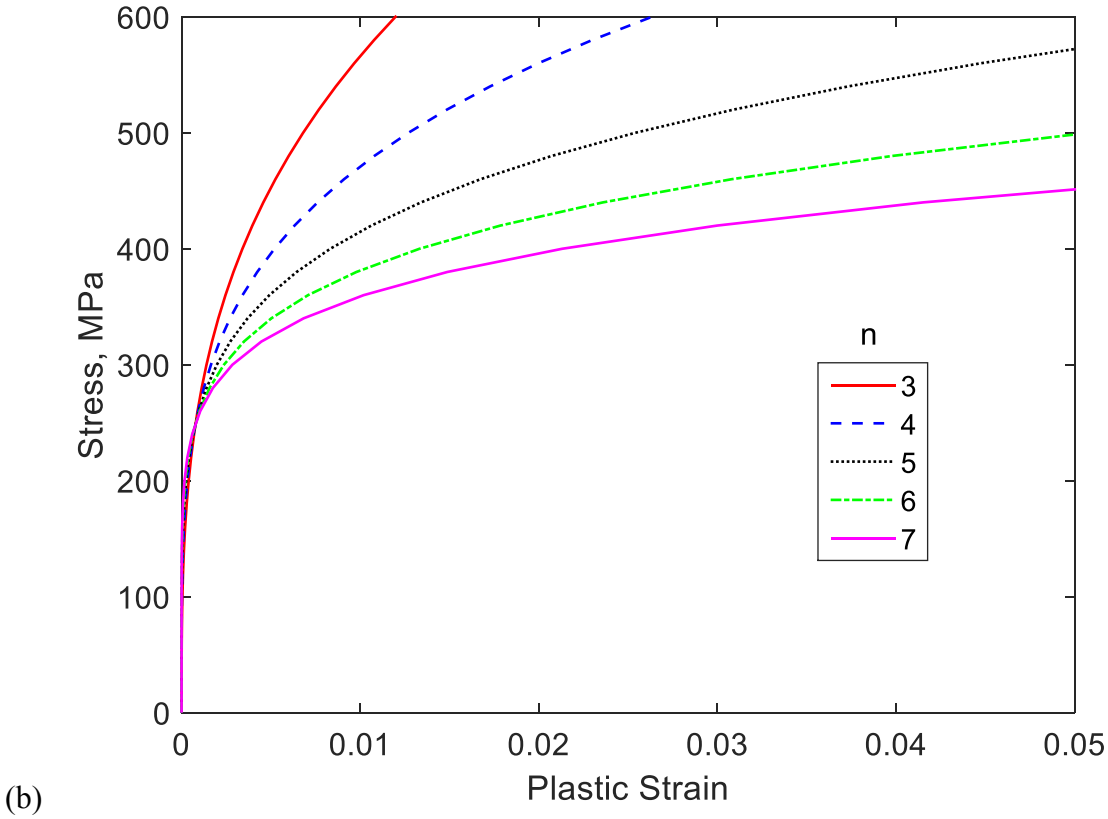

(b)

Figure 22: Finite element model of micro-pillar compression: (a) stress and plastic strain contours, (b) effect of hardening exponent on stress-strain behavior.

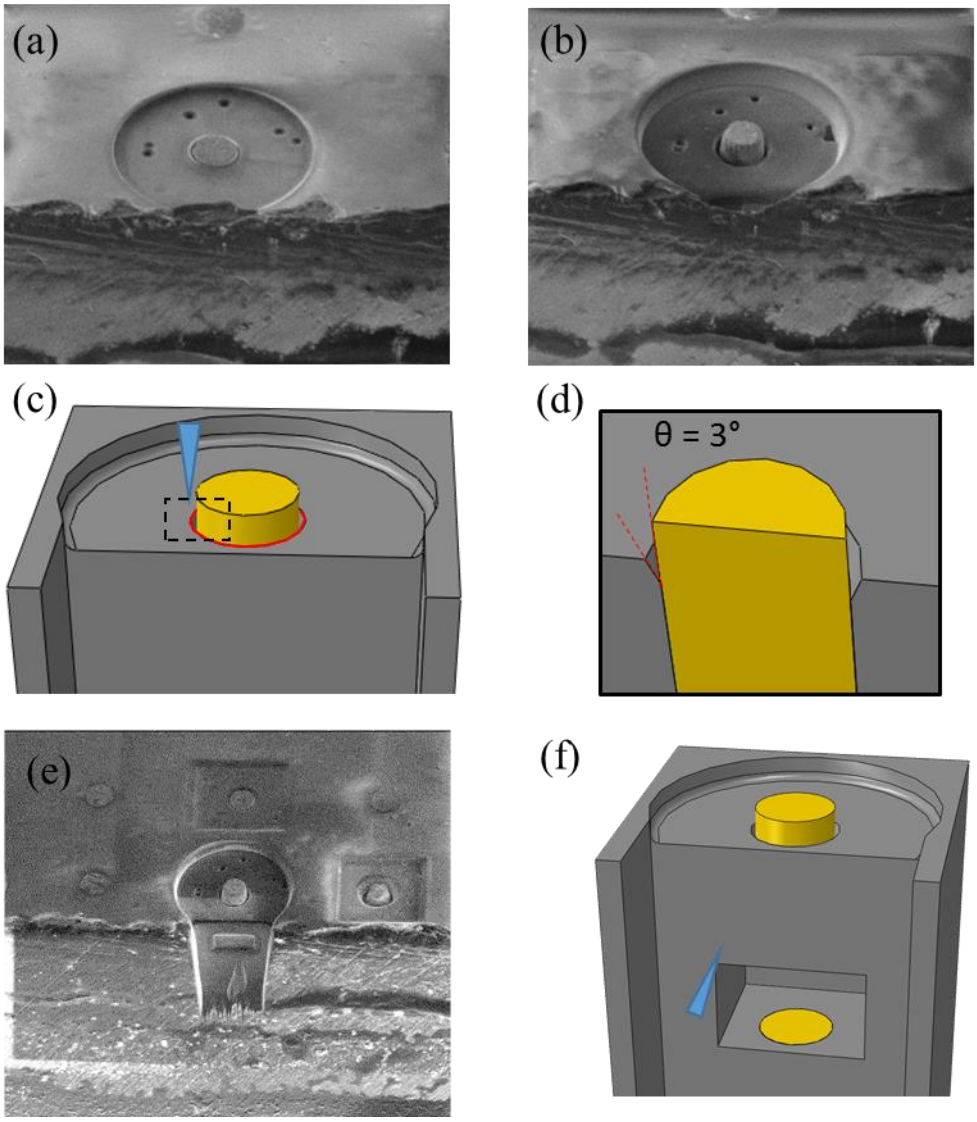

Figure 23: FIB milling of a TSV pushout specimen: (a) top surface removal; (b) forming an annular crack, (c) forming a draft angle of 3°; (d) free-standing via with an annular crack, (e) a schematic of side opening and (f) edge view of side opening in process.

(a)

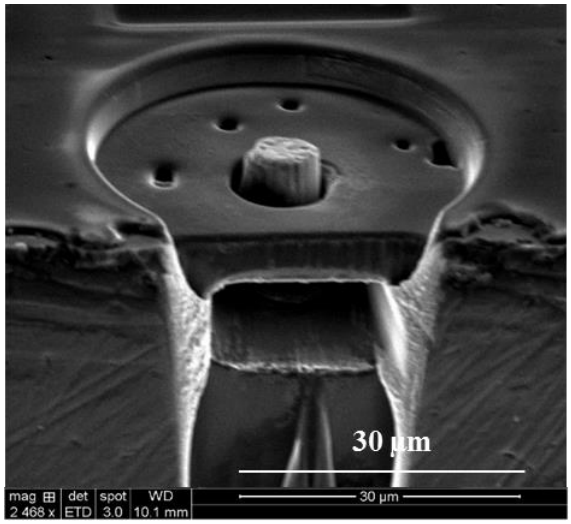

(b)

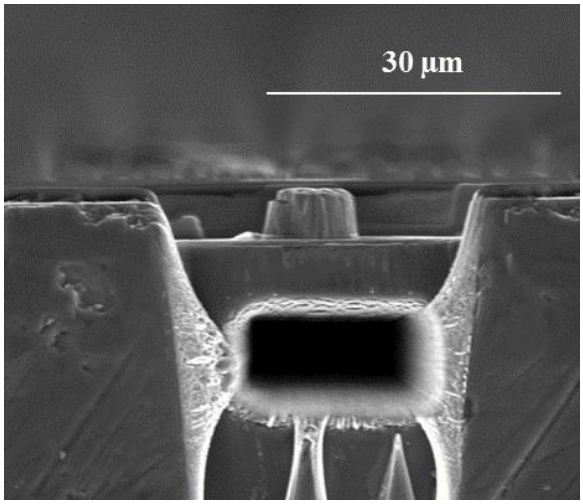

Figure 24: The TSV pushout specimen: (a) 52 degree tilted view, (b) side view.

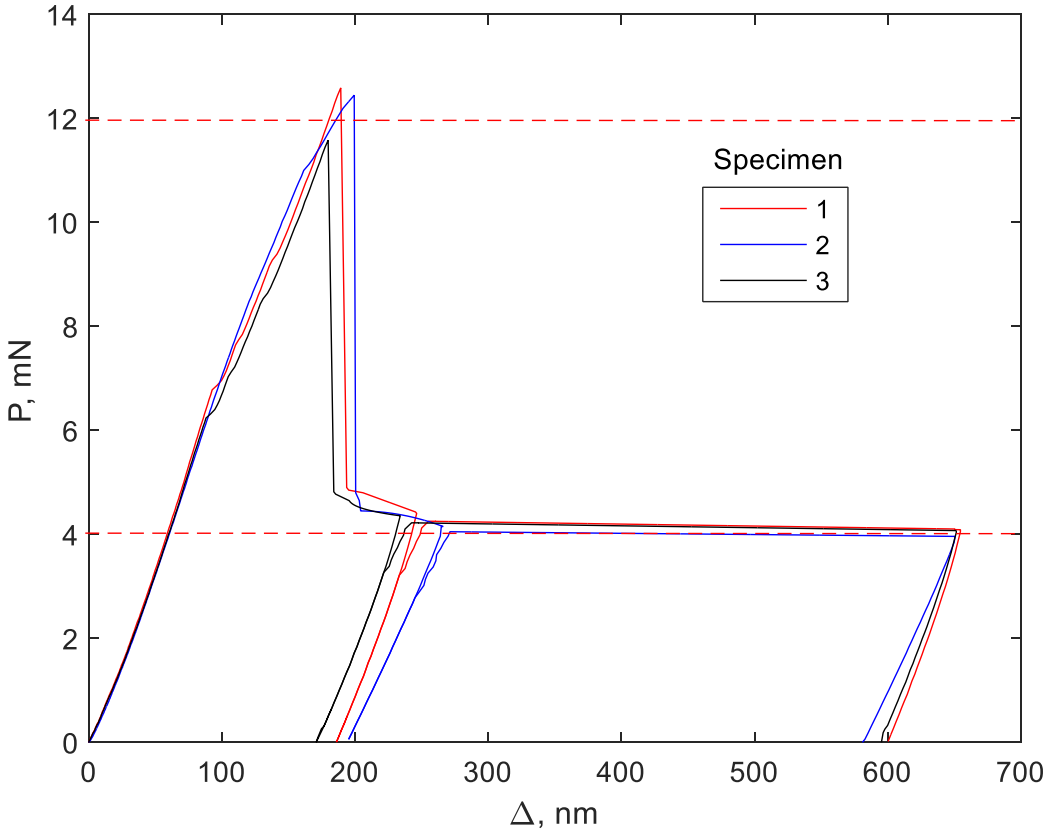

Figure 25: The force-displacement responses of TSV pushout specimens.

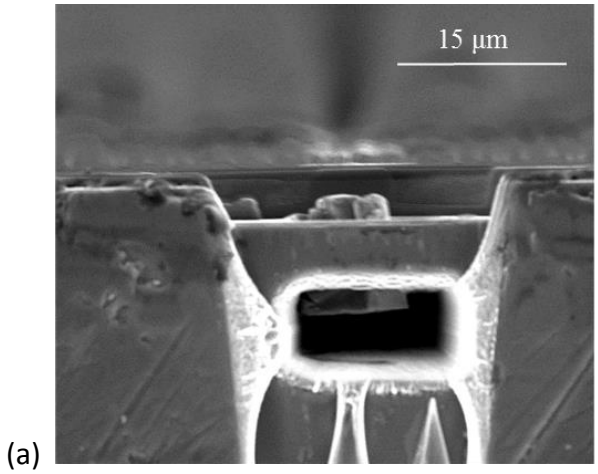

(a)

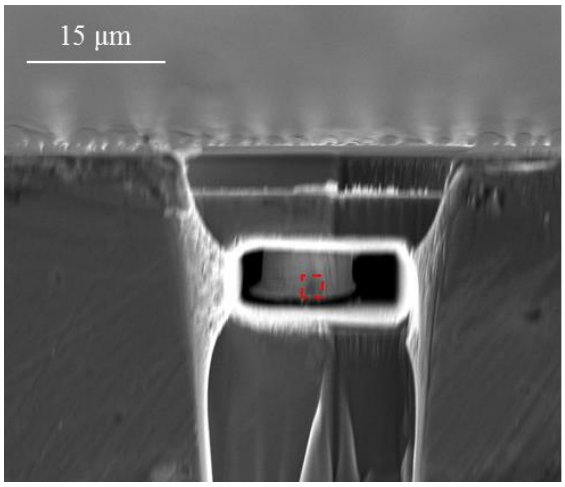

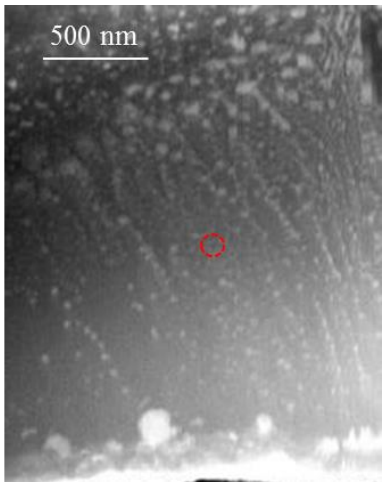

(b)

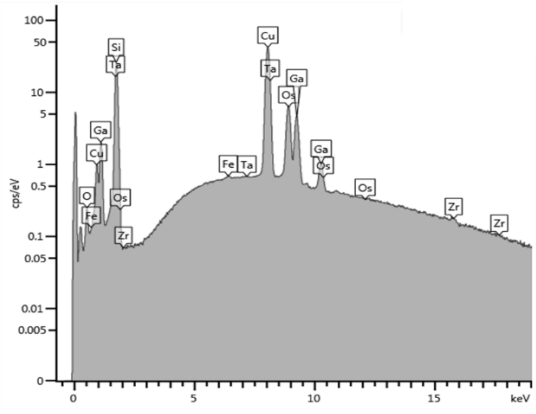

(c)

Figure 26: (a) post-failure view of a TSV pushout specimen, (b) a via that has been pushed out, (c) EDS of a via fracture surface,

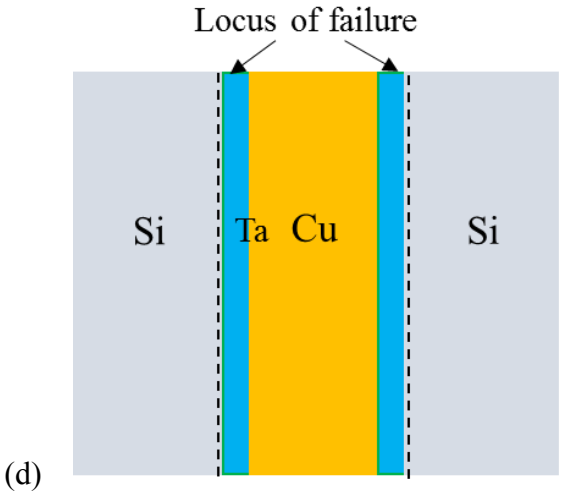

Figure 26: Identification of the locus of failure: (a) post-failure view of a TSV pushout specimen, (b) a via that has been pushed out, (c) EDS of a via fracture surface, (d) schematic of the failure locus.

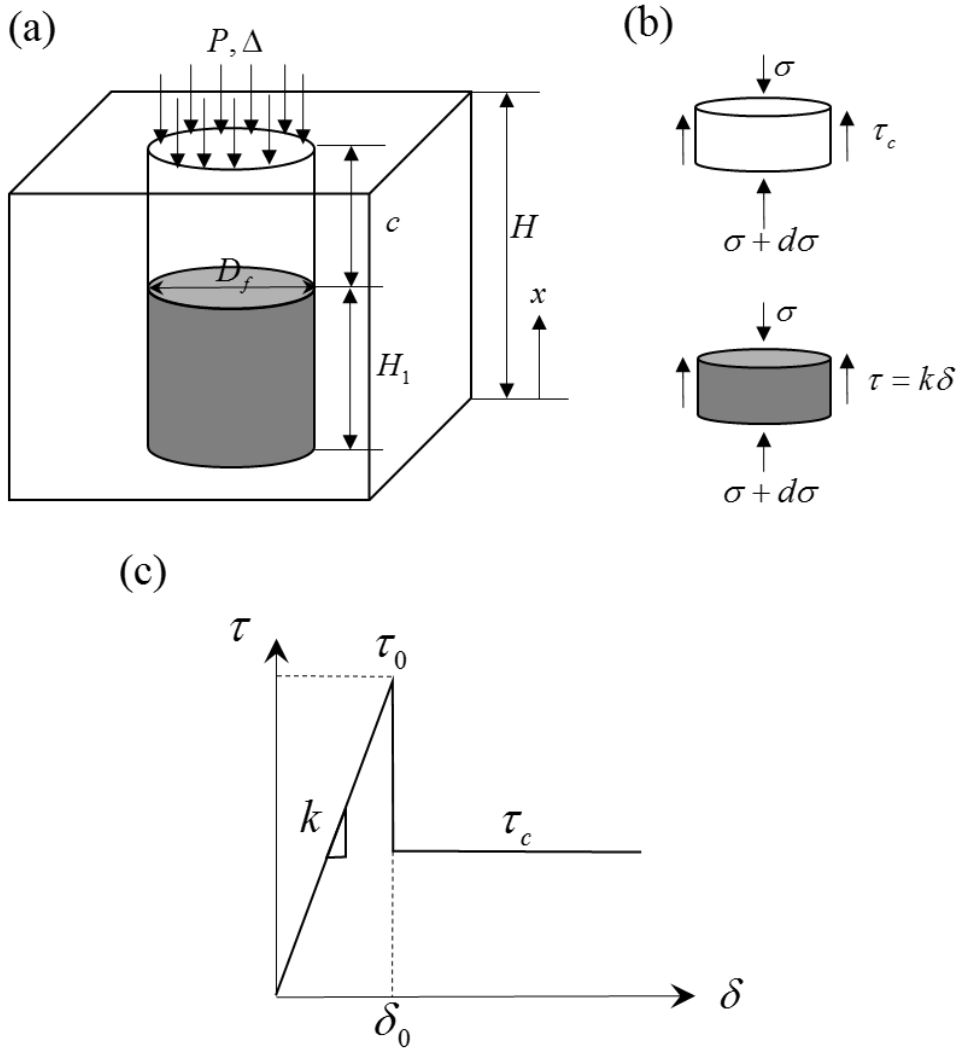

Figure 27: A shear lag model of a) the TSV pushout experiment, (b) free body diagram, (c) traction-separation relation for the interface.

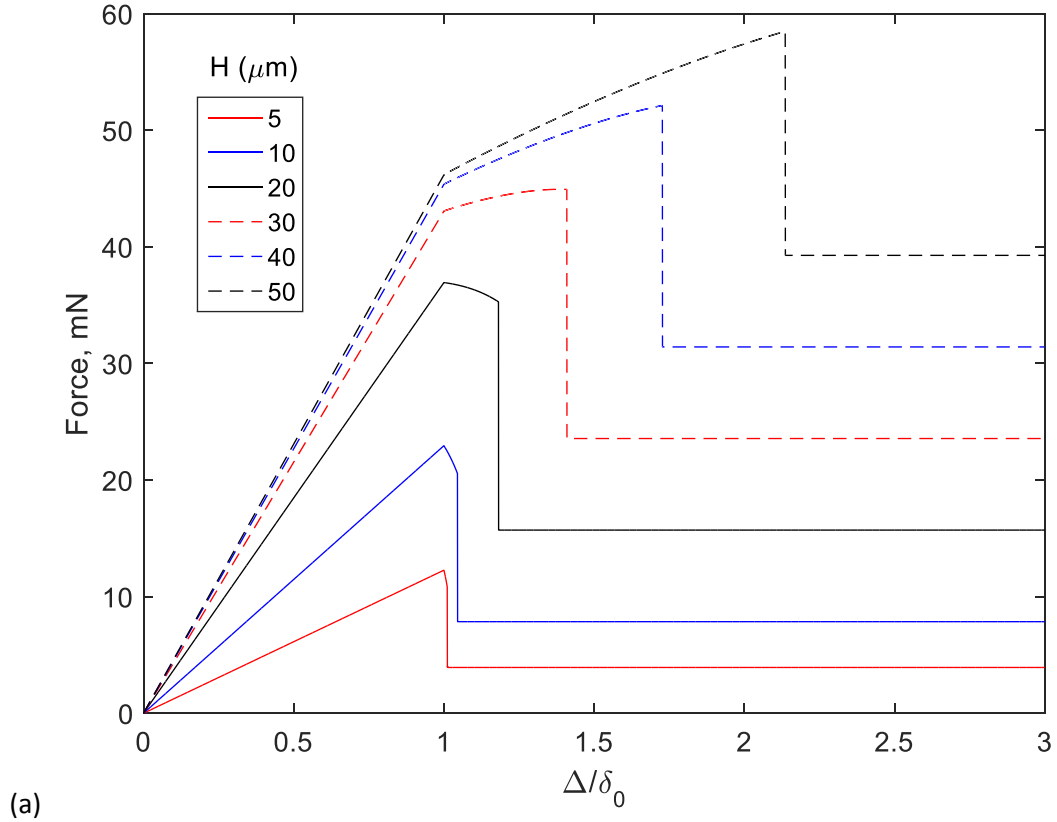

(a)

Figure 28: Results from the shear lag analysis: (a) load-displacement response,

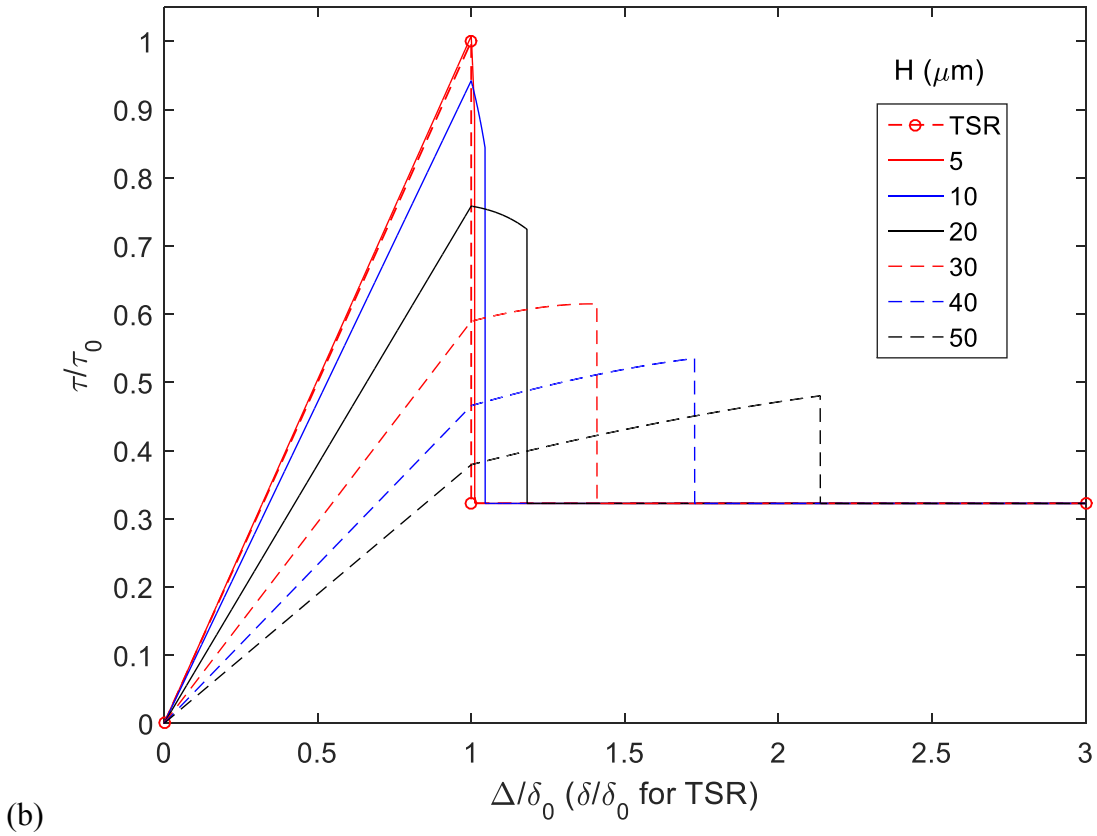

(b)

Figure 28: Results from the shear lag analysis: (a) load-displacement response, (b) shear stress-displacement response and input traction-separation relation.

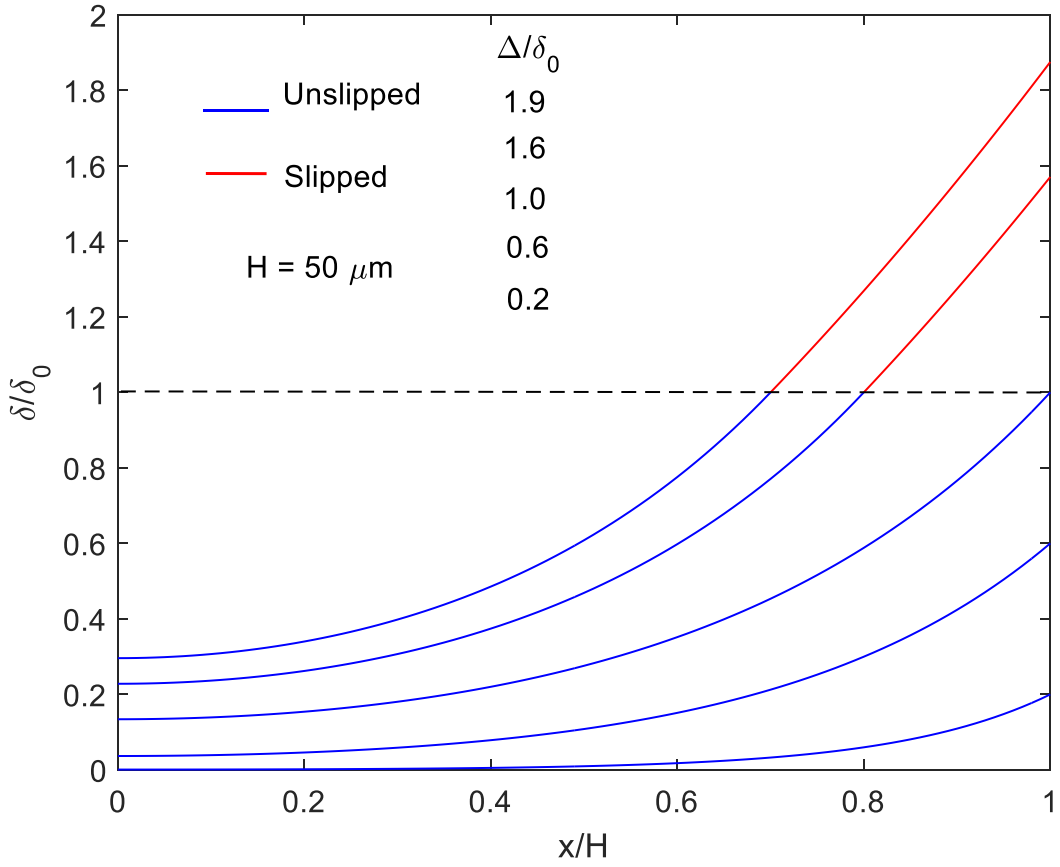

(a)

Figure 29: Effect of via length on crack growth: (a) distribution of relative displacement along interface,

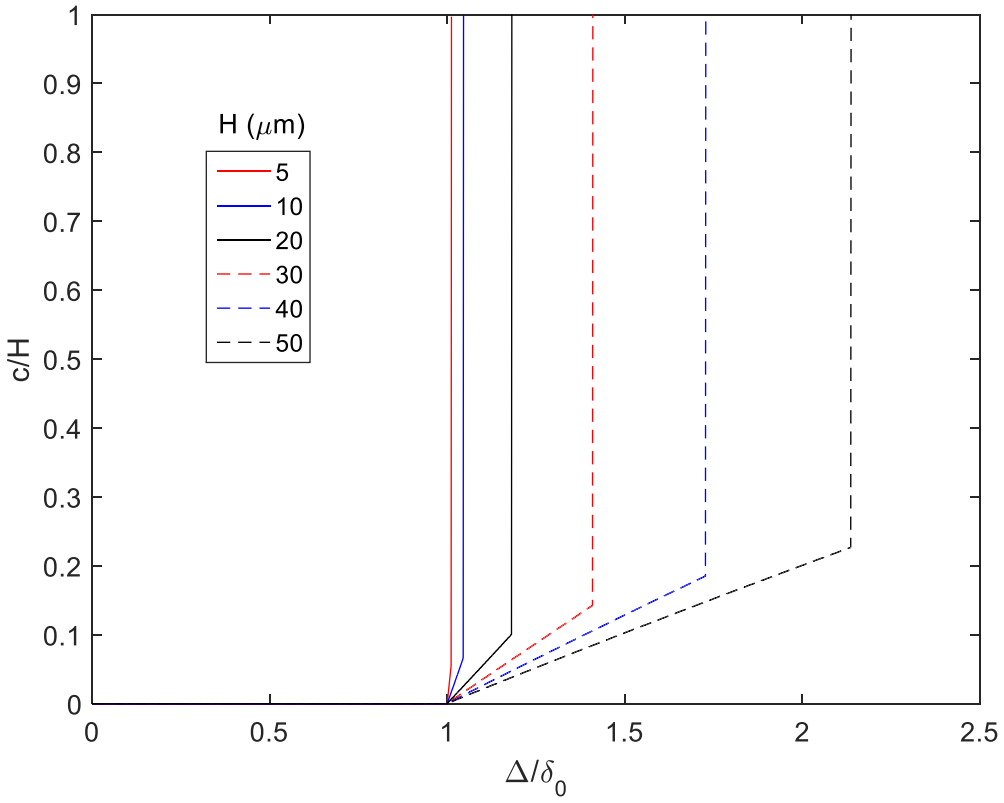

(b)

Figure 29: Effect of via length on crack growth: (b) development of slip with applied displacement,

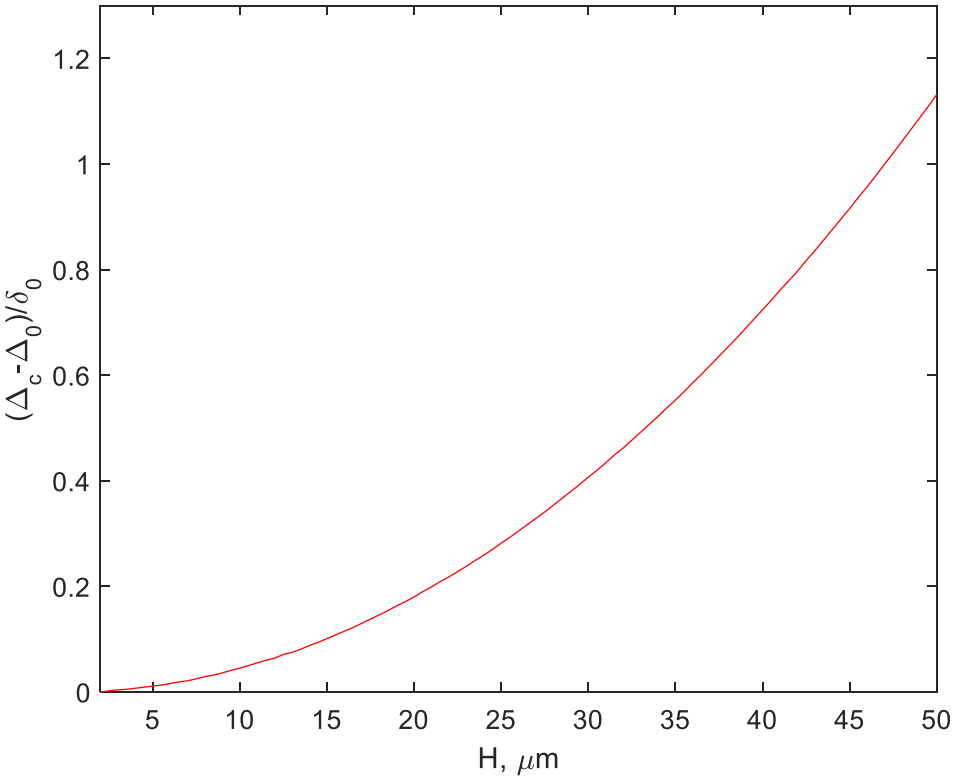

(c)

Figure 29: Effect of via length on crack growth: (a) distribution of relative displacement along interface, (b) development of slip with applied displacement, (c) effect of via length on the indenter displacement at the initiation and completion of slip.

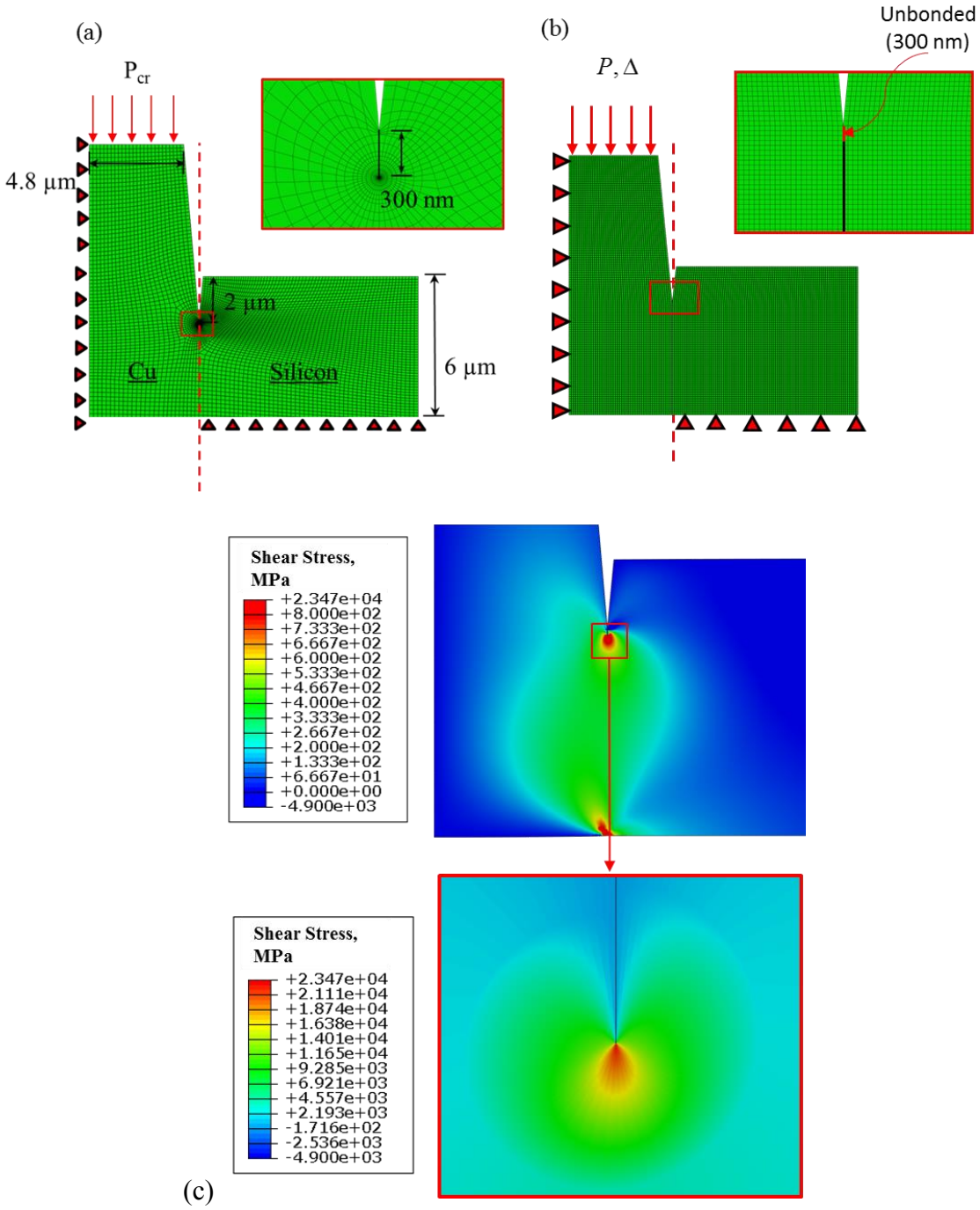

Figure 30: Finite element model: (a) LEFM model mesh, (b) cohesive zone model mesh, (c) global and local shear stress distribution.

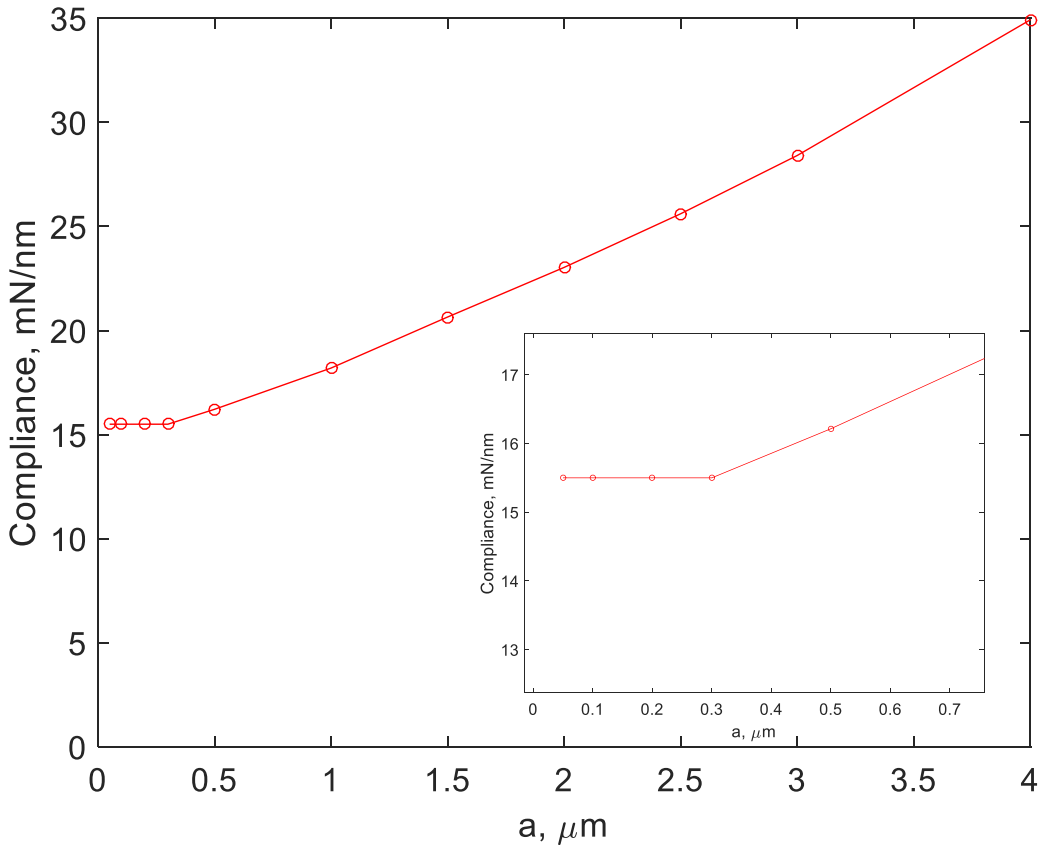

Figure 31: The effect of crack length on specimen compliance.

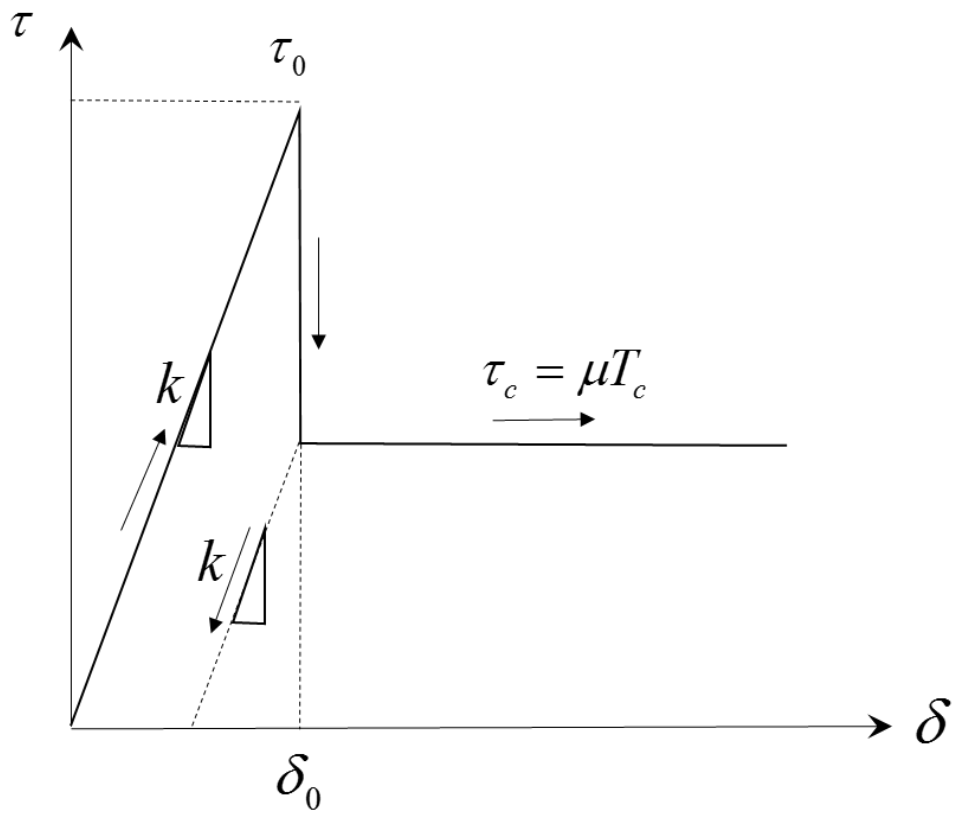

Figure 32: Shear traction-separation relation.

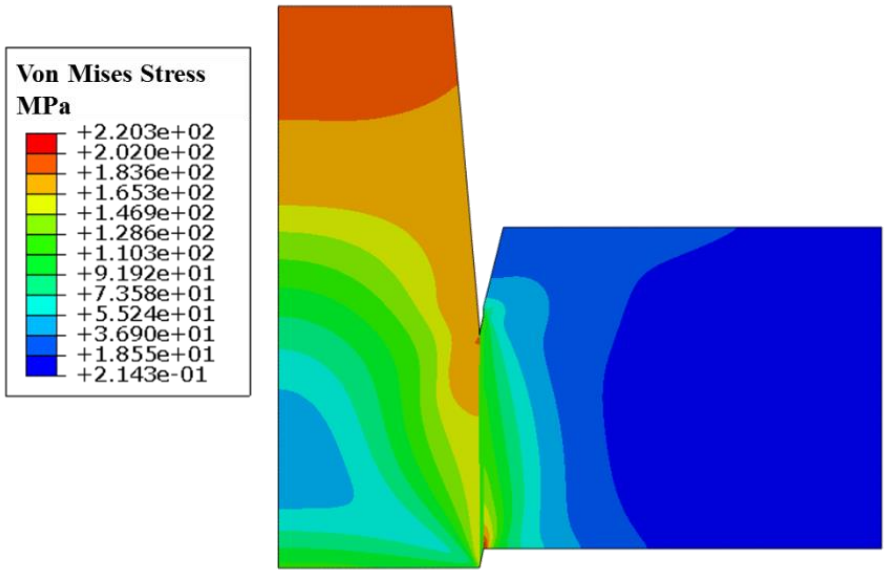

(a) .

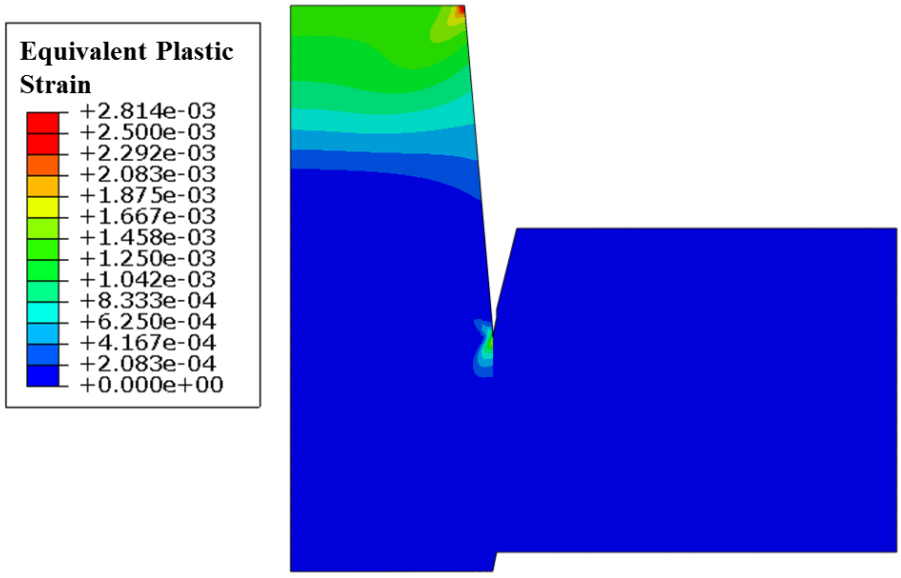

(b)

Figure 33: (a) Von Mises stress and (b) equivalent plastic strain.

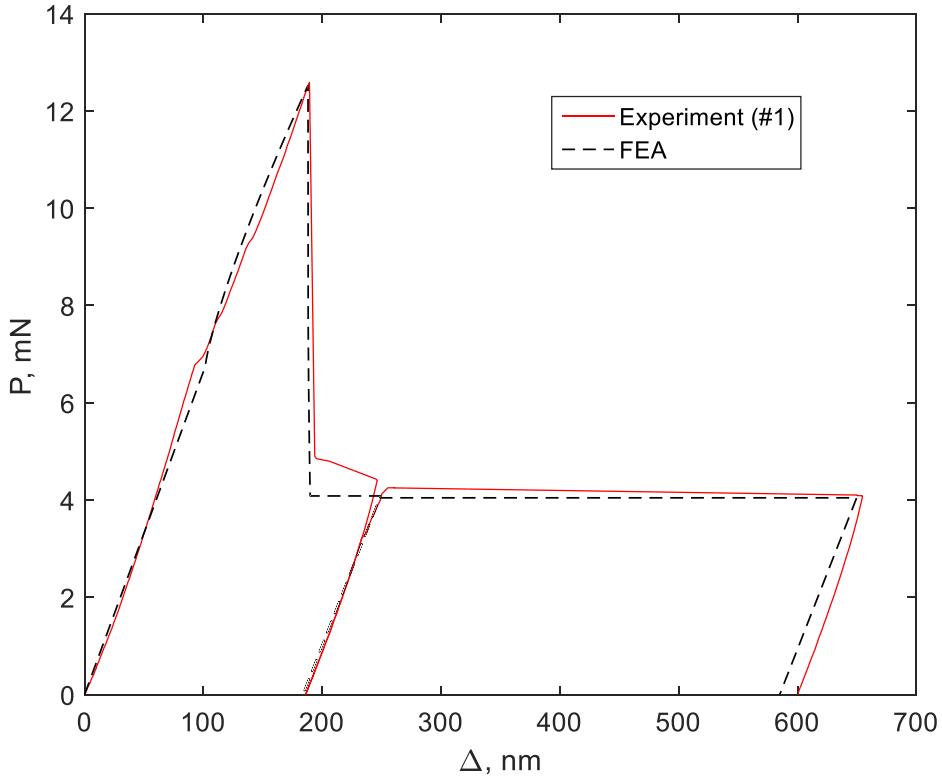

Figure 34: Comparison of force-displacement responses from cohesive zone modeling and experiment.

(a)

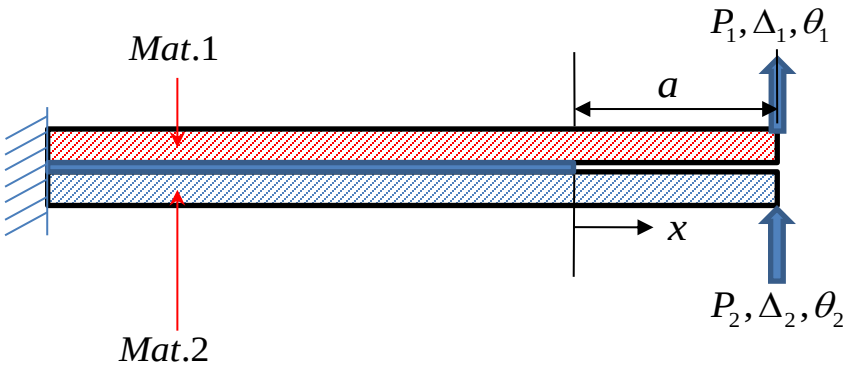

(b)

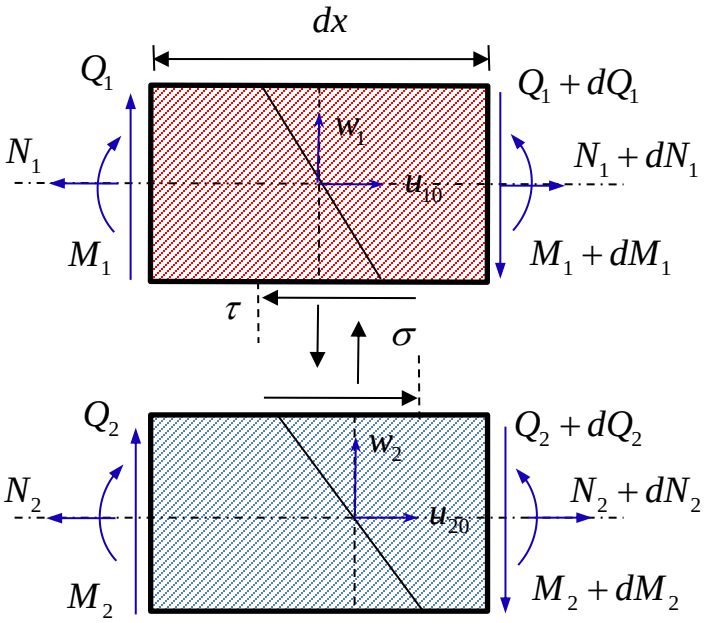

Figure 35: (a) General specimen configuration, (b) free body diagram of interactions between beam elements.

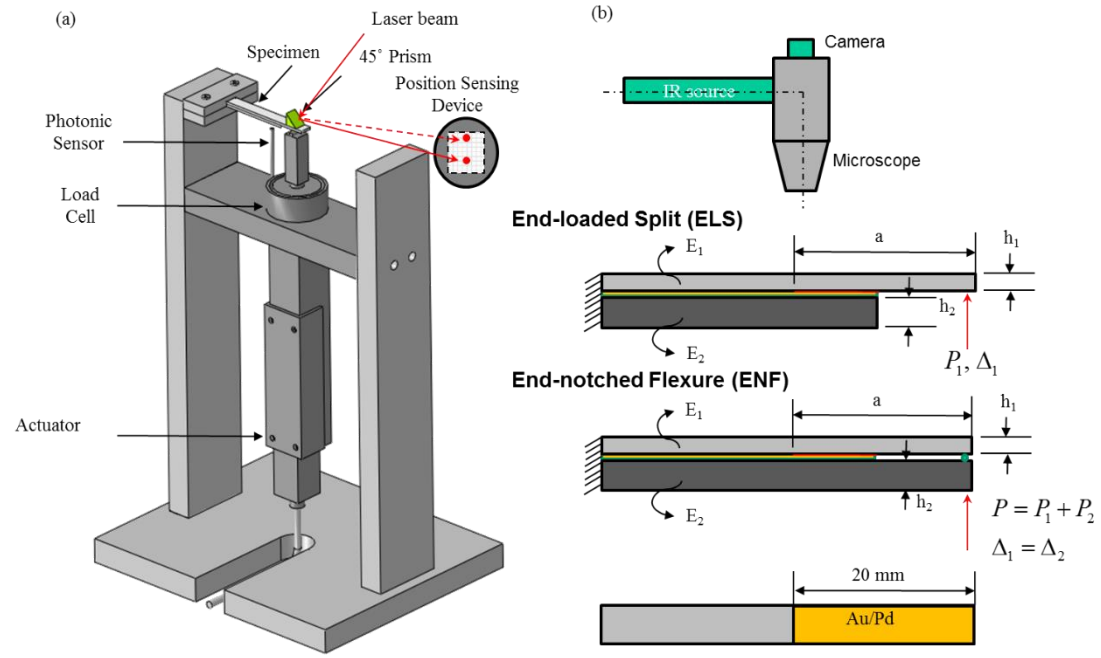

(c)

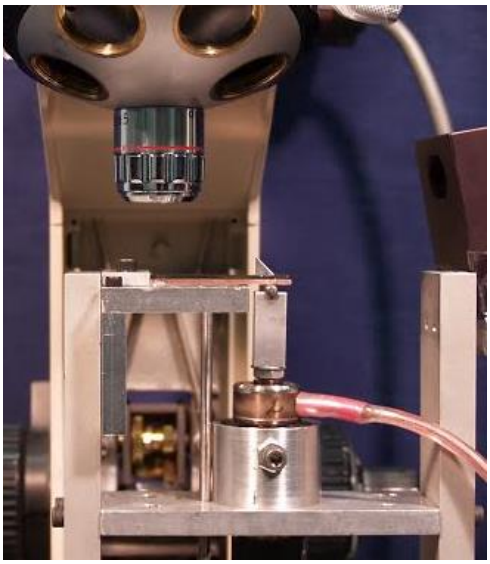

Figure 36: (a) Schematic of loading device, (b) specimen configuration, (c) side view of the apparatus.

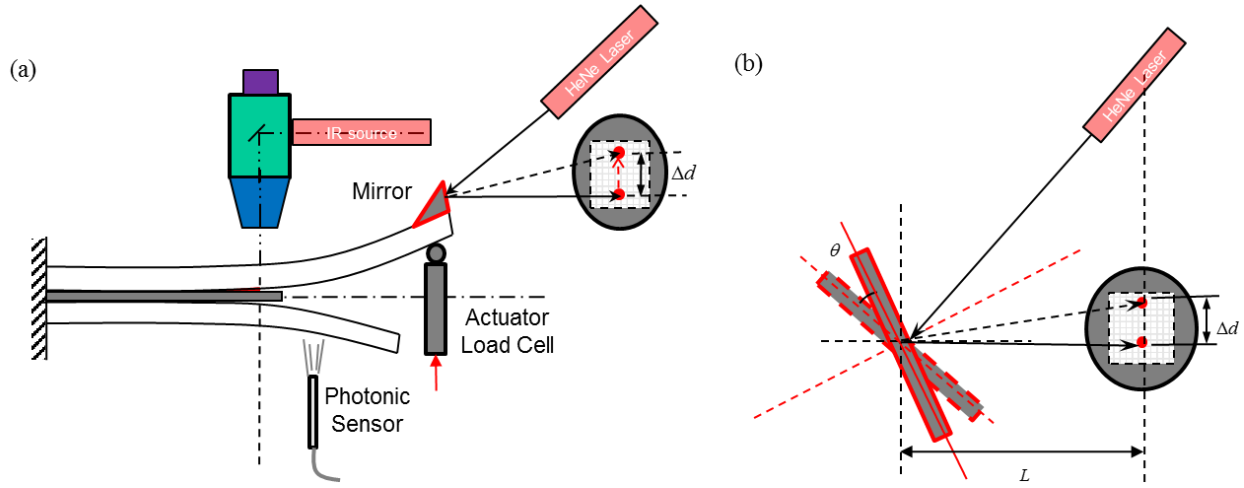

Figure 37: (a) Schematic side view of the experiment, (b) end-rotation measurement using a laser and mirror and position sensing detector.

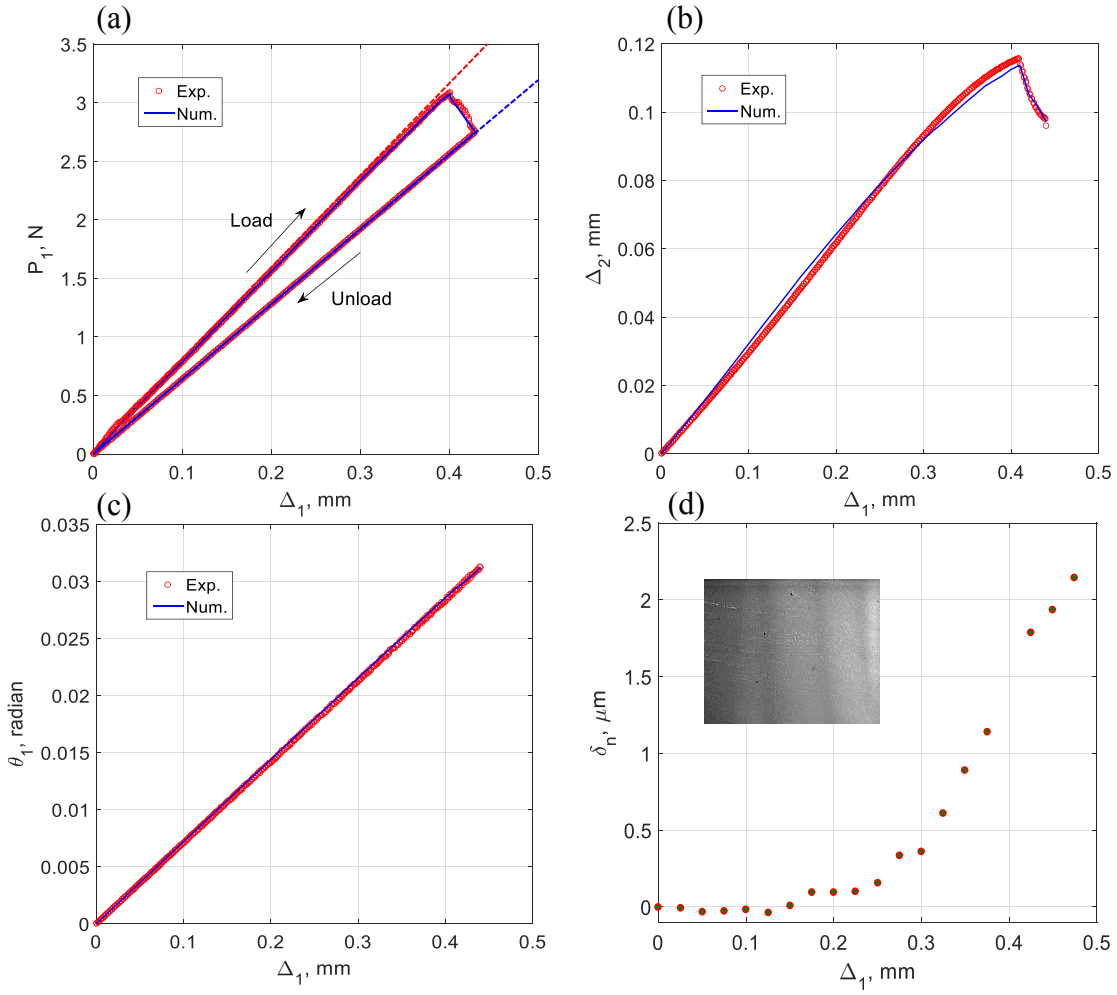

Figure 38: Typical response from an ELS specimen with silicon as the bottom adherend ($\psi = 26.97°$): (a) force displacement response, (b) end-displacement response, (c) end-rotation response, (d) NCOD versus applied displacement response.

(a)

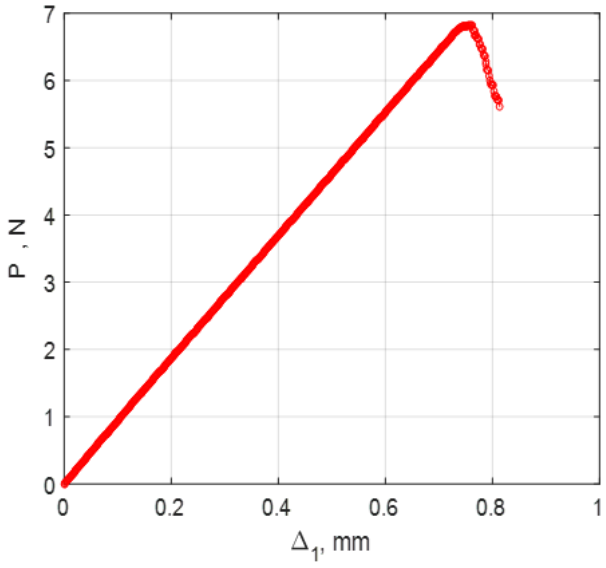

(b)

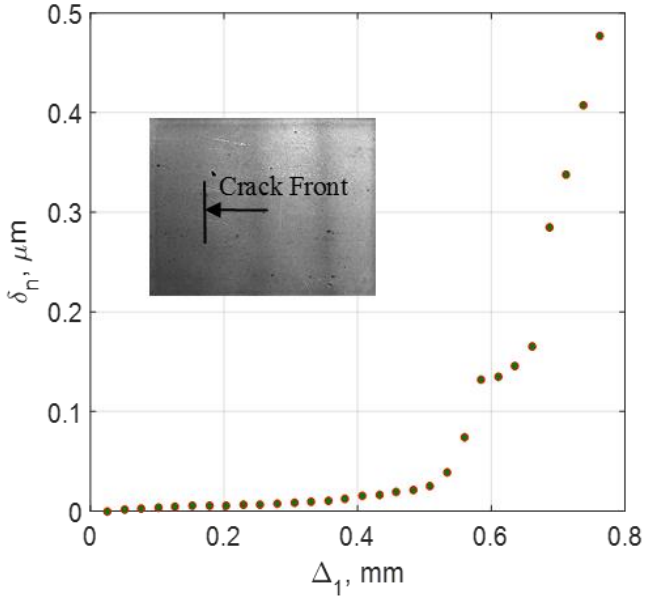

Figure 39: (a) Force and (b) NCOD measurements from an ENF with silicon as bottom adherend ($\psi = 61.07°$).

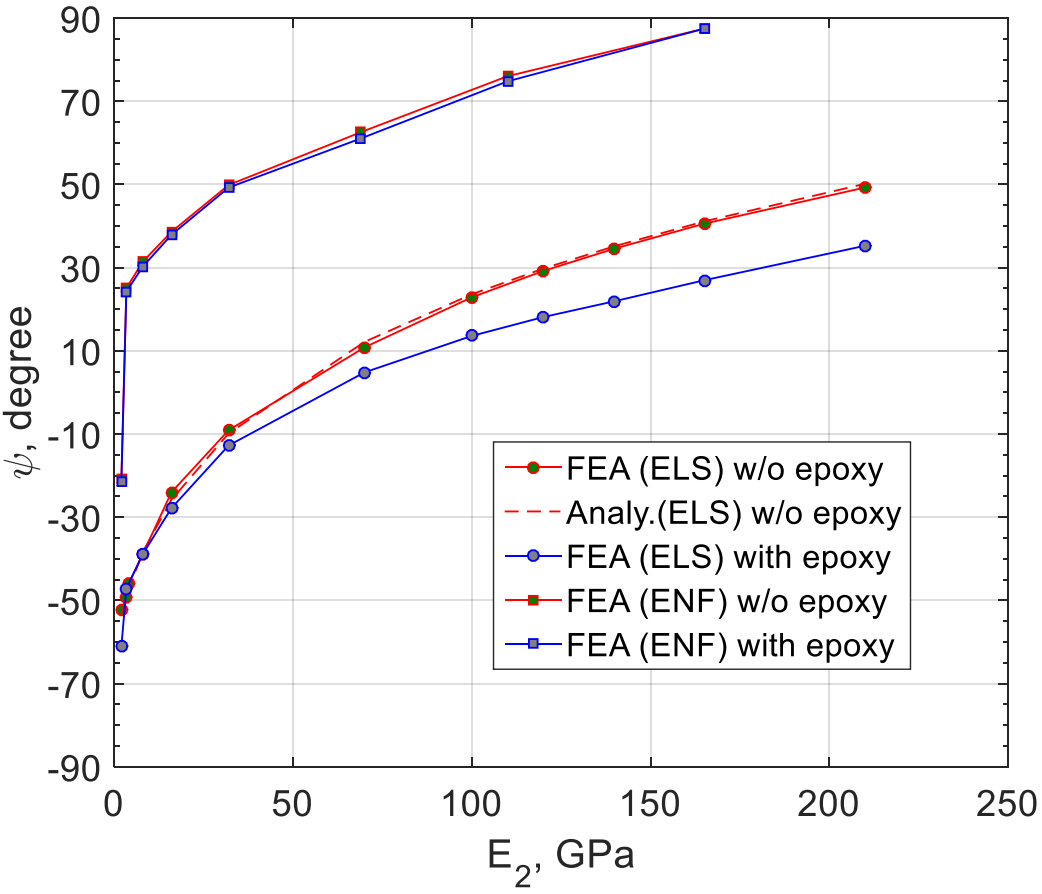

Figure 40: Mode-mix versus Young's modulus of the bottom adherend in a balanced condition.

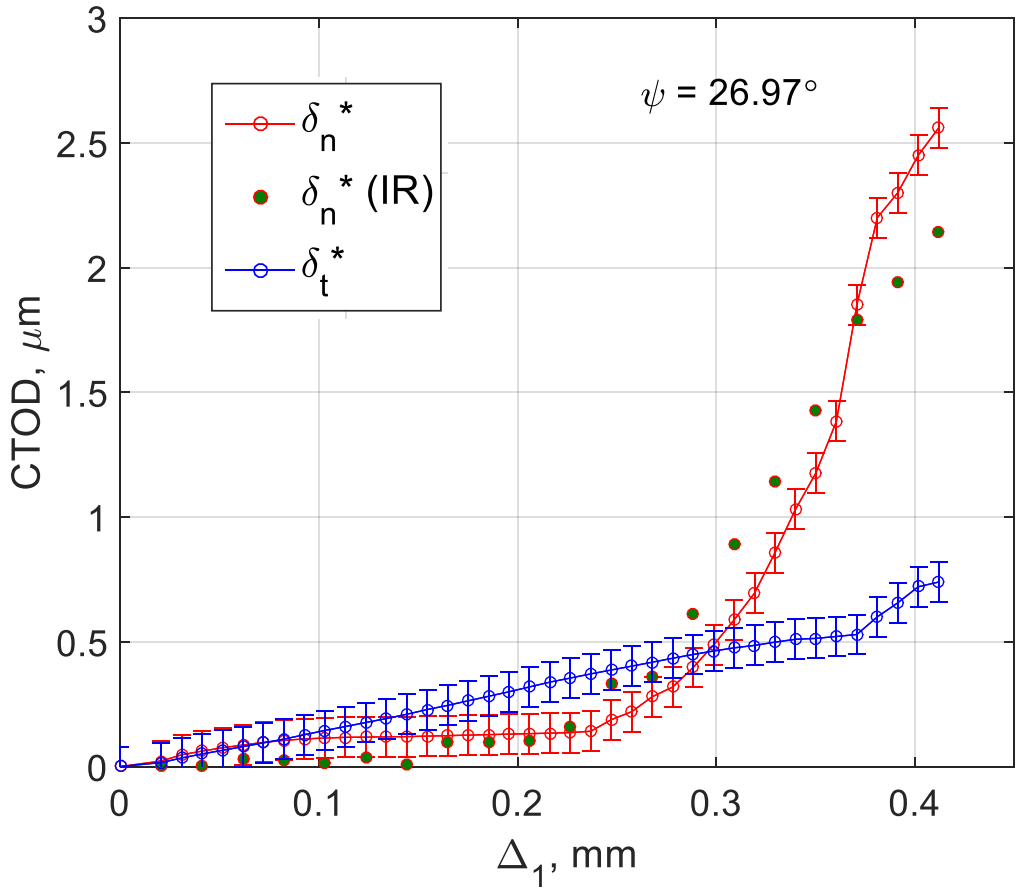

Figure 41: Normal and shear CTOD versus applied end-displacement ($\psi = 26.97°$).

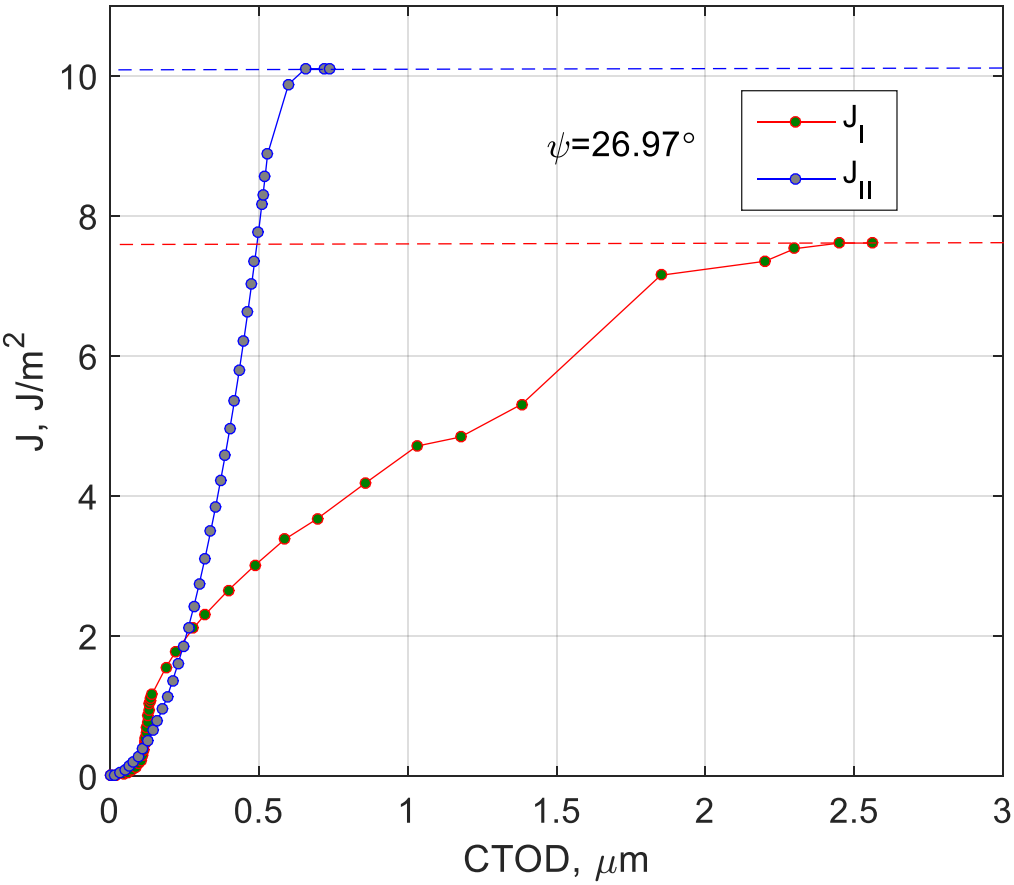

Figure 42: J-integral versus CTOD

(a)

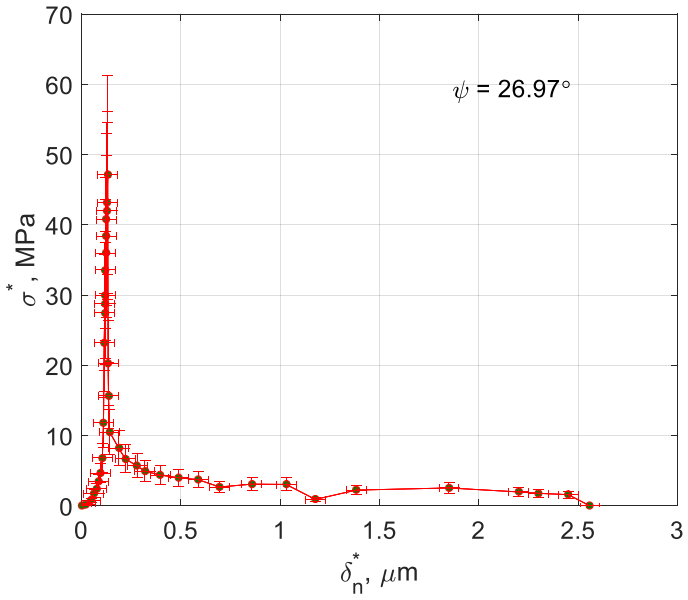

(b)

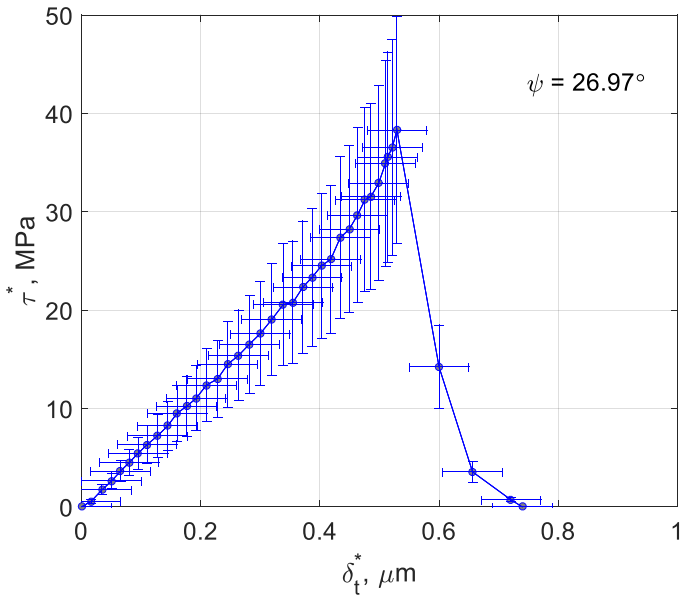

Figure 43: (a) Normal and (b) shear TSR for ELS specimen with silicon as bottom adherend ($\psi = 26.97°$).

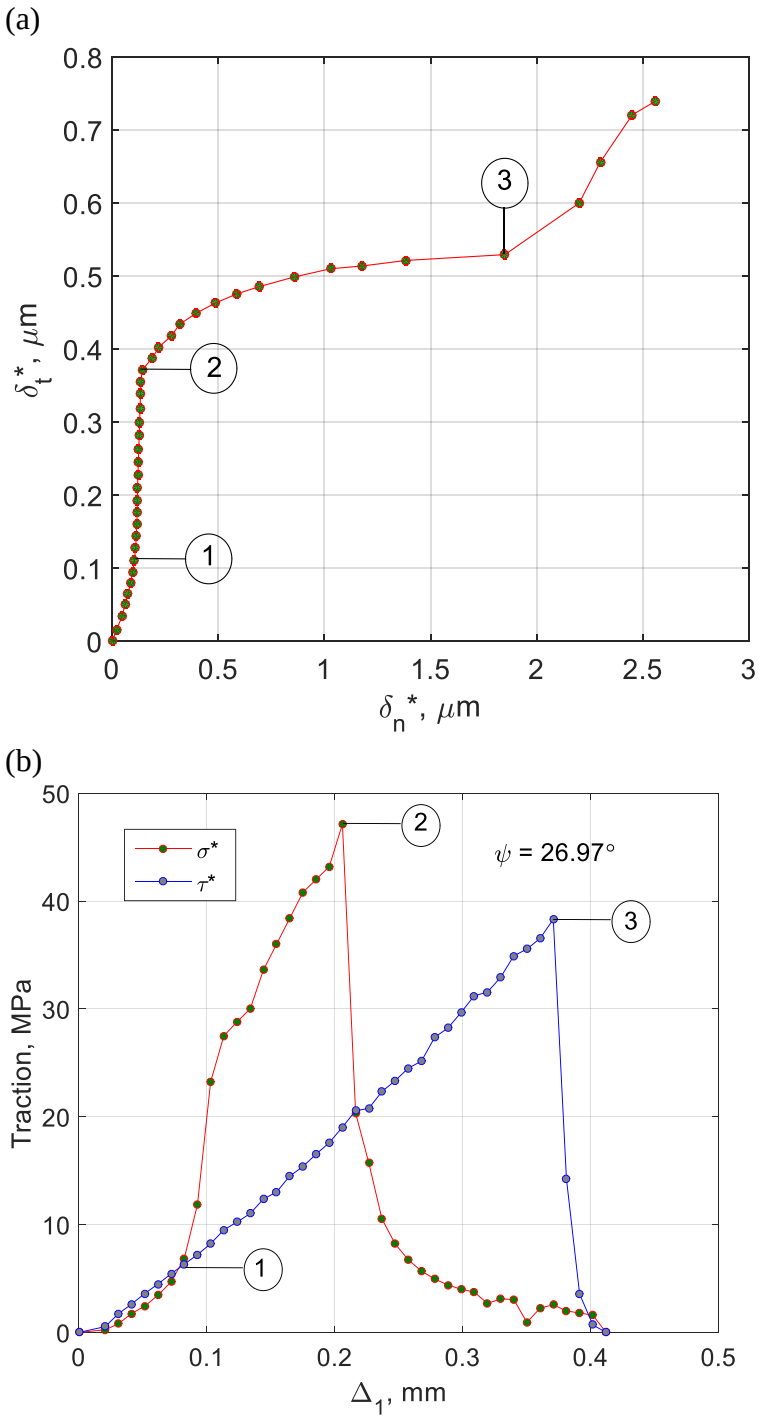

Figure 44: Development of TSRs: (a) separation versus end-displacement, (b) traction versus end-displacement ($\psi = 26.97°$).

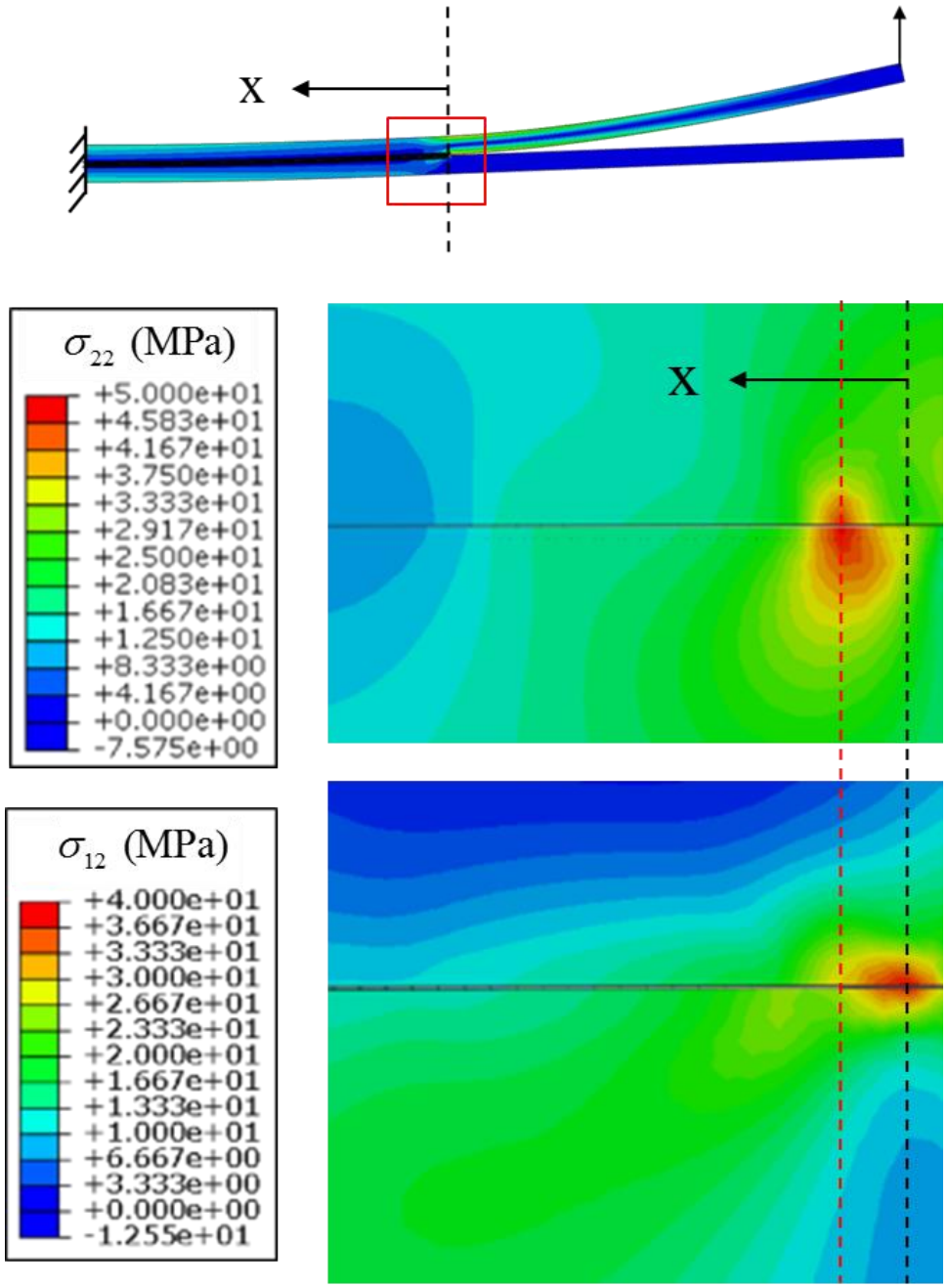

Figure 45: Stress contours near region surrounding crack fronts for normal separation and slip obtained from cohesive zone modeling for an ELS specimen with silicon as the bottom adherend ($\psi = 26.97°$).

(a)

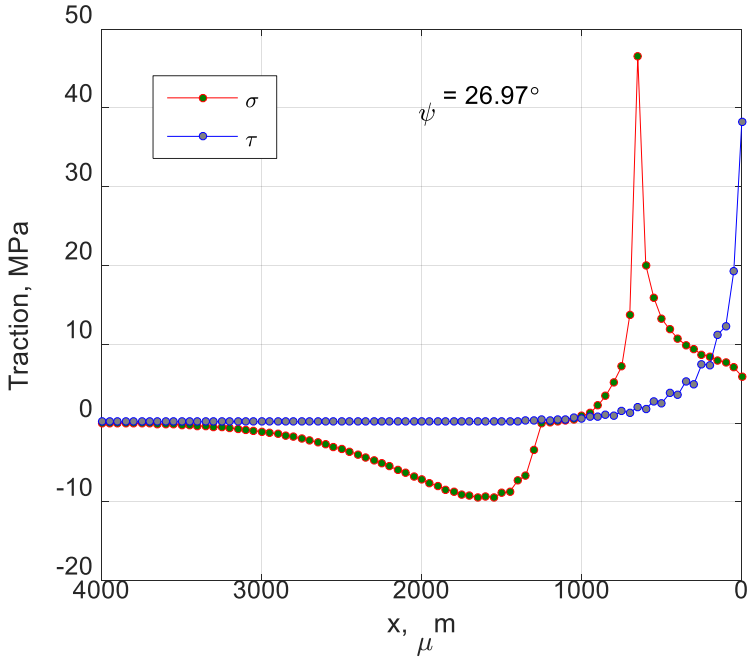

(b)

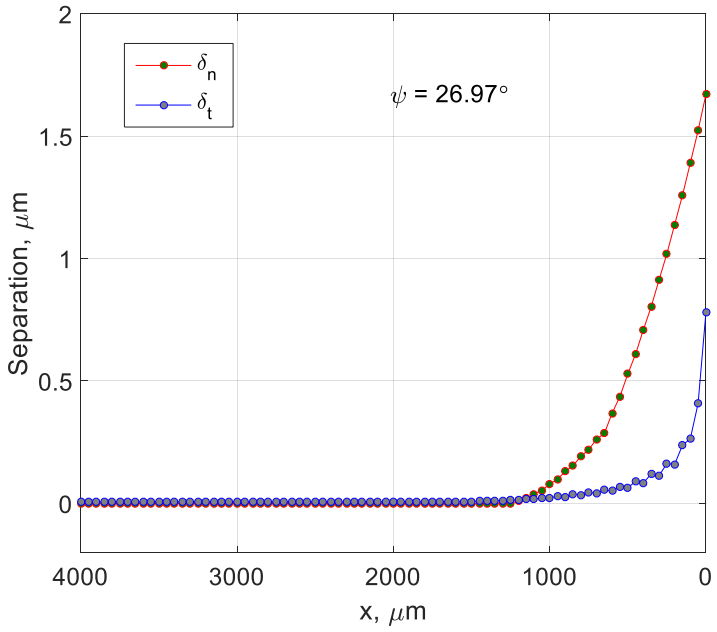

Figure 46: (a) Traction and (b) separation distribution along interface for ELS specimen with silicon as the bottom adherend ($\psi = 26.97°$).

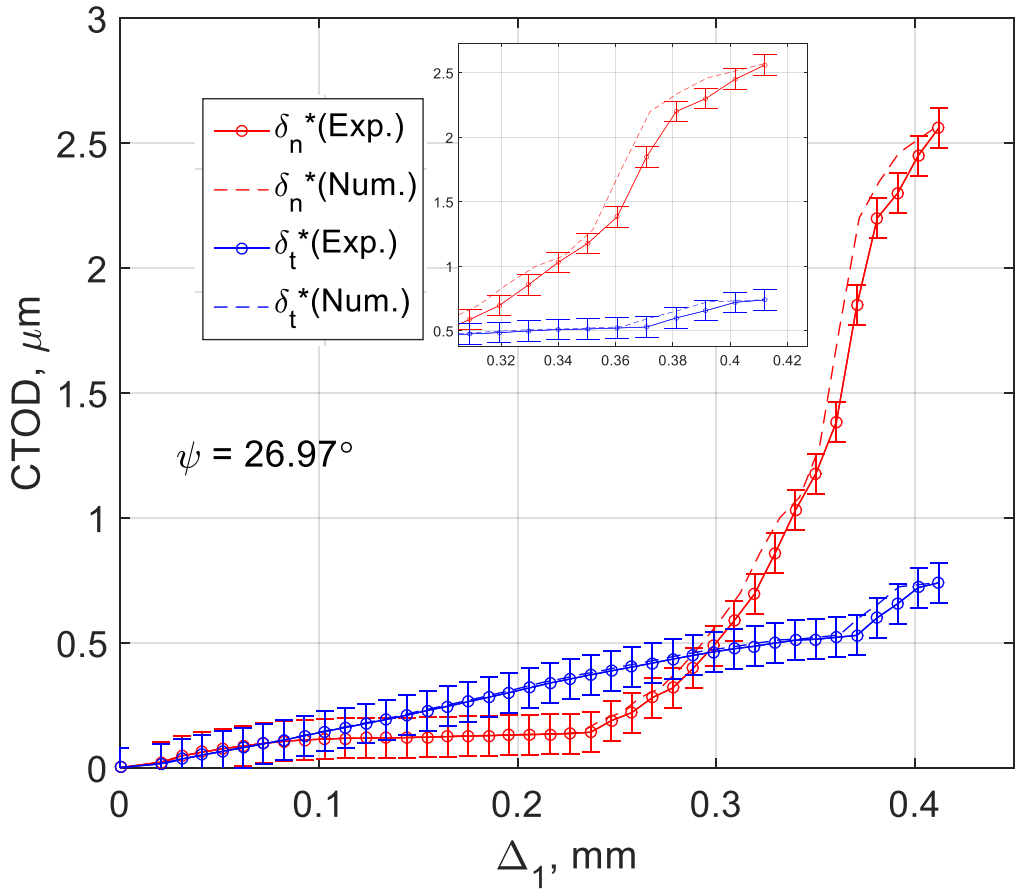

Figure 47: Comparison of CTODs from cohesive zone modeling and deduced values.

(a)

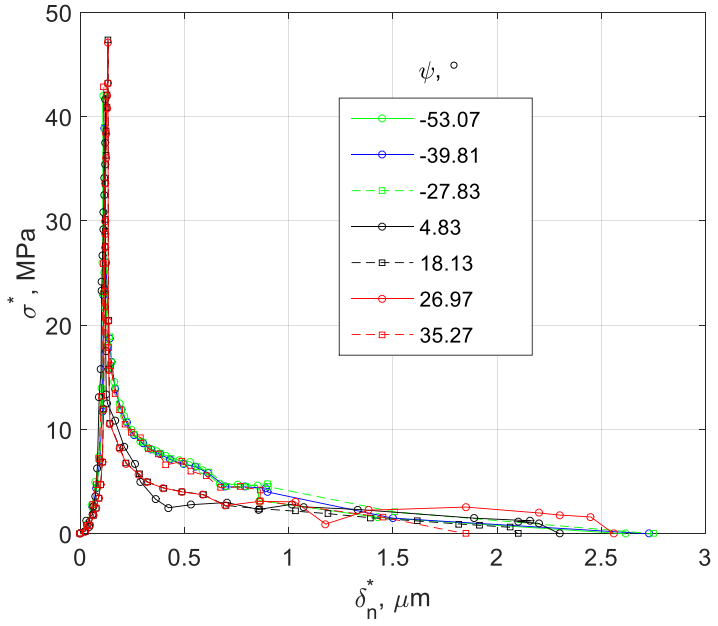

(b)

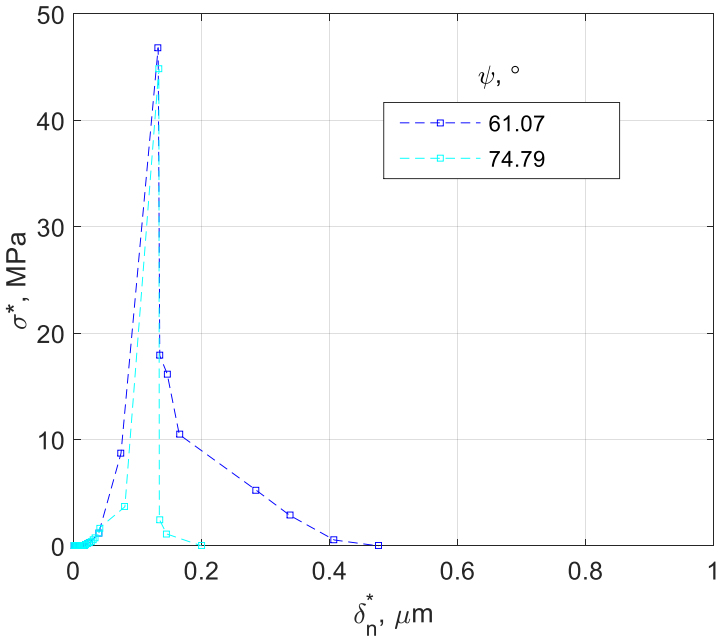

Figure 48: (a) Normal TSRs for low mode-mix, (b) normal TSRs for high mode-mix

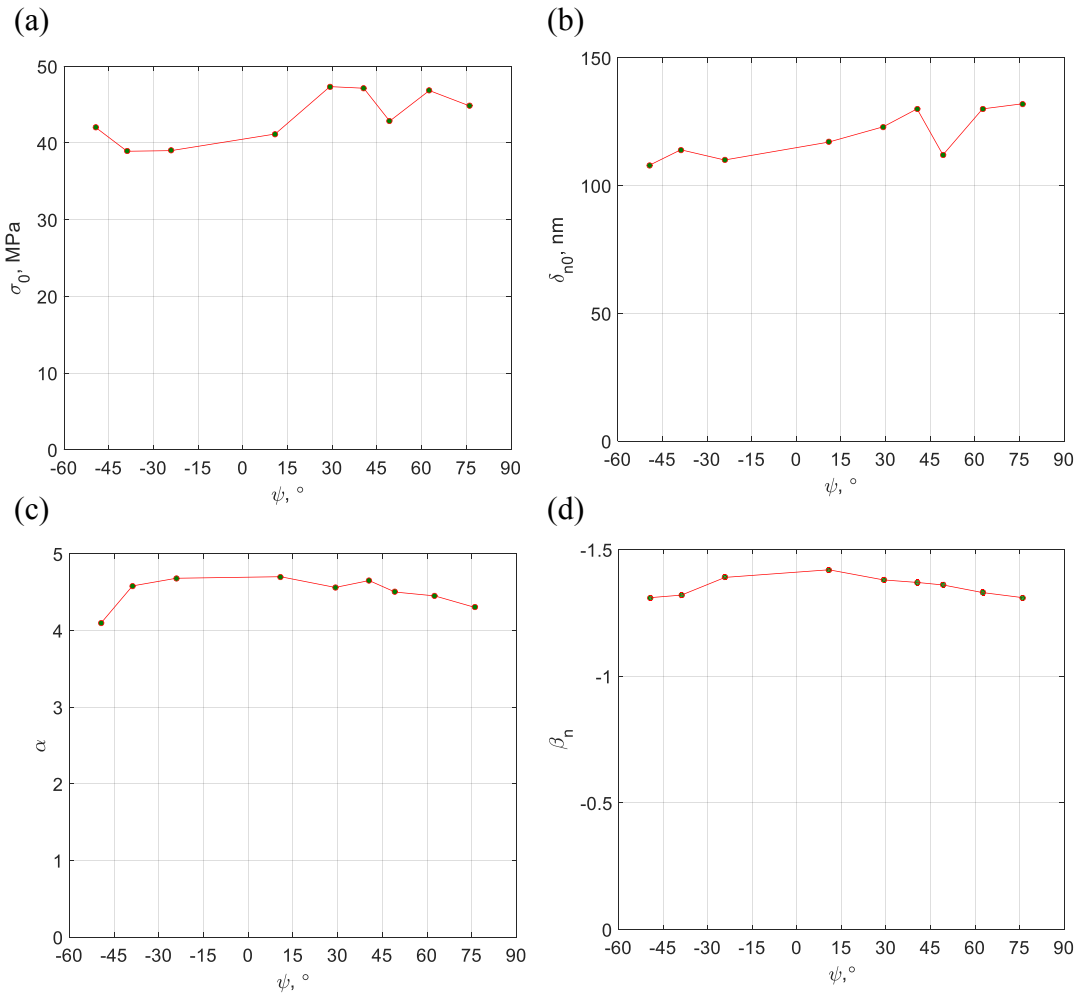

Figure 49: Fitting parameters for the normal TSRs: (a) strength, (b) separation at peak traction, (c) ascending and (d) descending power low exponent.

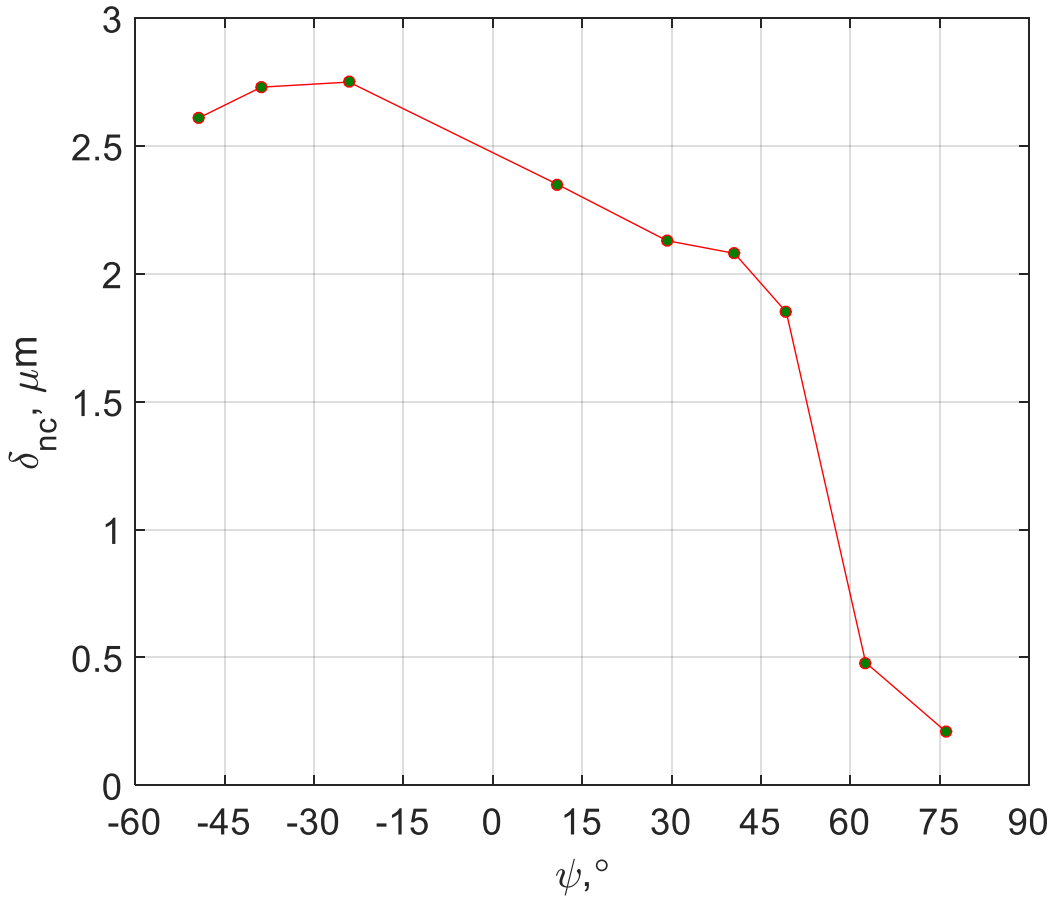

Figure 50: Variation of critical normal separation with mode-mix.

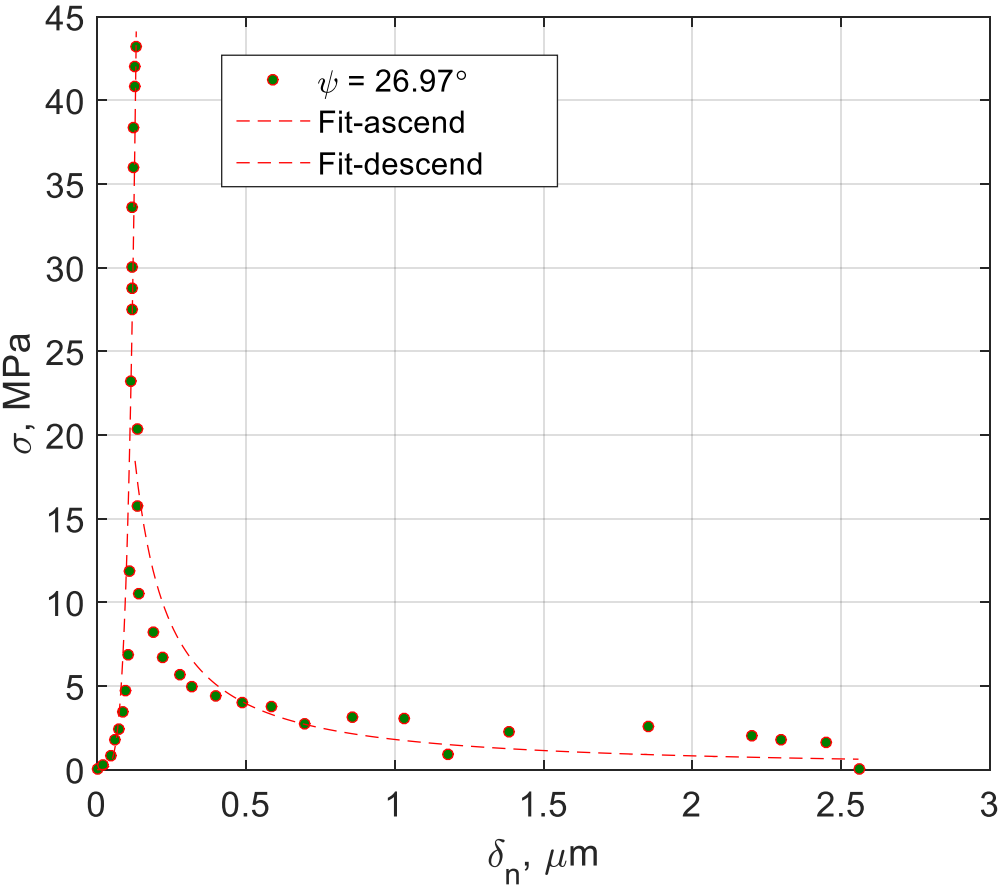

Figure 51a: Illustration of fitting of normal TSR for low mode-mix ($\psi = 26.97°$).

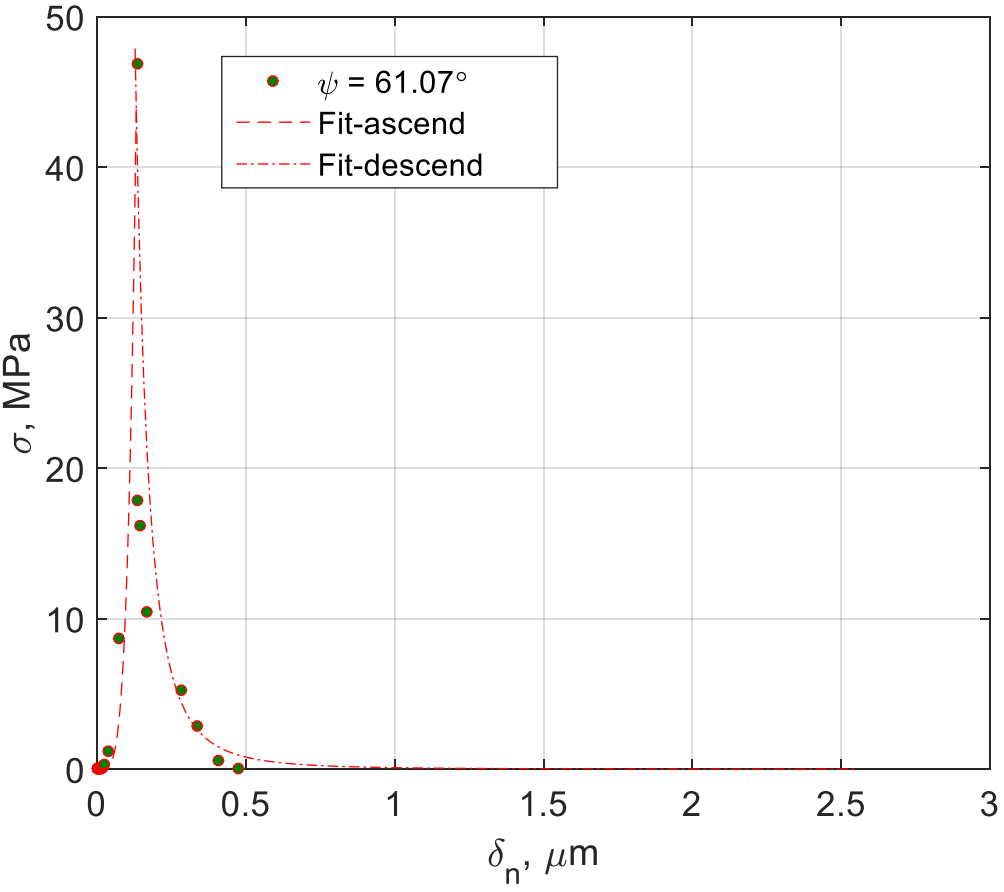

Figure 52b: Illustration of fitting of normal TSR for high mode-mix ($\psi = 61.07°$).

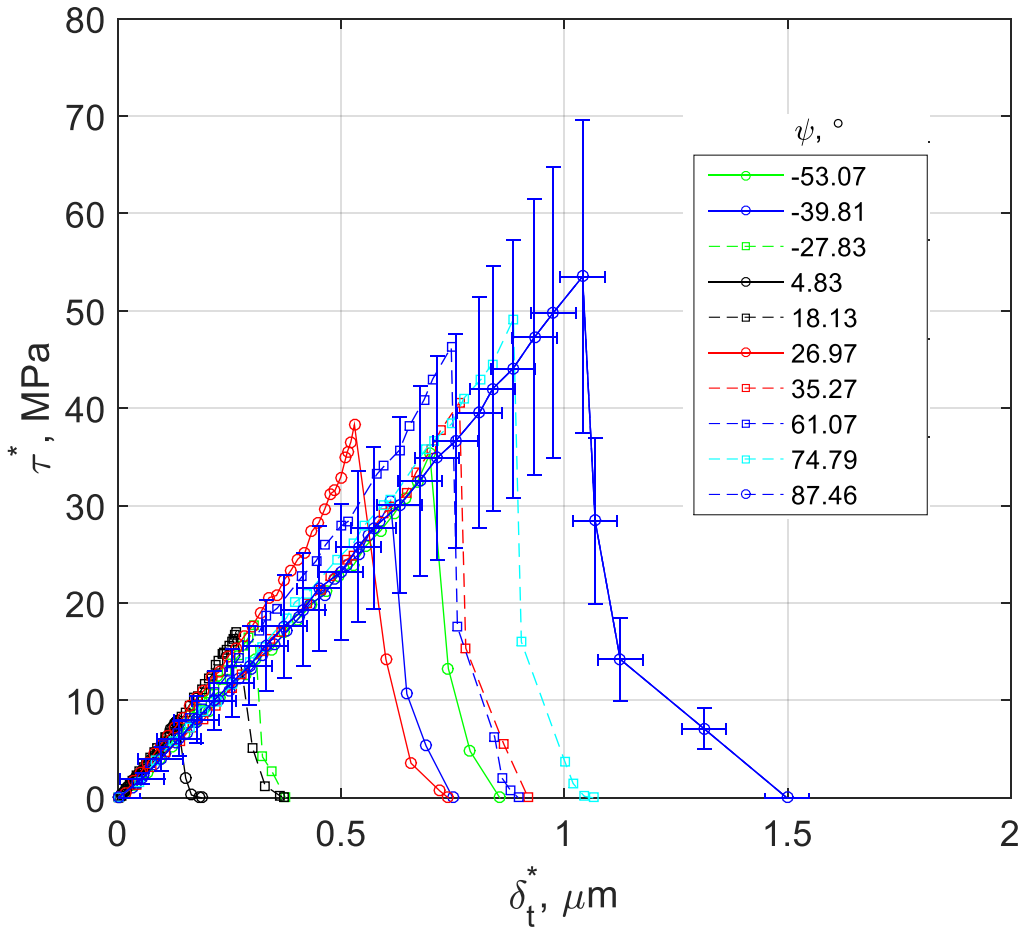

Figure 53: Shear TSRs for all mode-mix angles.

(a)

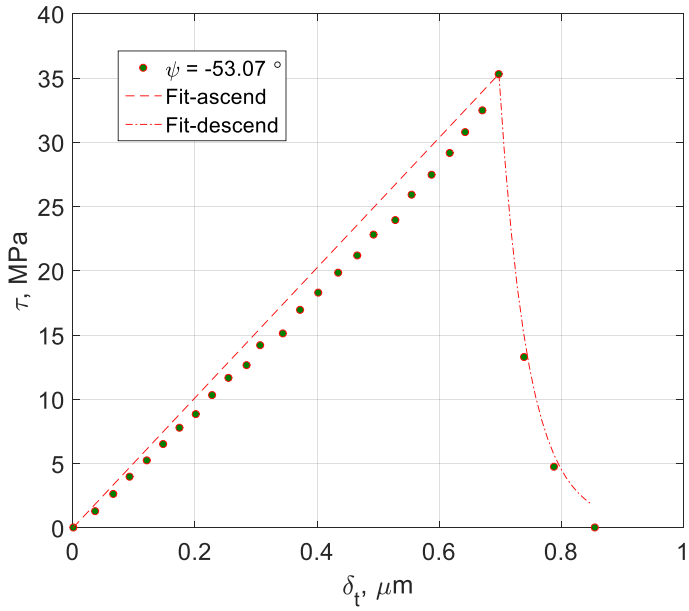

(b)

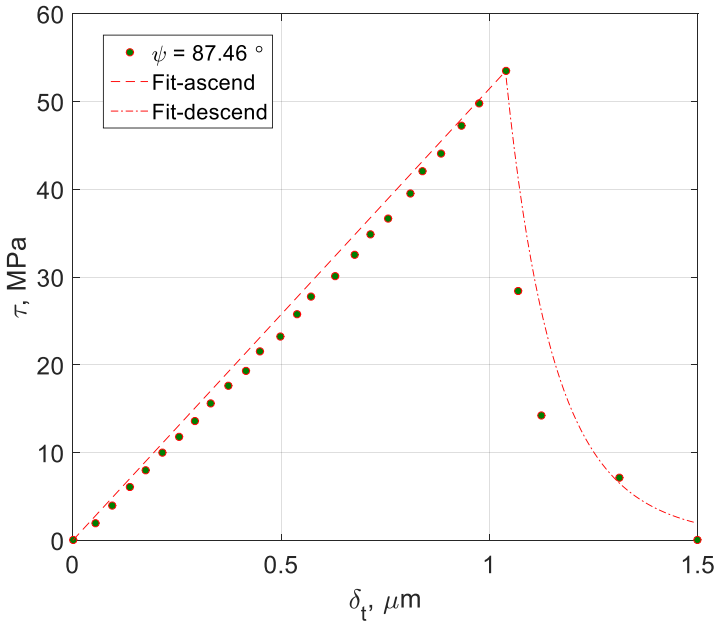

Figure 54: Fitting of shear TSR: (a) aluminum substrate (ENF) ($\psi = -53.07°$), (b) silicon substrate (ENF) ($\psi = 87.46°$).

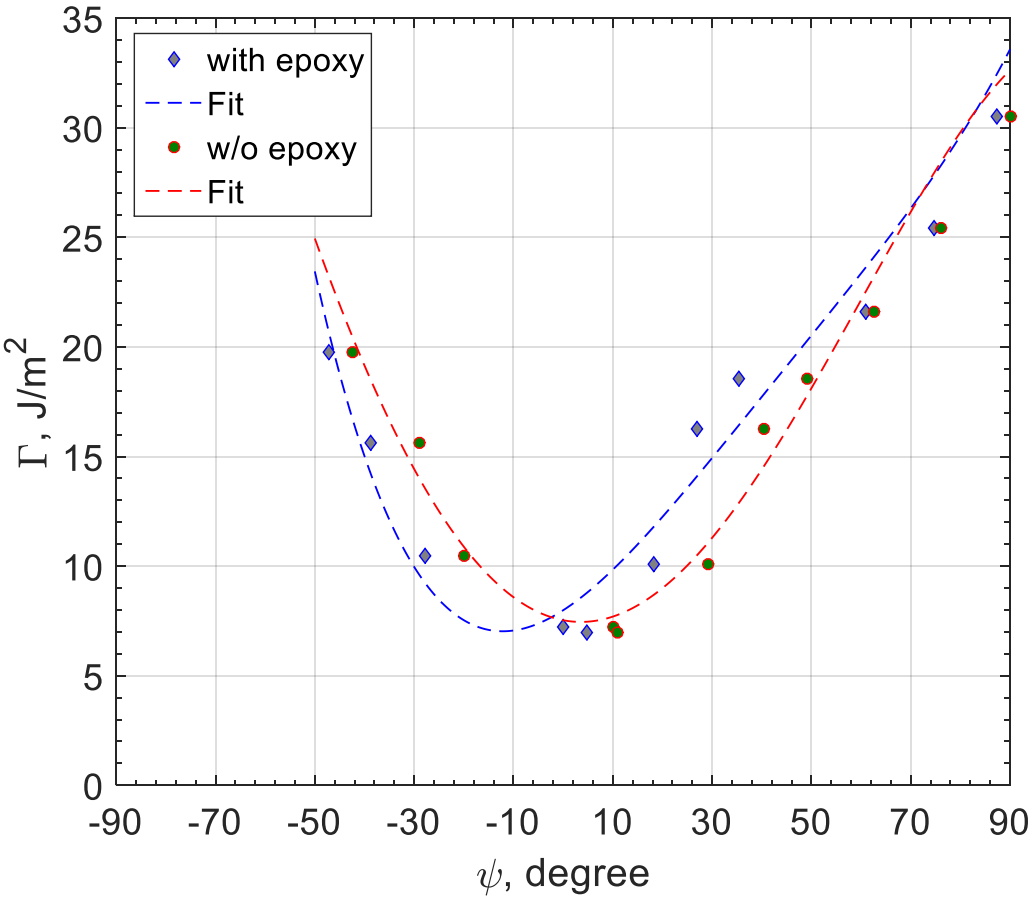

Figure 55: Total toughness (Γ_T) versus phase angle.

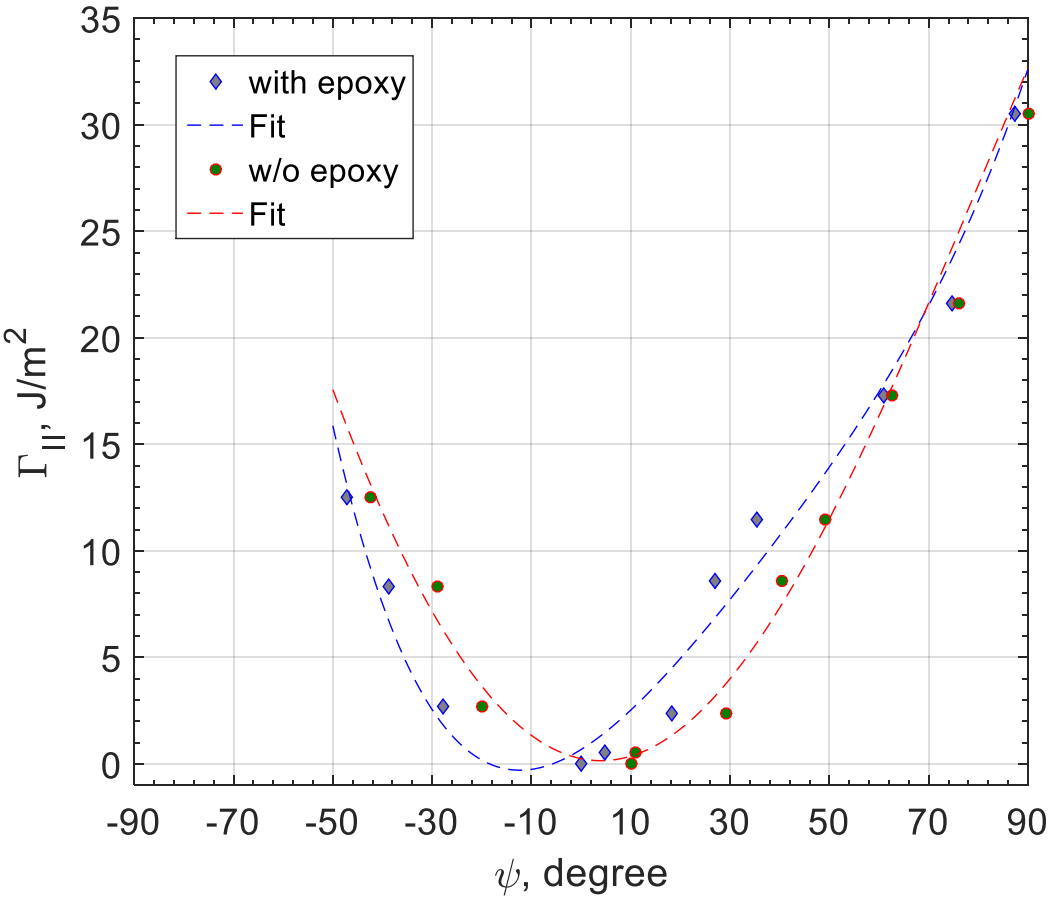

Figure 56: Mode-II toughness (Γ_{II}) versus phase angle.

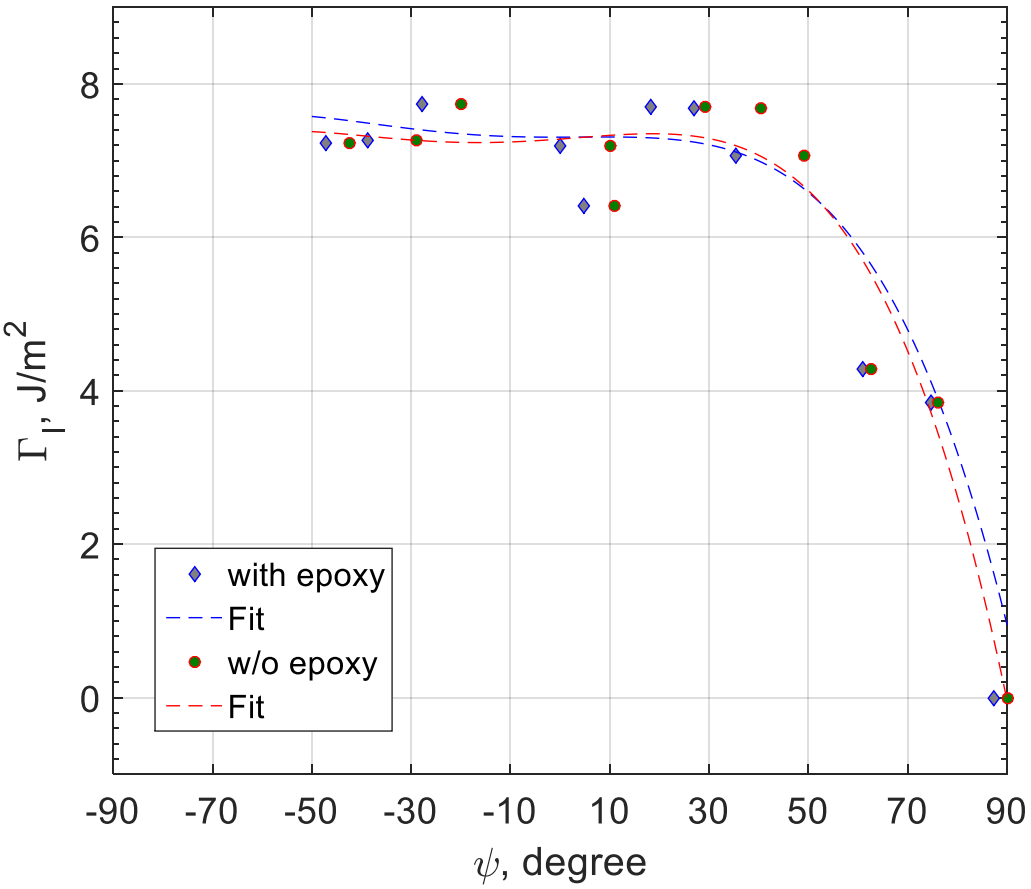

Figure 57: Mode-I toughness (Γ_I) versus phase angle.

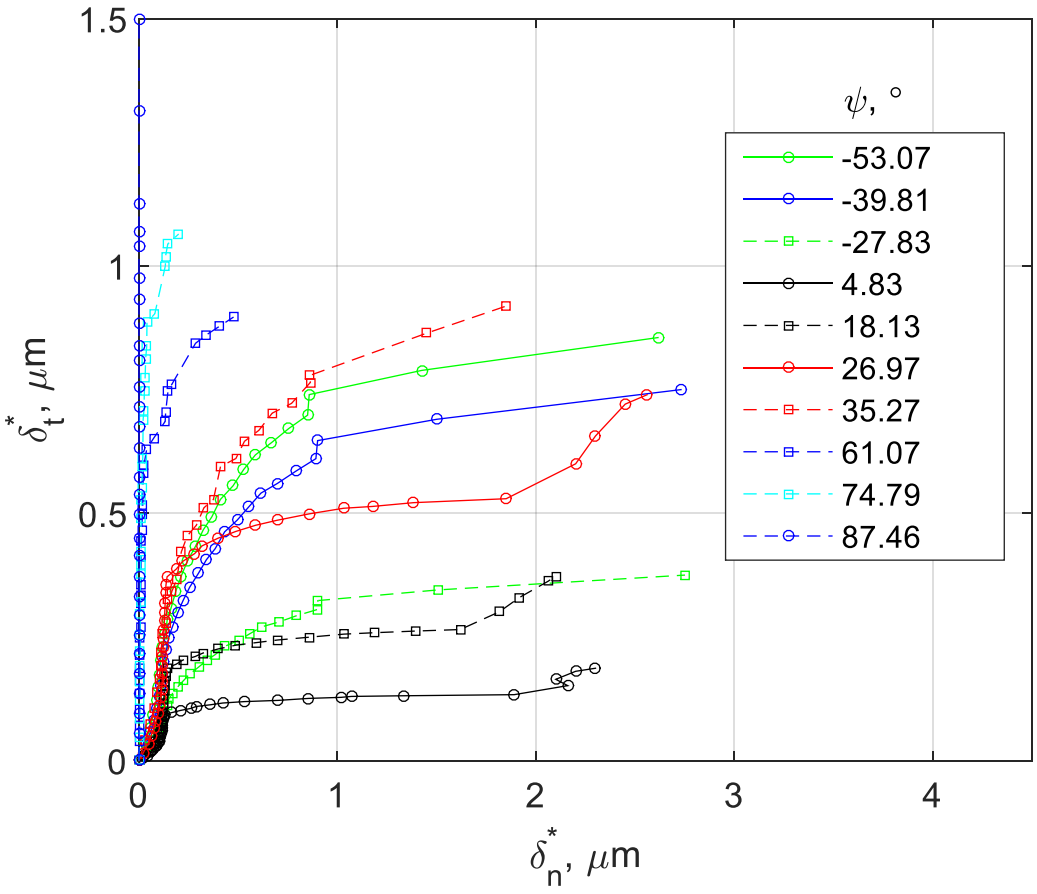

Figure 58: Loading path for different mode-mix angles.

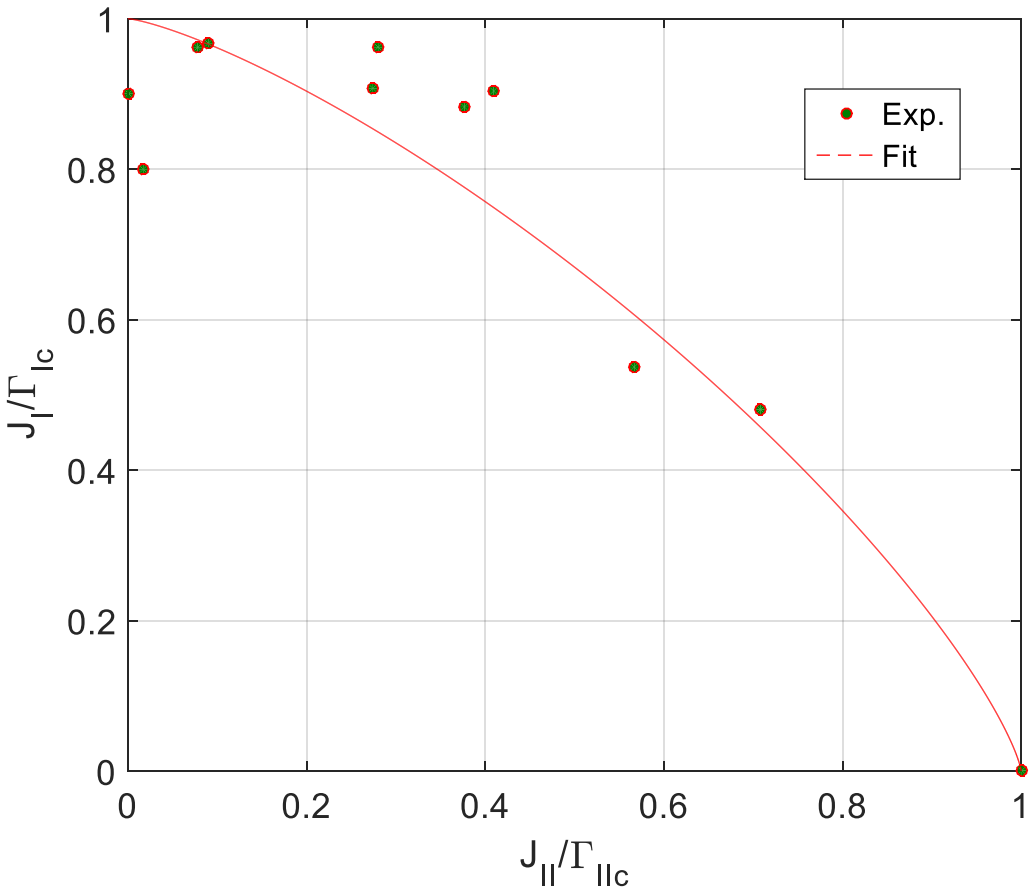

Figure 59: Power-law fracture criterion.

(a)

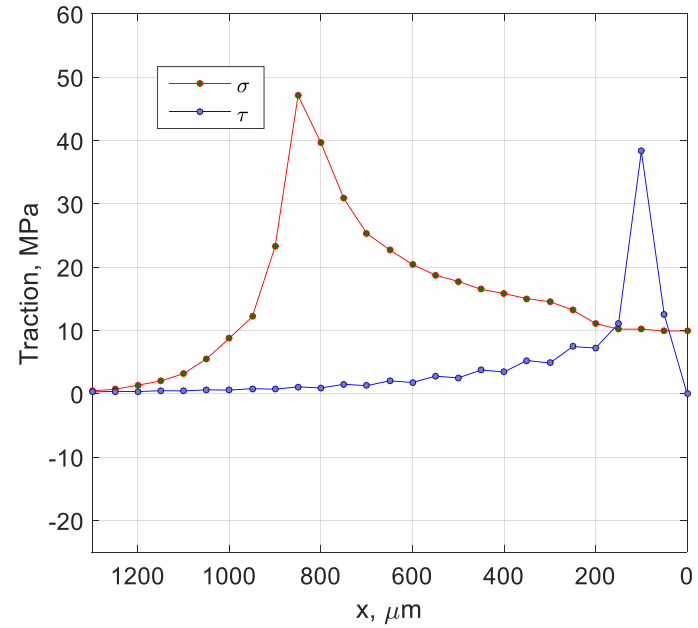

(b)

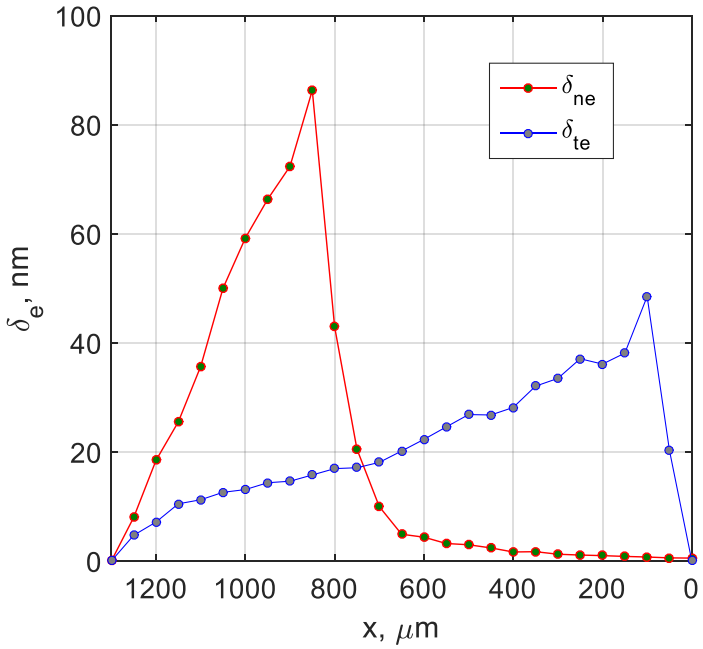

Figure 60: Traction (a) and separation, (b) profiles of the epoxy layer in cohesive zone.

(a)

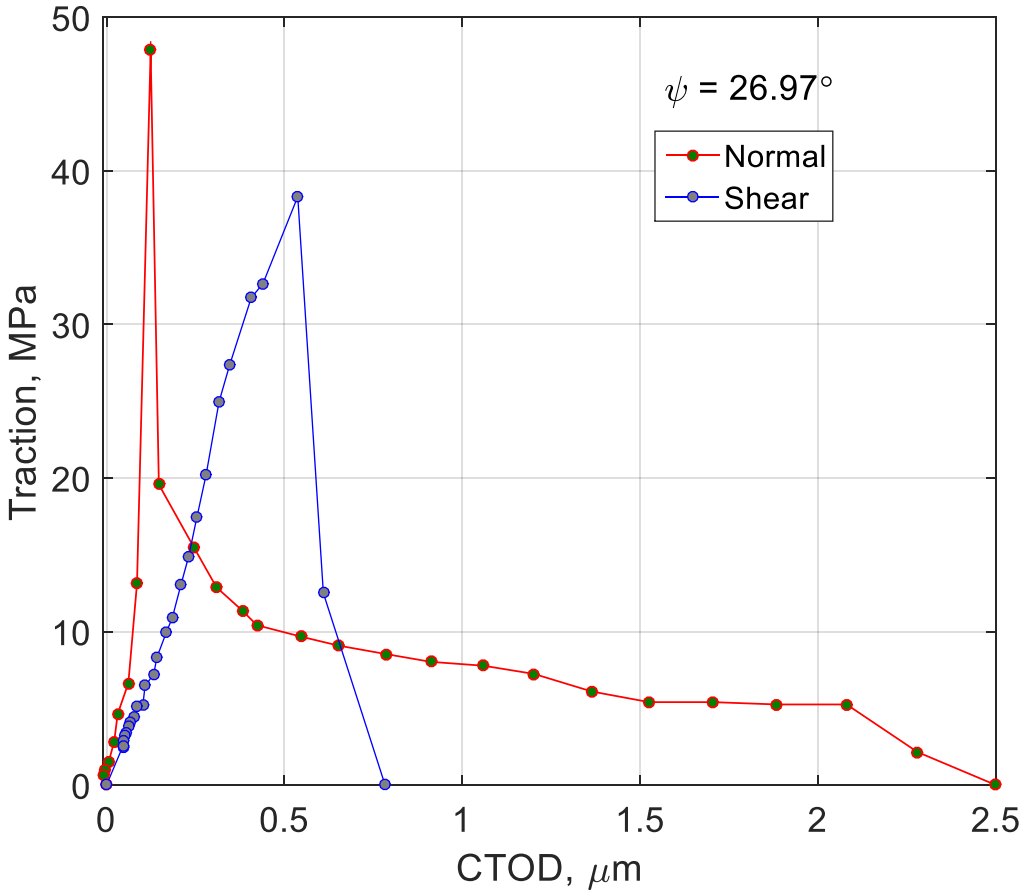

Figure 61: Interfacial TSRs for: (a) $\psi = 26.97°$,

(b)

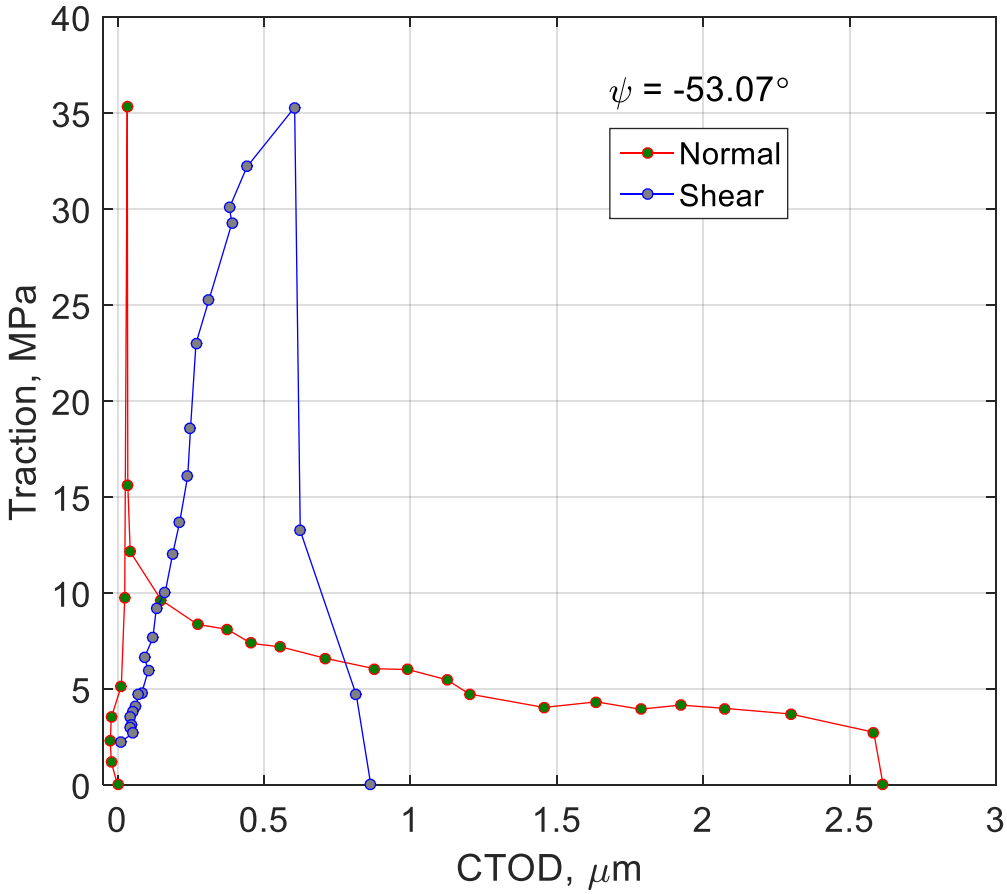

Figure 61: Interfacial TSRs for: (b) $\psi = -53.07°$,

(c)

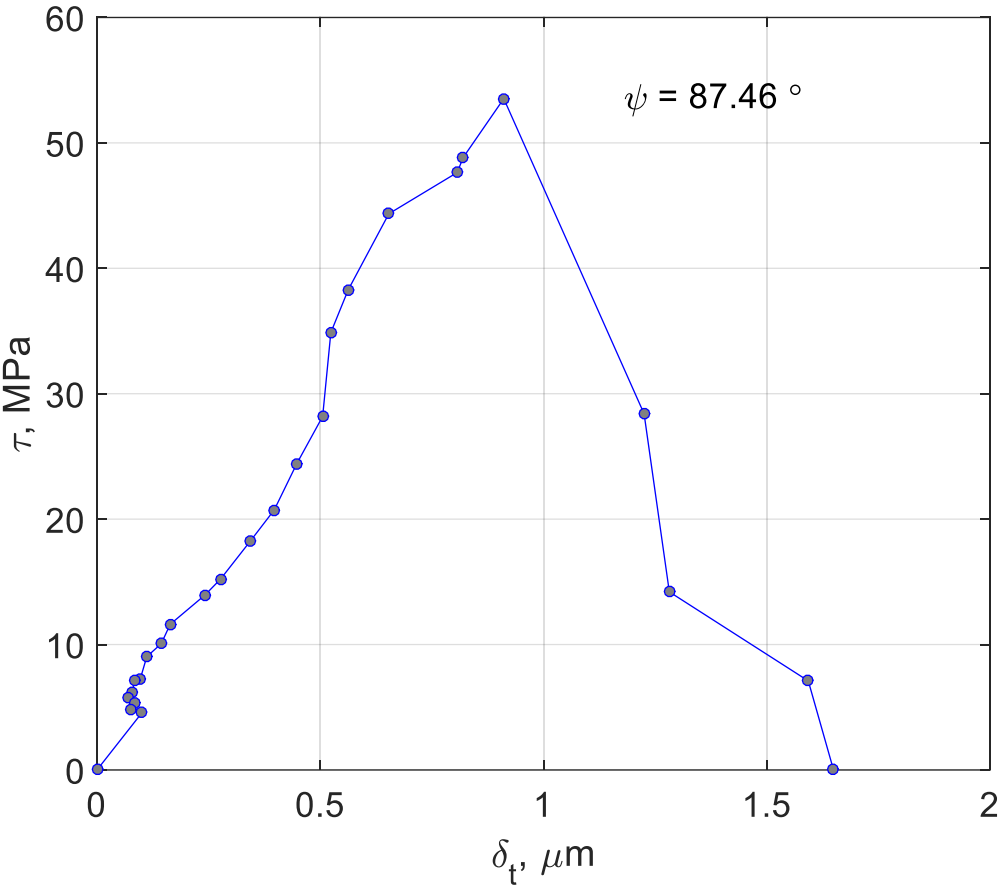

Figure 61: Interfacial TSRs for: (a) $\psi = 26.97°$, (b) $\psi = -53.07°$, (c) $\psi = 87.46°$.

TABLES

Table 1: Extracted parameters for the mixed-mode cohesive zone model.

Epoxy thickness (μm)	**Ψ**	δ_{n0} **(μm)**	δ_0 **(μm)**	Γ_1 **(J/m^2)**	**Γ (J/m^2)**	**K$_0$ (GPa/μm)**	**σ$_{n0}$ (MPa)**	δ_f **(μm)**	α
5	-41°	0.0232	0.0318	0.749	13.10	1.502	36	1.575	6
9.3	-37°	0.0340	0.043	1.120	9.00	1.208	41	0.954	6
50	-26°	0.0234	0.026	0.512	5.00	1.278	35	0.721	6
Average	-	-	-	-	-	1.33	37.3	-	-

Table 2: Tabulated input for the mixed-mode traction-separation relations in ABAQUS.

Energy ratio m$_1$	δ_f **(μm)**	δ_0 **(μm)**	α
0.570	1.537	0.0372	6
0.638	1.101	0.0352	6
0.808	0.669	0.0313	6
1.000	0.236	0.0280	6

Table 3: Element composition from EDS of the interface after pushout.

Element	**Weight (%)**	**Sigma (%)**
Cu	74.34	0.08
Si	10.82	0.03
Ta	1.09	0.08
Fe	0.04	0.01
Os	0.01	0.0018

Table 4: Extracted parameters for the interfacial traction-separation relation.

	Specimen	k **(MPa/nm)**	δ_0 **(nm)**	τ_0 **(MPa)**	τ_c **(MPa)**	J_{II} **(J/m^2)**
Analytical	1	0.418	189.0	79.0	25	7.47
	2	0.392	199.3	78.2	25	7.79
	3	0.402	179.8	72.2	25	6.49
Numerical	1	0.450	179.0	80.5	25	7.20
	2	0.407	193.6	78.8	25	7.63
	3	0.412	175.5	72.4	25	6.35

Table 5: Material properties used in finite element analyses.

	Young's Modulus (GPa)	**Poisson's Ratio**
Cu via	110	0.28
Si	165	0.2
Diamond tip	1220	0.22

Table 6: Specimens details and mode-mix.

Configuration	**Materials for bottom adherend**	**Young's modulus E_2, (GPa)**	**Thickness h_2, (mm)**	**ψ (°) with epoxy**	**ψ (°) w/o epoxy**
ELS	Acylic	3.4	6.97	-53.07	-49.30
ELS	Glassy Polymer	8	4.54	-39.81	-38.85
ELS	Glassfilled Polymer	16	3.21	-27.83	-24.12
ELS	Aluminum	70	1.54	4.83	10.84
ELS	Copper	120	1.17	18.13	29.21
ELS	Silicon	165	1.00	26.97	40.57
ELS	Stainless Steel	210	0.89	35.27	49.27
ENF	Aluminum	69	1.55	61.07	62.58
ENF	Copper	110	1.22	74.79	76.03
ENF	Silicon	165	1.00	87.46	90.00

Table 7: Fitting parameters for normal TSRs.

ψ (°) with epoxy	σ_0 (MPa)	δ_{n0} (nm)	α	β_n	Γ_I (J/m^2)
-53.07	42.00	108	4.10	-1.31	7.23
-39.81	38.92	114	4.58	-1.32	7.26
-27.83	39.00	110	4.68	-1.39	7.74
4.83	41.17	117	4.70	-1.42	6.4
18.13	47.35	123	4.56	-1.38	6.47.7
26.97	47.14	130	4.65	-1.37	7.69
35.27	42.85	112	4.50	-1.36	7.06
61.07	46.84	130	4.45	-1.33	4.29
74.79	44.84	132	4.30	-1.31	3.85
average	42.63	120	4.50	-1.35	N/A

Table 8: Fitting parameters for shear TSRs.

ψ (°) with epoxy	k_t (MPa/μm)	f_t	β_t	Γ_{II} (J/m^2)	δ_{t0} (nm)
-53.07	50.602	0.75	-9.10	12.5	698
-39.81	52.354	0.79	-9.10	8.35	610
-27.83	57.934	0.78	-8.70	2.73	305
4.83	58.000	0.72	-9.50	0.542	133
18.13	62.310	0.70	-9.10	2.4	265
26.97	62.300	0.72	-9.80	8.56	529
35.27	53.059	0.75	-8.50	11.5	746
61.07	58.035	0.80	-9.00	17.3	765
74.79	52.000	0.79	-8.20	21.6	886
87.46	51.462	0.71	-9.00	30.5	1040
average	55.806	0.75	-9.00	N/A	N/A

Table 9: Coefficients in toughness fitting function.

Toughness	a	b	c	d	e
Γ vs ψ, w. ep. (T)	4.00E-07	-7.00E-05	4.60E-03	1.46E-01	7.98E+00
Γ vs ψ, w/o ep. (T)	2.00E-07	-1.00E-05	6.10E-03	-4.33E-02	7.53E+00
Γ_I vs ψ, w. ep. (I)	0.00E+00	0.00E+00	-1.00E-04	0.00E+00	7.30E+00
Γ_I vs ψ, w/o ep. (I)	3.00E-07	-3.00E-06	1.00E-04	4.80E-03	7.28E+00
Γ_{II} vs ψ, w. ep. (II)	4.00E-07	-7.00E-05	4.70E-03	1.46E-01	6.79E-01
Γ_{II} vs ψ, w/o ep. (II)	-1.00E-07	-7.00E-06	6.00E-03	-4.81E-02	2.50E-01

References

ABAQUS Theory manual and Analysis User's Manual (Version 6.14). *Dassault Systèmes Simulia Corp.*, Providence, RI, USA.

Alexandre, I. Rousseau, K. Alfonso, C. Saikaly, W. Fares, L. Grosjean, C. et al. (2008). *"Optimized FIB silicon samples suitable for lattice parameters measurements by convergent beam electron diffraction",* Micron **39**: 294-301.

Alfano, G. (2006). *"On the influence of the shape of the interface law on the application of cohesive-zone models",* Composites Science and Technology **66**(6): 723-730.

Alfano, G. Crisfield, M. A. (2001). *"Finite element interface models for the delamination analysis of laminated composites: mechanical and computational issues",* International Journal for Numerical Methods in Engineering, **50**(7): 1701-1736.

Alfano, M. Furgiuele, F. Leonardi, A. Maletta, C. Paulino, G. H. (2007) *"Cohesive zone modeling of mode-I fracture in adhesive bonded joints",* Key Engineering Materials **348-349**: 13-16.

Andersson, T. and U. Stigh (2004). *"The stress–elongation relation for an adhesive layer loaded in peel using equilibrium of energetic forces",* International Journal of Solids and Structures **41**(2): 413-434.

Bao, G. and Z. Suo (1992). *"Remarks on crack-bridging concepts",* Applied Mechanics Reviews **45**(8): 355-366.

Barenblatt, G. I. (1962). *"The mathematical theory of equilibrium cracks in brittle fracture",* Advances in Applied Mechanics **7**: 55-129.

Barrett, J. D. and R. O. Foschi (1977). *"Mode II stress-intensity factors for cracked wood beams",* Engineering Fracture Mechanics **9**(2): 371-378.

Bay, B. K., et al. (1999). *"Digital volume correlation: Three-dimensional strain mapping using X-ray tomography",* Experimental Mechanics **39**(3): 217-226.

Bechel, V. T. Sottos, N. R. (1998) *"A comparison of calculated and measured debond lengths from fiber push-out tests",* Composites Science and Technology **58**: 1727-1739

Bei, H. Shim, S. George E. P. Miller, M. K. Herbert, E. G. Pharr, G. M. (2007) *"Compressive strengths of molybdenum alloy micro-piallrs prepared using a new technique",* Scripta Materialia 57: 397-400

Bing, P., et al. (2009). *"Measurement of coefficient of thermal expansion of films using digital image correlation method",* Polymer Testing **28**(1): 75-83.

Bing, Q. and B. D. Davidson (2010). *"An improved methodology for measuring the interfacial toughness of sandwich beams"*. Major accomplishments in composite materials and sandwich structures: An anthology of ONR sponsored research. I. M. Daniels , E. E. Gdoutos and Y. D. S. Rajapakse, Springer**:** 365-380.

Birringer, R. P., et al. (2011). *"High yield four-point bend thin film adhesion testing techniques"*, Engineering Fracture Mechanics **78**(12): 2390-2398.

Brantley, W. A. (1973). *"Calculated elastic constants for stress problems associated with semiconductor devices"*, Journal of Applied Physics **44**(1): 534-535.

Cao, H. C., and Evans, A.G. (1989). *"An experimental study of the fracture resistance of bimaterial interfaces"*, Mechanics of Materials **7**: 295-304.

Cao, Z. Wang, P. Gao, W. Tao. L., Suk J.W., Ruoff R.S., Akinwande D., Huang R., Liechti K.M. (2014). *"A blister test for interfacial adhesion of large-scale transferred graphene"*, Carbon **69:** 390-400.

Callister W. D. and Rethwisch, D. G. (2014) *"Materials Science and Engineering: an Introduction":* John Wiley & Sons, Inc.

Carlsson L. A., Gillespie J. W., Pipes R. (1985) *"On the analysis and design of the end notched flexure (ENF) specimen for Mode II testing"*, Journal of Composite Materials, **20**: 594-604

Chai, H. (1992). *"Experimental evaluation of mixed-mode fracture in adhesive bonds"*, Experimental Mechanics(December): 296-303.

Chai, H. and S. Mall (1988). *"Design aspects of the end-notched adhesive joint specimen"*, International Journal of Fracture **8**: 3-8.

Chai, Y. S. and K. M. Liechti (1991). *"Biaxial loading experiments for determining interfacial fracture toughness"*, Journal of Applied Mechanics **58**: 680-687.

Chai, Y. S. and K. M. Liechti (1992). *"Asymmetric shielding in interfacial fracture under in-plane shear"*, Journal of Applied Mechanics **59**(2): 295-304.

Charalambides, P. G., Cao, H.C., Lund, J., Evans, A.G. (1990). *"Development of a test specimen for measuring the mixed mode fracture resistance of bimaterial interfaces"*, Mech. of Materials(8): 269-283.

Charalambides, P. G., Kinloch AJ., Wang Y., William J. G. (1992). *"On the analysis of mixed mode failure"*, Internation Journal of Fracture **54**:269-291

Charalambides, P. G., et al. (1989). *"A test specimen for determining the fracture resistance of bimaterial interfaces"*, Journal of Applied Mechanics **56**: 77-82.

Chasiotis, I. and W. Knauss (2002). *"A new microtensile tester for the study of MEMS materials with the aid of atomic force microscopy"*, Experimental Mechanics **42**(1): 51-57.

Choi, S. H., et al. (2001). *"Fracture of a ductile layer constrained by stiff substrates"*, Fatigue and Fracture of Engineering Materials and Structures **23**: 1-13.

Chow, C. L., et al. (1979). *"On the determination and application of COD to epoxy-bonded aluminum joints"*, Journal of Strain Analysis for Engineering Design **14**(2): 37-42.

Chu, T. C., et al. (1985). *"Applications of digital-image-correlation techniques to experimental mechanics"*, Experimental Mechanics **25**(3): 232-244.

Comer, A. J., et al. (2013). *"Characterising the behaviour of composite single lap bonded joints using digital image correlation"*, International Journal of Adhesion and Adhesives **40**: 215-223.

Comninou, M. (1977). *"The Interface Crack"*, Journal of Applied Mechanics **44**(4): 631-636.

Comninou, M., and Schmueser, D. (1979). *"The interface crack in a combined tension-compression and shear field"*, Journal of Applied Mechanics **46**: 345-348.

Cox, B. N. and D. B. Marshall (1991). *"The determination of crack bridging forces"*, International Journal of Fracture **49**(3): 159-176.

Dauskardt, R. H., et al. (1998). *"Adhesion and debonding of multi-layer thin film structures"*, Engineering Fracture Mechanics **61**(1): 141-162.

Davidson, B. D. and V. Sundararaman (1996). *"A single leg bending test for interfacial fracture toughness determination"*, International Journal of Fracture **78**(2): 193-210.

De Wolf, I. Croes, K. Varela Pedreira, O. Labie, R. Redolfi A. Van De Peer, M. et al. (2011). *"Cu pumping in TSVs: effect of pre-CMP thermal budget"*, Microelectronics Reliability **51**:1856-1859

Dolbow, J. and M. Gosz (1996). *"Effect of out-of-plane properties of a polyimide film on the stress fields in microelectronic structures"*, Mechanics of Materials **23**(4): 311-321.

Dollhofer, J. Beckert, W. Lauke, B. Schneider, K. (2000), *"Fracture mechancial charaterization of mixed-mode toughness of thermoplasti/glass interfaces"*, Computational Material Science, **19**: 223-228.

Dugdale, D. S. (1960). *"Yielding of steel sheets containing slits"*, Journal of the Mechanics and Physics of Solids **8**(2): 100-104.

Dundurs, J. (1969). *"Edge-bonded dissimilar orthogonal elastic wedges"*, Journal of Applied Mechanics: 36, 650-652.

Dundurs, J. (1978). *"The interface crack"*, Journal of Applied Mechanics-Transactions of the Asme **45**(3): 700-700.

Elices, M., et al. (2002). *"The cohesive zone model: advantages, limitations and challenges"*, Engineering Fracture Mechanics **69**(2): 137-163.

Feraren, P. and H. M. Jensen (2004). *"Cohesive zone modeling of interface fracture near flaws in adhesive joints"*, Engineering Fracture Mechanics **71**(15): 2125-2142.

Ferguson, T. and J. Qu (2003). *"Moisture absorption analysis of interfacial fracture test specimens composed of no-flow underfill materials"*, Journal of Electronic Packaging **125**(1): 24-30.

Ferguson, T. P. and J. Qu (2004). *"Moisture and temperature effects on the reliability of interfacial adhesion of a polymer/metal interface"*. Electronic Components and Technology Conference, 2004. Proceedings. 54th.

Fernlund, G., and Spelt, J. K. (1994). *"Mixed-mode fracture characterization of adhesive joints"*. Composites Science and Technology, **50**: 441-449.

Fichter, W. B. (1983). *"The stress intensity factor for the double cantilever beam"*, International Journal of Fracture **22**: 133-143.

Fung, Y. C. (1965)."*Foundations of solid mechanics"*. Englewood Cliffs, New Jersey, Prentice Hall Inc.

Garrou, P. Bower, C. Ramm, P. Handbook of 3D Integration: Volumes 1 and 2 - Technology and Applications of 3D Integrated Circuits: Wiley, 2012.

Gain, A. L., et al. (2011). *"A hybrid experimental/numerical technique to extract cohesive fracture properties for mode-I fracture of quasi-brittle materials"*, International Journal of Fracture **169**(2): 113-131.

Gillis, P. P. and J. J. Gilman (1964). *"Double-cantilever cleavage mode of crack propagation"*, Journal of Applied Physics **35**(3): 647-658.

Gowrishankar, S., et al. (2012). *"A comparison of direct and iterative methods for determining traction-separation relations"*, International Journal of Fracture **177**(2): 109-128.

Guo, Z.K., Kobayashi, A.S., Hay, J.C., White, K.W. (1999). *"Fracture process zone modeling of monolithic Al2O3"*, Engineering Fracture Mechanics **63(2)**: 115–129.

Hall, J. J. (1967). *"Electronic effects in the elastic constants of n-type silicon"*, Physical Review **161**(3): 756-761.

Heryanto, A. Putra, W. N. Trigg, A. Gao, S. Kwon, W. S. Che, F. X. et al. (2012*). "Effect of copper TSV annealing on via protrusion for TSV wafer fabrication"*, Journal of Electornic Materials 41: 2533-2542.

Hong, S. Kim, K.-S. (2003). *"Extraction of cohesive-zone laws from elastic far-fields of a cohesive crack tip: a field projection method"*, Journal of Mechanics and Physics of Solids **51**: 1267-1286

Högberg, J. L., et al. (2007). *"Constitutive behaviour of mixed mode loaded adhesive layer"*, International Journal of Solids and Structures **44**(25-26): 8335-8354.

Hutchinson, J. W. and A. G. Evans (2000). *"Mechanics of materials: Top-down approaches to fracture"*, Acta Materialia **48**(1): 125-135.

Hutchinson, J. W., et al. (1987). *"Crack paralleling an interface between dissimilar elastic materials"*, Journal of Applied Mechanics **54**: 828-832.

Hutchinson, J. W. and Z. Suo (1992). *"Mixed Mode Cracking in Layered Materials"*, Advances in Applied Mechanics **29**: 64-191.

Ji, G. Ouyang, Z. Li, G. (2011). *"On approximately realizing and characterizing pure mode-I interface fracture between bonded dissimilar materials"*, Journal of Applied Mechanics **78**: 11 p.

Jiang, T. Im, J. Huang, R. Ho, P. S. (2015). *"Through-silicon via stress characteristics and reliability impact on 3D integrated circuit",* MRS Bulletin **40**:248-256

Jiang, T. Wu, C. Im, J. Huang, R. Ho, P. S. (2015). *"Impact of Grain Structures and material Properties on Via Extrusion in 3D interconnects",* Journal of Microelectronics and Electronic Packaging **12**:118-122

Jiang, T. Wu, C. Im, J. Huang, R. Ho, P. S. (2013). *"Plasticity mechanism for copper extrusion in through-silicon vias for three-dimensional interconnects",* Applied Physics Letters, **103**: *211906*

Kamer, A., et al. (2011). *"Adhesion and degradation of hard coatings on poly (methyl methacrylate) substrates",* Thin Solid Films **519**(6): 1907-1913.

Kandula, S. S., et al. (2005). *"Cohesive modeling of quasi-static fracture in functionally graded materials",* Journal of Applied Mechanics **73**(5): 783-791.

Kanninen, M. F. (1973). *"An augmented double cantilever beam model for studying crack propagation and arrest",* International Journal of Fracture **9**(1): 83-92.

Kehoe, L., et al. (2006). *"Measurement of deformation and strain in first level C4 interconnect and stacked die using optical digital image correlation"*. Electronic Components and Technology Conference, 2006. Proceedings. 56th.

Kolluri, M., et al. (2009). *"In-situ characterization of interface delamination by a new miniature mixed mode bending setup",* International Journal of Fracture **158**(2): 183-195.

Kysar, J. W. (2001). *"Crack-opening interferometry at interfaces of transparent materials and metals",* Experimental Mechanics **41**(1): 52-57.

Lecompte, D., et al. (2007). *"Study and generation of optimal speckle patterns for DIC"*. SEM Annual Conference & Exposition on Experimental and Applied Mechanics, Springfield, MA.

Li, S., et al. (2005). *"Use of mode-I cohesive-zone models to describe the fracture of an adhesively-bonded polymer-matrix composite",* Composites Science and Technology **65**(2): 281-293.

Li, S., et al. (2006). *"Mixed-mode cohesive-zone models for fracture of an adhesively bonded polymer–matrix composite",* Engineering Fracture Mechanics **73**(1): 64-78.

Li, S., et al. (2004). *"The effects of shear on delamination in layered materials",* Journal of the Mechanics and Physics of Solids **52**(1): 193-214.

Liang, C., Hutchinson, J.W., (1993), "*Mechanics of the fiber pushout test*", Mechanics of Materials, Vol. 14, 207-221.

Liang, Y. M. and K. M. Liechti (1995). *"Toughening mechanisms in mixed-mode interfacial fracture"*, International Journal of Solids and Structures: 32, 957-978.

Liang, Y. M. and K. M. Liechti (1996). *"On the large deformation and localization behavior of an epoxy resin under multiaxial stress states"*, International Journal of Solids and Structures **33**(10): 1479-1500.

Liechti, K. M. (1993). *"On the use of Classical interferometry techniques in Fracture Mechanics"*. Experimental techniques in fracture. J. S. Epstein. New York, VCH Publishers**:** 95-124.

Liechti, K. M. (1993). *"On the use of classical interferometry techniques in fracture mechanics"*. Experimental Techniques in Fracture, III. J. S. Epstein. New York, VCH Publishers**:** 95-124.

Liechti, K. M. and T. Freda (1989). *"On the use of laminated beams for the determination of pure and mixed-mode fracture properties of structural adhesives"*, Journal of Adhesion **28**: 145-169.

Liechti, K. M. and E. C. Hanson (1988)."*An examination of mixed-mode debonding in the blister test"*. Philadelphia, American Society for Testing and Materials

Liechti, K. M. and W. G. Knauss (1982). *"Crack propagation at material interfaces II: experiments on mode interaction"*, Experimental Mechanics(October): 383-391.

Liechti, K. M. and Y. M. Liang (1992). *"The interfacial fracture characteristics of bimaterial and sandwich blister specimens"*, International Journal of Fracture **55**(2): 95-114.

Liechti, K. M. and B. Marton (2002). *"Delamination of a high-temperature sandwich plate"*, Experimental mechanics **42**(2): 206-213.

Luo, P. F., et al. (1993). *"Accurate measurement of three-dimensional deformations in deformable and rigid bodies using computer vision"*, Experimental Mechanics **33**(2): 123-132.

Mangalgiri, P. D., et al. (1986). *"Effect of adherend thickness and mixed-mode loading on debond growth in adhesively bonded composite joints"*, NASA Technical Memorandum 88992: 1-46.

McGarry, J. P. Éamonn, Ó. M. Guillaume, P. Beltz, G. E. *"Potential-based and non-potential-based cohesive zone formuatlinos under mixed-mode separation and over-closure. Part I: Theoretical analysis"*, Journal of the Mechanics and Physics of Solids, **63**: 336-362

Mei, H. (2011)."*Fracture and delamination of elastic thin films on compliant substrates: modeling and simulations"*. Ph.D. Dissertation, The University of Texas at Austin.

Mei, H., et al. (2010). *"Initiation and propagation of interfacial delamination in integrated thin-film structures"*. Thermal and Thermomechanical Phenomena in Electronic Systems-12th IEEE Intersociety conference (ITHERM 2010), IEEE.

Mello, A. W. (2003)."*Mixed-Mode Fracture Experiments on Quartz/Epoxy and Sapphire/Epoxy Interfaces"*.

Mello, A. W. and K. M. Liechti (2004). *"A piezoelectric biaxial loading device for interfacial fracture experiments"*, Experimental Mechanics **44**(5): 495-501.

Mello, A. W. and K. M. Liechti (2006). *"The Effect of Self-Assembled Monolayers on Interfacial Fracture"*, Journal of Applied Mechanics **73**(5): 860-870.

Messemaeker, J. D. Pedreira, O. V. Vandevelde, B. Philipsen, H. De Wolf, I. Beyne, E. et al. (2013), *"Impact of post-plating anneal an through-silicon viadimensions on Cu pumping",* IEEE 63rd Electronic Components and Technology Conference pp. 586-591.

Miller, L. F. (1969). *"Controlled collapse reflow chip joining"*, IBM Journal of Research and Development(May): 239-250.

Mohammed, I. and K. M. Liechti (2000). *"Cohesive zone modeling of crack nucleation at bimaterial corners"*, Journal of the Mechanics and Physics of Solids **48**: 735-764.

Moroni, F. and A. Pirondi (2011). *"Cohesive zone model simulation of fatigue debonding along interfaces"*, Procedia Engineering **10**: 1829-1834.

Na, S. R., et al. (2011). *"Delamination Between Functionalized Silicon Surfaces"*. Experimental and Applied Mechanics, Volume 6. T. Proulx, Springer New York**:** 89-89.

Na, S.R., D.A. Sarceno, and K.M. Liechti (2016). *"Ultra long-range interactions between silicon surfaces"*, International Journal of Solids and Structures, **80**: 168-180.

Needleman, A. (1987). *"A continuum model for void nucleation by inclusion debonding"*, Journal of Applied Mechanics **54**: 525-531.

Needleman, A. (1990). *"An analysis of tensile decohesion along an interface"*, Journal of the Mechanics and Physics of Solids **38**: 289-324.

Nguyen, C. Levy A. J. (2009). "An exact theory of interfacial debonding in layered elastic compsosites", International Journal of Solids and Structures **46**: 2712-2723

Ouyang, Z. Li G. (2009). *"Nonlinear interface shear fracture of end notched flexure specimens",* International Journal of Solids and Structures **46**: 2659-2668.

Pan, B., et al. (2009). *"Two-dimensional digital image correlation for in-plane displacement and strain measurement: a review"*, Measurement Science and Technology **20**(6): 1-17.

Park, K. and G. H. Paulino (2011). *"Cohesive zone models: A critical review of traction-separation relationships across fracture surfaces"*, Applied Mechanics Reviews **64**: 1-20.

Park, K., et al. (2009). *"A unified potential-based cohesive model of mixed-mode fracture"*, Journal of the Mechanics and Physics of Solids **57**(6): 891-908.

Parmigiani, J. P. and M. D. Thouless (2007). *"The effects of cohesive strength and toughness on mixed-mode delamination of beam-like geometries"*, Engineering Fracture Mechanics **74**: 2675-2699.

Planas, J., et al. (2003). *"Generalizations and specializations of cohesive crack models"*, Engineering Fracture Mechanics **70**(14): 1759-1776.

Pronin, A. N. and V. Gupta (1998). *"Measurement of thin film interface toughness by using laser-generated stress pulses"*, Journal of the Mechanics and Physics of Solids **46**(3): 389-410.

Rakestraw, M., M. Taylor, D. Dillard, and T. Chang, (1995) "*Time dependent crack growth and loading rate effects on interfacial and cohesive fracture of adhesive joints."* The Journal of Adhesion, **55**(1-2): 123-149.

Rahulkumar, P., Jagota,A., Bennison,S.J., Saigal,S., (2000). "*Cohesive element modeling of viscoelastic fracture: application to peel testing of polymers"*. International Journal of Solids and Structures. **37**: 1873–1897.

Reeder, J. R. and J. R. Crews Jr. (1990). *"Mixed-mode bending method for delamination testing"*, AIAA Journal **28**(7): 1270-1276.

Rice, J. R. (1968). *"A path independent integral and the approximate analysis of strain concentrations by notches and cracks"*, Journal of Applied Mechanics: 35, 379-386.

Rice, J. R. (1988). *"Elastic fracture mechanics concepts for interfacial cracks"*, Journal of Applied Mechanics: 55, 98-103.

Rice, J. R. and G. C. Shih (1965). *"Plane problems of cracks in dissimilar media"*, Journal of Applied Mechanics **32**: 418-423.

Riney, T. D. (1961). *"Residual Thermoelastic Stresses in Bonded Silicon Wafers"*, Journal of Applied Physics **32**(3): 454-454.

Schapery R. A., Davidson BD., (1990), "Predication of energy release rate for mixed-mode delamination using classical plate theory", Applied Mechanics Review **43**:S281-7.

Scrivens, W. A., et al. (2006). *"Development of Patterns for Digital Image Correlation Measurements at Reduced Length Scales"*, Experimental Mechanics **47**(1): 63-77.

Sharpe, L.H., (1972). "*The interphase in adhesion."* The Journal of Adhesion**, 4(1)**: 51-64.

Shen, B. and G. Paulino (2011). *"Direct Extraction of Cohesive Fracture Properties from Digital Image Correlation: A Hybrid Inverse Technique"*, Experimental Mechanics **51**(2): 143-163.

Shi, X. Q., et al. (2007). *"Determination of fracture toughness of underfill/chip interface with digital image speckle correlation technique"*, IEEE Transactions on Components and Packaging Technologies **30**(1): 101-109.

Shirani, A. and K. M. Liechti (1998). *"A calibrated frature process zone model for thin film blistering"*, International Journal of Fracture **93**: 281-314.

Singh HK, Chakraborty A, Frazier CE, Dillard DA. (2010). "*Mixed mode fracture testing of adhesively bonded wood specimens using a dual actuator load frame*". Holzforschung. **64**(3):353-61.

Smith, T. S., et al. (2002). *"Digital volume correlation including rotational degrees of freedom during minimization"*, Experimental Mechanics **42**(3): 272-278.

Sokolnikoff, I. S. (1946). *"Mathematical Theory of Elasticity"*, McGraw-Hill, New York.

Soles, C. L. and A. F. Yee (2000). *"A discussion of the molecular mechanisms of moisture transport in epoxy resins"*, Journal of Polymer Science Part B: Polymer Physics **38**(5): 792-802.

Song, S. H., et al. (2008). *"Influence of the cohesive zone model shape parameter on asphalt concrete fracture behavior"*. AIP Conference 2008, AIP.

Sørensen, B. F. and T. K. Jacobsen (2003). *"Determination of cohesive laws by the J integral approach"*, Engineering Fracture Mechanics **70**(14): 1841-1858.

Sørensen, B. F. and P. Kirkegaard (2006). *"Determination of mixed mode cohesive laws"*, Engineering Fracture Mechanics **73**(17): 2642-2661.

Sorensen, L., et al. (2008). *"Bridging tractions in mode I delamination: Measurements and simulations"*, Composites Science and Technology **68**(12): 2350-2358.

Stigh, U. and T. Andersson (2000). *"An experimental method to determine the complete stress-elongation relation for a structureal adhesive layer loaded in peel"*, ESIS Publication 27**:** 297-306.

Sun, Y. and J. H. L. Pang (2008). *"Digital image correlation for solder joint fatigue reliability in microelectronics packages"*, Microelectronics Reliability **48**(2): 310-318.

Sun, Z., et al. (1997). *"Measuring microscopic deformations with digital image correlation"*, Optics and Lasers in Engineering **27**: 409-428.

Sundararaman, V. and B. D. Davidson (1997). *"An unsymmetric double cantilever beam test for interfacial fracture toughness determination"*, International Journal of Solids and Structures **34**(7): 799-817.

Suo, Z. and J. W. Hutchinson (1988). *"Sandwich test specimens for measuring interface crack toughness"*. Intefacial phenomena in composites: Processing, characterization and mechanical properties, Newport, R.I., Elsevier Sequoia.

Suryanarayana, D., et al. (1991). *"Enhancement of flip-chip fatigue life by encapsulation"*, IEEE Transactions on Components, Hybrids, and Manufacturing Technology, **14**(1): 218-223.

Swadener, J. G. (1998)."*Primary fracture toughness mechanisms of a glass / epoxy interface"*.

Swadener, J. G. and K. M. Liechti (1998). *"Asymmetric shielding mechanisms in the mixed-mode fracture of a glass/epoxy interface",* Journal of Applied Mechanics **65**(1): 25-29.

Swadener, J. G., et al. (1999). *"The intrinsic toughness and adhesion mechanisms of a glass/epoxy interface",* Journal of the Mechanics and Physics of Solids **47**(2): 223-258.

Thouless, M. D., Evans A. G., Ashby M. F., Hutchinson J. W. (1987). "The edge cracking and spalling of brittle plates", Acta Metallurgica **35**: 1333-1341.

Thouless, M. D. (1990). *"Fracture of a model interface under mixed mode loading"*, Acta Metallurgica **35**:1135-1140.

Thouless, M. D. (1994). *"Fracture mechanics of thin films",* IBM Journal of Research and Development **38**(4): 367-377.

Tvergaard, V. and J. W. Hutchinson (1992). *"The relation between crack growth resistance and fracture process parameters in elastic-plastic solids",* Journal of the Mechanics and Physics of Solids **40**(6): 1377-1397.

Ungsuwarungsru, T. and Knauss, W. G. (1987) *"The role of damage-softened material behavior in the fracture of composites and adhesive",* International Journal of Fracture, **35**: 221-241.

Valoroso, N. and L. Champaney (2006). *"A damage-mechanics-based approach for modelling decohesion in adhesively bonded assemblies",* Engineering Fracture Mechanics **73**(18): 2774-2801.

Vendroux, G. and W. G. Knauss (1998). *"Submicron deformation field measurements: Part 2. Improved digital image correlation ",* Experimental Mechanics **38**(2): 86-92.

Volinsky, A. A., et al. (2002). *"Interfacial toughness measurements for thin films on substrates",* Acta Materialia **50**: 441-466.

Volokh, K. Y. (2004). *"Comparison between cohesive zone models",* Communications in Numerical Methods in Engineering **20**(11): 845-856.

Wang, H. and T. Vukanh (1996). *"Use of end-loaded-split (ELS) test to study stable fracture behavior of composites under mode-II loading",* Composite Structures **36**: 71-79.

Wang, J.-S., and Suo Z. (1990). *"Experimental determination of interfacial toughness curves using Brazil Nut sandwiches",* Acta. Metall. Mater. **38**: 1279-1290.

Wang J., Qiao P. (2004). "Interface crack between two shear deformable elastic layers", Journal of Mechanics and Physics of Solids **52**: 891-905.

Wang, S. Harvey, C. M. Guan, L. (2013). *"Partition of mixed modes in layered isotropic double cantilever beams with non-rigid cohesive interfaces",* Engineering Fracture Mechanics **111**:1-25

Warrior,N.A., Pickett, A.K., Lourenco, N.S.F. (2003). "*Mixed-mode delamination experimental and numerical studies"*, Strain, **39**:153–159.

Wiederhorn, S. M., et al. (1968). *"Critical analysis of the theory of the double cantilever method of measuring fracture-surface energies"*, Journal of Applied Physics **39**(3): 1569-1572.

Williams J. G. (1988), *"On the calculation of energy release rates for cracked laminates"*, International Journal of Fracture Mechanics, **36**:101 – 19.

Williams, J. G. (1989). *"End corrections for orthotropic DCB specimens"*, Composites Science and Technology **35**(4): 367-376.

Williams, J. G. and H. Hadavinia (2002). *"Analytical solutions for cohesive zone models"*, Journal of the Mechanics and Physics of Solids **50**(4): 809-825.

Williams, M. L. (1959). *"The stresses around a fault or crack in dissimilar media"*, Bulletin of the Seismological Society of America **49**(2): 199-204.

Wu, C. L., Gowrishankar S., Huang R., Liechti K. M. (2016), "*On determining mixed-mode traction-separation relations for interfaces*", International Journal of Fracture, **202**: 1-19

Xu, X-P. and Needleman, A. (1993). *"Void nucleation by inclusion debonding in a crystal matrix"*, Modeling and Simulation in Maerials Science and Engineering, **2**: 417-418.

Yang, Q. D. and M. D. Thouless (2001). *"Mixed-mode fracture analyses of plastically-deforming adhesive joints"*, International Journal of Fracture **110**(2): 175-187.

Yin, Z. Wu, C. Chen, G. (2014). *"Concrete crack detection through full-field displacement and curvature measurements by visual mark tracking: A proof-of-concept study"*, Structural Health Monitoring **13**:205-218

Yu, H. H. and J. W. Hutchinson (2002). *"Influence of substrate compliance on buckling delamination of thin films"*, International Journal of Fracture **113**: 39-55.

Yuan,H., Chen,J., (2003). *"Computational analysis of thin coating layer failure using a cohesive model and gradient plasticity"*, Engineering Fracture Mechanics, **70**,1929–1942.

Zavattieri, P.D., HectorJr, L.G., Bower, A.F. (2008). *"Cohesive zone simulations of crack growth along a rough interface between two elastic–plastic solids"*, Engineering Fracture Mechanics, **75**: 4309–4332.

Zhu, Y., et al. (2009). *"Direct extraction of rate-dependent traction–separation laws for polyurea/steel interfaces"*, International Journal of Solids and Structures **46**(1): 31-51.

Vita

Chenglin Wu was born in Luoyang, Henan province, China in 1983. He obtained his bachelor degree in civil engineering from Tongji University, Shanghai, China in 2006. He then obtained his master degree in structural engineering from Lawrence Technological University, Southfield, Michigan, USA in 2009. The same year he entered the Missouri University of Science and Technology, where he obtained his Ph.D. degree in civil engineering in 2014. He started his Ph.D. program in engineering mechanics at the University of Texas at Austin in 2013.

Email Address: chenglinwu@utexas.edu

This dissertation was typed by Chenglin Wu.